Use of Glass Fibre Reinforced Polymer (GFRP) reinforcing bars for concrete bridge decks

A thesis submitted in partial fulfillment of the requirements for the

Degree

of Master of Engineering in Civil Engineering

By

Victoria Jane Worner

_____

Department of Civil and Natural Resources Engineering

University of Canterbury

New Zealand

2015

Abstract

Glass Fibre Reinforced Polymer (GFRP) bars have been developed as an alternative to steel reinforcement for various structural concrete applications. Due to their non-corrossive nature, they are particularly suited for harsh environments where steel reinforcement is prone to corrosion. The purpose of this research is to determine the feasibility of GFRP reinforcing bars as concrete bridge deck reinforcement for locations, such as coastal New Zealand, where the non-corrosive benefits of GFRP may offer an alternative to traditional mild steel reinforcement. GFRP use as structural reinforcement may offer life-cycle cost benefits for certain structures as maintenance to repair corroded reinforcement is not necessary. The use of GFRP reinforcement in a New Zealand design context was investigated to directly compare the structural performance of this alternative reinforcing product. Mateen-bar, manufactured by Pultron Composites Ltd, is the GFRP reinforcing bar used in the experimental tests.

Experimental investigation of tensile properties of GFRP bar samples was carried out to understand the mechanical behaviour of GFRP reinforcement and validate the manufacturer's specifications. This series of tests highlighted the complexities of carrying out tensile testing of FRP products, due to the inability to grip the GFRP directly in a testing machine without crushing the specimen.

Two phases of full-scale tests were carried out to compare the performance of bridge deck slabs reinforced with typical mild steel and GFRP reinforcing bar. This experimental testing was different to most existing research on GFRP reinforced slab performance as it did not compare the performance of a GFRP reinforcing bar area equivalent to steel, but was designed in such a way as to dependably give the same moment capacity of the steel reinforced slab design. This incorporated the recommended limit of 20% of design stress given by the manufacturer which led to an apparent over-reinforced section for the GFRP slab design. The aim of the experiments was to investigate the comparative performance of a typical New Zealand bridge deck design and a GFRP reinforced equivalent designed in such a way as is

currently recommended by the manufacturer. The over-reinforcement lead to differences in conclusions drawn by other authors who have studied GFRP reinforced slab behaviour.

Both flexural and concentrated loading (simulating vehicle loading) tests were carried out on both the steel and GFRP reinforced slab designs. Due to over-reinforcement the GFRP slab was considerably stiffer and stronger than the steel design, indicating that serviceability issues are unlikely to be as much of a design issue as existing literature would suggest. Deflection prediction models generally underestimate the strength of over-reinforced sections. All slabs failed in punching shear under concentrated loads, indicating that punching shear may be a critical failure mechanism for GFRP reinforced slabs

Based on the findings from the extensive experimental phases, a set of design recommendations were made to further improve the potential for GFRP to be used for bridge deck design in a New Zealand context.

Acknowledgements

I would like to thank my principal supervisor Dr Alessandro Palermo for his support during this thesis project and for his belief in my ability. Thank you for your continued encouragement and for giving me plenty of opportunities to build confidence and foster my presentation skills. Thank you for the opportunity to travel, meet world renowned engineers and a lot of Italians!

Thank you to my co-supervisor Dr Allan Scott for being a great sounding board for ideas and for your review of my work. Thank you for always being willing to chat about 'where I was at'.

I would like to acknowledge the support of the academic, technical and administrative staff of the Department of Civil and Natural Resources Engineering at the University of Canterbury. Special thanks must go to technicians John Maley, for his assistance and perseverance in the tensile tests, and Tim Perigo for his dedication to my slab testing experiment.

Amongst my fellow post-graduate students in the Department, thanks must go to Sam White, Mustafa Mashal and Zeinab Chegini for travelling to Ashburton with me to finish tying steel and GFRP rebar when time was tight!

I would like to acknowledge the efforts of Jaewoo Park who, as a summer research student, worked to collate a selection of the resources and reference materials that contributed to this thesis.

Thank you to Pultron Composites Ltd. for giving me the opportunity to undertake this experimental research and for your financial and technical support throughout the project. In particular I would like to thank Japser Holdsworth, Peter Renshaw and Moyeen Sawpan for your continued correspondence of advice and feedback. Thank you to Peter for his support during my recent presentation at the NZCI conference 2014.

I would like to acknowledge the Ministry of Business, Innovation and Employment (MBIE) for funding this research project.

I would like to thank Opus International Consultants in Christchurch, especially Michael Cowan and the Bridges and Civil Structures team, for support of my decision to undertake postgraduate study. Thanks for saving a desk for me while I tried to wrap things up!

I would like to thank my husband Tom for his personal support and for the great amount of patience he has shown over this chapter of our lives together. To my parents and in-laws, thank you for the unconditional love and support always and for understanding when I 'didn't want to talk about it'. Thanks to friends and family for trying to seem interested in concrete and offering support anyway!

Table of Contents

List of Figures

List of Tables

Nomenclature

$Ab = area\ of\ reinforcing\ bar, mm^2$

$Af = total\ area\ of\ GFRP\ reinforcing\ bars, mm^2/m$

$b_0 = critical\ perimeter\ surrounding\ load\ footprint\ for\ punching\ shear\ strength, mm$

$d = effective\ depth\ of\ concrete\ section, mm$

$d_b = bar\ diameter, mm$

$d_c = thickness\ of\ cover\ to\ centre\ of\ first\ layer\ of\ bars, mm$

$E = tensile\ modulus\ of\ elasticity, MPa$

$E_c = modulus\ of\ elasticity\ of\ concrete = 4700\sqrt{f_c'}(MPa)$

$E_f = modulus\ of\ elasticity\ of\ GFRP, MPa$

$E_s = modulus\ of\ elasticity\ of\ steel = 200{,}000\ MPa$

$f_c = compressive\ stress\ in\ concrete, MPa$

$f_c' = cylinder\ concrete\ compressive\ strength, MPa$

$f_{cr} = 0.62\sqrt{f_c'}(MPa)$

$f_f = GFRP\ bar\ stress, MPa$

$f_{fu} = design\ tensile\ strength\ of\ GFRP\ bar, MPa$

$f_y = yield\ strength\ of\ steel, MPa$

$FRP = fibre\ reinforced\ polymer$

$GFRP = glass\ fibre\ reinforced\ polymer$

$GTS = guaranteed\ tensile\ strength, MPa$

$I_{cr} =\ cracked\ moment\ of\ inertia = \frac{bd^3}{12} \cdot k^3 + n_f \cdot A_f \cdot d^2 \cdot (1-k)^2$

$I_e = effective\ moment\ of\ inertia$

$I_g = gross\ moment\ of\ inertia = \frac{bh^3}{12}$

$k = ratio\ of\ neutral\ axis\ depth\ to\ depth\ of\ reinforcement$

$k_b = bond\ coefficient$

$L = span\ length$

$l_{db} = basic\ development\ length$

$M_{cr} = cracking\ moment = \frac{f_{cr} \cdot I_g}{y_t} (kN.m)$

$M_a = service\ moment, kN.m$

$n_f = modular\ ratio\ of\ FRP\ and\ concrete = \frac{E_f}{E_c}$

$P = applied\ load$

$P_{SLS} = applied\ load\ corresponding\ to\ SLS$

$P_{ULS} = applied\ load\ corresponding\ to\ ULS$

$s = spacing\ of\ reinforcement, mm$

$SLS = servicibility\ limit\ state$

$T_g = glass\ transition\ temperature$

$ULS = ultimate\ limit\ state$

$UTS = ultimate\ tensile\ strength, MPa$

$V_c = (punching)\ shear\ strength\ of\ concrete$

$V_n = nominal\ shear\ strength\ of\ section$

$V_s = shear\ strength\ contribution\ from\ steel$

$w = crack\ width\ , mm$

$y_t = distance\ from\ neutral\ axis\ of\ overall\ section\ to\ extreme\ tension\ fibre$

$\beta = ratio\ of\ distance\ from\ neutral\ axis\ to\ extreme\ tensionfibre\ to\ distance\ from\ neutral$

$axis\ to\ centre\ of\ tensile\ reinforcement$

$\beta_1 = reduction\ factor\ for\ concrete\ strength = 0.85\ for\ f'c \leq 28MPa$

$= 1.064 - 0.00714 f_c'\ for\ 28 < f'c < 56MPa$

$= 0.65\ for\ f'c \geq 56MPa$

$\beta_d = reduction\ factor\ for\ deflection\ calculation$

$\Delta = deflection$

$\varepsilon_c = compressive\ strain\ in\ concrete$

$\varepsilon_{c0} = concrete\ compressive\ strain\ at\ peak\ stress$

$\varepsilon_{cu} = ultimate\ concrete\ compressive\ strain$

$\varepsilon_{sp} = concrete\ spalling\ strain$

$\rho_f = reinforcment\ ratio$

$\rho_{fb} = balanced\ reinforcement\ ratio$

1 Introduction

Bridges provide critical transportation links in New Zealand's state highway network, occurring on average every 2.5km. Much the state highway network is in close proximity to the coastline, unfortunately leading to increased corrosion risk for concrete bridges reinforced with steel. Sea spray and salt-laden aerosols are able to reach the steel through cracking in the concrete. Weathering of the concrete also adds to the risk of corrosion. Bridges cannot easily be upgraded during their service life due to inevitable traffic disruptions (NZTA, 2012) which, along with optimizing costs, is one of the reasons 'life cycle' approach is needed when considering bridge design.

Many millions of dollars are spent all over the world every year on bridge replacement and maintenance. In New Zealand alone, highway bridges are estimated to have a replacement value of $6 billion and depreciated value of $3.5 billion (NZTA, 2011). NZTA (2011) states that "Historic, current and forecast maintenance costs are consistently low, at about 0.4% of the bridge replacement value." Even with much lower maintenance than replacement costs for bridges, this is still a very significant cost to NZTA. It is therefore economical to consider low maintenance solutions when designing new bridges.

A significant part of the maintenance work involves repairing and preventing corrosion of mild steel reinforcement. Increasing traffic demand and use of de-icing salts (not common in New Zealand since the early 1980s due to public concern about vehicle corrosion, but used in USA and Canada) as well as bridges located in harsh environments increase the rate of deck deterioration and corrosion of steel reinforcement for bridges. Due to the large costs involved in the maintenance works, authorities have been searching for an alternative to steel reinforcement in bridge decks.

Glass Fibre Reinforced Polymer (GFRP) bars have been developed as an alternative to steel reinforcement for various structural concrete applications. Due to their non-corrodible nature, they have been considered a promising alternative to steel reinforcement in concrete bridge decks in harsh environments where traditional steel reinforcement is prone to corrosion. Much research has been

conducted to investigate the properties and behavior under various conditions of GFRP reinforcement in concrete. GFRP bars can offer benefits of cost and durability in some applications.

Investigation of the use of GFRP reinforcement in bridge decks in harsh environments such as coastal New Zealand is the main motivation for this research project. The bridge deck is identified as the most appropriate application for GFRP when considering both the deck and piers, as it is typical to design the bridge deck so that it remains in the elastic range under lateral loading. Current GFRP technology is not recommended for seismic design by manufacturers and researchers due to its limited ductility so it is unsuitable for pier design. Design recommendations will be made, drawing on findings from the experimental programme as well as existing research on GFRP reinforced concrete members.

Life cycle management (LCM) is a strategy used when managing a structure through its design, construction and service life that aims to improve the overall efficiency in terms of both an economic and engineering point of view. An LCM approach seeks to find an optimum balance considering factors such as cost, profits, risk, quality, durability and sustainability of the structure (fib, 2010). A complete Life cycle analysis is not within the scope of the project, however this would be an appropriate next stage in the research of GFRP reinforced concrete bridge deck applications.

1.1 Objectives

The key objectives of the research are:

1. To better understand and characterise the GFRP bar material through research and materials testing. To identify the current application of GFRP bars as structural reinforcement.
2. To understand the flexural and punching shear behavior of a bridge deck slab reinforced with deformed GFRP reinforcing bars. Comparisons will be made with a typical steel reinforced concrete deck.
3. To verify existing GFRP reinforced concrete design recommendations and make any additional recommendations appropriate to New Zealand bridge deck design based on the results found.

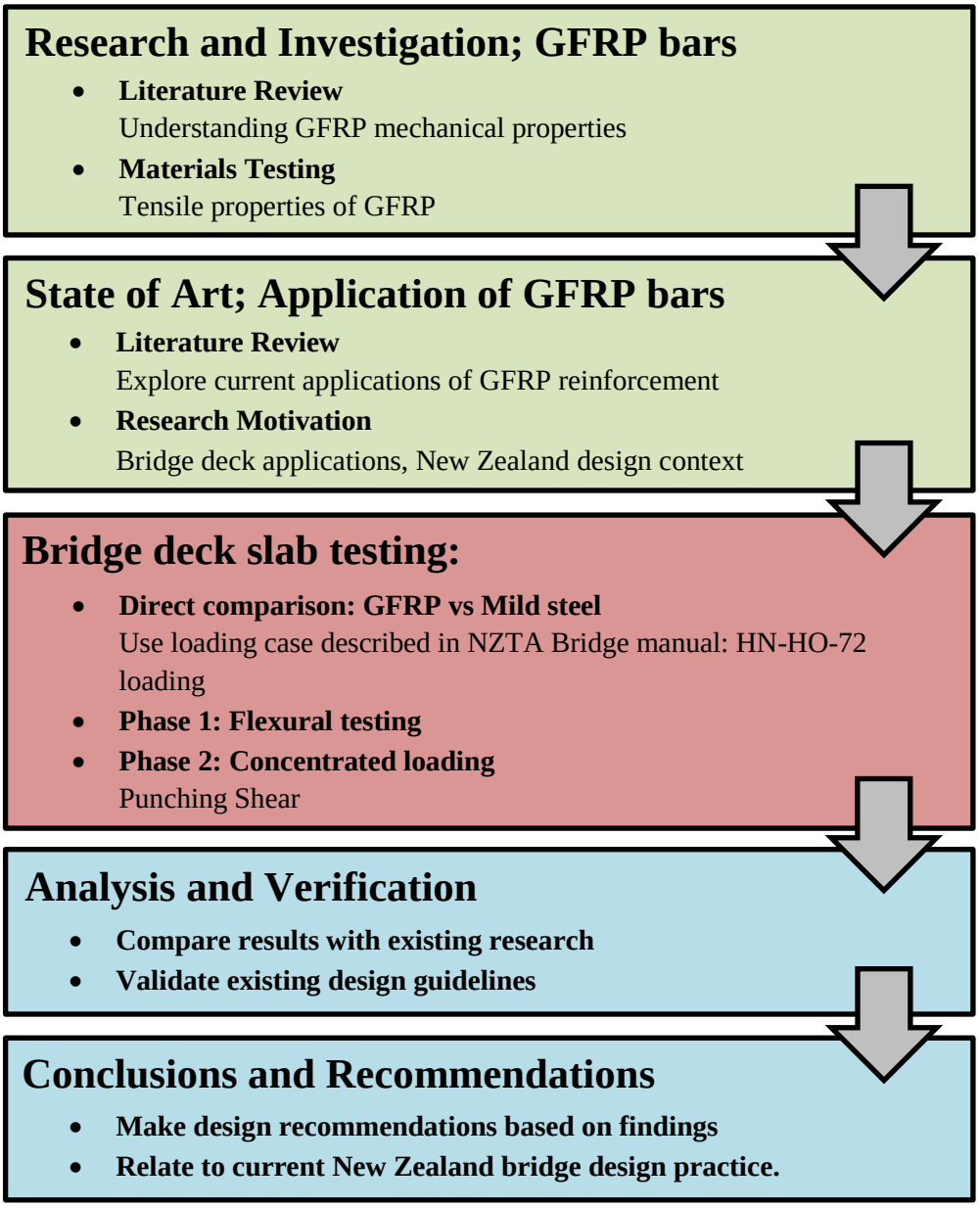

Figure 1-1: Flowchart describing the structure and methodology of the research. The three shades correspond to the three key objectives described in 1.1.

The flowchart presented in figure 1-1 shows the structure of the thesis describing the practical steps undertaken in this research, keeping in line with the three key objectives described above. The first objective is described in the first two boxes of the flowchart which covers understanding existing knowledge surrounding the GFRP bar material and its use in structural applications. Also gaps in the current research are identified to feed into the motivation for this research. The second objective is

covered by the third box in the flowchart which refers to the large experimental component of the research. In this component a GFRP reinforced slab design is compared with a steel reinforced concrete slab design (relatively well understood by structural engineers) as a benchmark for understanding the structural performance of GFRP reinforcement. The final boxes in the flowchart describe the third key objective which involves relating the current research to existing research and design guidelines and also making additional recommendations based on the experimental findings.

2 Literature Review

2.1 Glass Fibre Reinforced Polymer (GFRP) bars

A glass fibre reinforced polymer (GFRP) bar is composed of many tiny continuous glass fibres embedded in a polymeric resin matrix. GFRP bars have been developed for use in various structural applications with the main benefit of being a non-corrodible alternative to steel reinforcing bar. Other benefits of GFRP bars can include high strength and stiffness to weight ratio, resistance to chemical attack, more control over thermal expansion and damping characteristics, good fatigue properties and electromagnetic resistance (Abdalla, 2002). Other common fibre reinforced polymers (FRP) are Carbon (CFRP) and Aramid (AFRP).

While developed to be an alternative to mild steel reinforcing bars, GFRP bars are currently a cost-competitive alternative to stainless steel reinforcing bars which are also used in structures where corrosion of reinforcement is a concern (Feldman, Boulfiza, Zacaruk, Christensen, & Sparks, 2008).

2.2 General GFRP bar Material Characteristics

E-glass or S-glass are the often used for the fibres in GFRP reinforcement and the selection of resins is made based on cost, strength, rigidity and long term stability (Dolan, Bakis, & Nanni, 2001). The fibres provide strength and stiffness to the bar, while the polymer matrix binds the fibres together and transfers stresses between them. To achieve the highest tensile properties, fibres are orientated in the same longitudinal direction as the bar itself, though some products are made with fibres set in many orientations.

Due to the lack of standardized manufacturing procedure, and the attempt to increase bond strength of the bars, a few different types of bar surface have been produced. These include smooth bar surface, ribbing of the bar surface (similar to deformed mild steel), helical fibre wrapping of the bar (either simply bonded to the core or wrapped under tension to deform the bar slightly) and applying a rough coating with sand particles to the bar surface (Katz, 1998), see figure 2-1.

The exact properties of GFRP bars depend on the materials used, dimensions of the bar and quality control and therefore any published information about GFRP should be used in a general sense as it may not be applicable for a certain GFRP bar product.

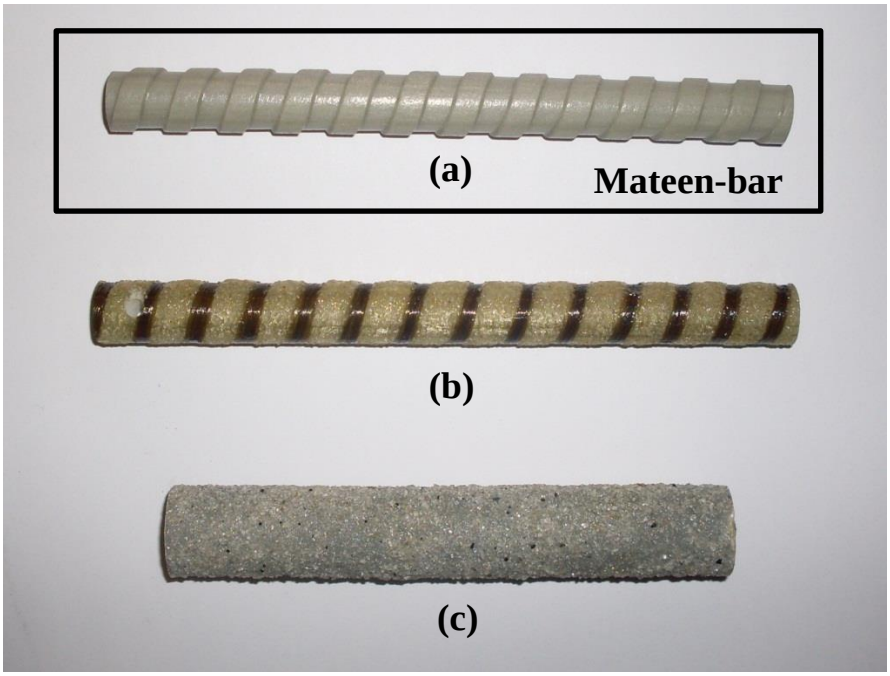

Figure 2-1: Comparison between GFRP bars with different surface types: (a) helical ribbed bar surface, (b) helical fibre wrapping of sand coated bar surface, (c) sand coated bar surface. Note: bar (a) is a sample of Mateen-bar which will be tested as part of this research project.

A comparison of steel reinforcing bars with common types of FRP reinforcement is shown in table 2-1. It can be seen that there is much more variation in the strength properties of all the FRP products than for mild or stainless steel reinforcement. This is due to factors such as fibre volume, type, orientation, resin type and quality control as well as dimensional effects (ACI Committee 440, 2006). Also there is not yet any standardized manufacturing process for FRP bars. In general the GFRP bars exhibit lower strengths than carbon CFRP or AFRP bars, however as GFRP is generally the cheapest of the three has lead both researchers and manufacturers to focus on development and applications for this type of bar. CFRP bars have a high cost as carbon fibres are about 10 to 30 times more expensive than e-glass and the manufacturing process is longer than for GFRP (fib, 2007). Aramid is a generic term for synthetic fibres that have higher tensile strength to weight ratio than both glass and carbon fibres (fib, 2007).

Table 2-1: Usual tensile properties of reinforcing bars (ACI 440.1R-06, AS/NZS 4673: 2001, fib 2007).

	Mild Steel	Stainless Steel	CFRP	AFRP	GFRP
Nominal Yield Stress, MPa	276 to 517	250 to 450	-	-	-
Tensile Strength, MPa	483 to 690	380 to 680	600 to 3690	1720 to 2540	483 to 1600
Elastic Modulus, GPa	200.0	185 to 200	120.0 to 580.0	41.0 to 125.0	35.0 to 51.0
Yield Strain, %	0.14 to 0.25	0.2 to 0.3	-	-	-
Rupture Strain, %	6.0 to 20.0	15.0 to 20.0	0.5 to 1.7	1.9 to 4.4	1.2 to 3.1
Density, kg/m^3	7860	7480 to 8000	1430-1670	1300-1450	1730-2170

2.3 GFRP bar Physical Properties

2.3.1 *Density*

GFRP bars have a density of ~2.0 g/cm^3, much lower than that of steel reinforcing bars at ~8.0 g/cm^3. Reduced weight may reduce transportation costs and makes handling the bars easier on the project site.

2.3.2 *Thermal Properties*

The coefficient of thermal expansion for GFRP bars can vary greatly in the longitudinal and transverse directions depending on the type of glass, resin and volume fraction of fibre. Typical coefficients for thermal expansion are shown in table 2-2. The longitudinal coefficient of thermal expansion is comparable to that of concrete, meaning that thermal incompatibility is unlikely to be any cause for concern when designing GFRP reinforced concrete structures. The transverse coefficient of thermal expansion can be up to around four times greater than the longitudinal direction which may lead to splitting cracks in cases where insufficient cover is provided. It was found that a ratio of concrete cover thickness to bar diameter (c/d_b) of greater than or equal to 2 was sufficient to avoid cracking of concrete up to temperatures of +80°C (Masmoudi, Zaidi, & Gerard, 2005).

Table 2-2: Typical coefficients of thermal expansion for GFRP bars compared with concrete and steel.

Direction	CTE, x 10^{-6}/°C
Longitudinal, α_L	6.0 – 10.0
Transverse, α_T	21.0 – 23.0
Concrete	12.0
Steel	11.0-13.0

In a fire GFRP bars embedded in concrete will not burn, but the resin will soften due to the high temperatures. FRP composites have a glass transition temperature, T_g, above which the resin changes from its stiffer 'glassy' state to a soft rubbery state. The value of T_g depends on the resin type and is usually in the range of 70 to 175°C (fib, 2007). The tensile properties of GFRP decrease above T_g due to a reduction in the bond between fibres. GFRP is not recommended where fire resistance is critical to maintaining structural integrity (fib, 2007).

2.4 GFRP bar Mechanical Properties

2.4.1 *Tensile Behaviour*

GFRP bars have a tensile strength much higher than that of mild steel reinforcing bars. However they do not exhibit any yielding behavior under tensile load, and experience a sudden brittle failure at the ultimate loading point (Kocaoz, Samaranayake, & Nanni, 2005). The bars behave elastically up until failure exhibiting no yield behavior. Ultimate strain of GFRP bars is around 2%, meaning a 1m bar section will stretch approximately 20 mm before rupture. Unlike steel reinforcing bars, the tensile strength of GFRP bars can vary with changes in diameter, reducing by up to 40% proportionally as the diameter increases from 9.5mm to 22.2mm (ACI Committee 440, 2006).

The 22 mm Mateen-bars used in the experimental part of this project have a guaranteed tensile strength 790 MPa. Figure 2-2 shows the stress-strain curves for typical values of mild steel and GFRP reinforcement. The difference in the much steeper initial slope of the steel curve compared to the GFRP curve is due to the much higher elastic modulus value of steel. It can be seen that the GFRP can take considerably more stress than the mild steel, however the strain in the GFRP is far greater than the steel for stress below the steel yield point.

Independent tensile testing of different GFRP bar products is not readily available, however tests must be carried out for manufacturers to have a basis for determining the guaranteed tensile strengths to be included in bar specifications. Guaranteed tensile strength values, as defined by ACI Committee 440, are the mean tensile strength of a sample of test specimens minus three standard deviations.

Testing of 32 bars (4 different bar coating types, with the same diameter) by Kocaoz, Samaranayake and Nanni (2005) showed that a Gaussian distribution can be used to represent the strength of a population of bar specimens. It was also stated that the bar coating may have an effect of the tensile strength of bars.

It is generally understood that with increasing GFRP bar diameter there is a decrease in tensile strength due to shear lag effect, so each bar size (of a particular product type) must have a specified tensile strength attached to it. The tensile modulus is not significantly affected by the cross-sectional size of the bar, but by the volume of fibre contained (Kocaoz, Samaranayake, & Nanni, 2005).

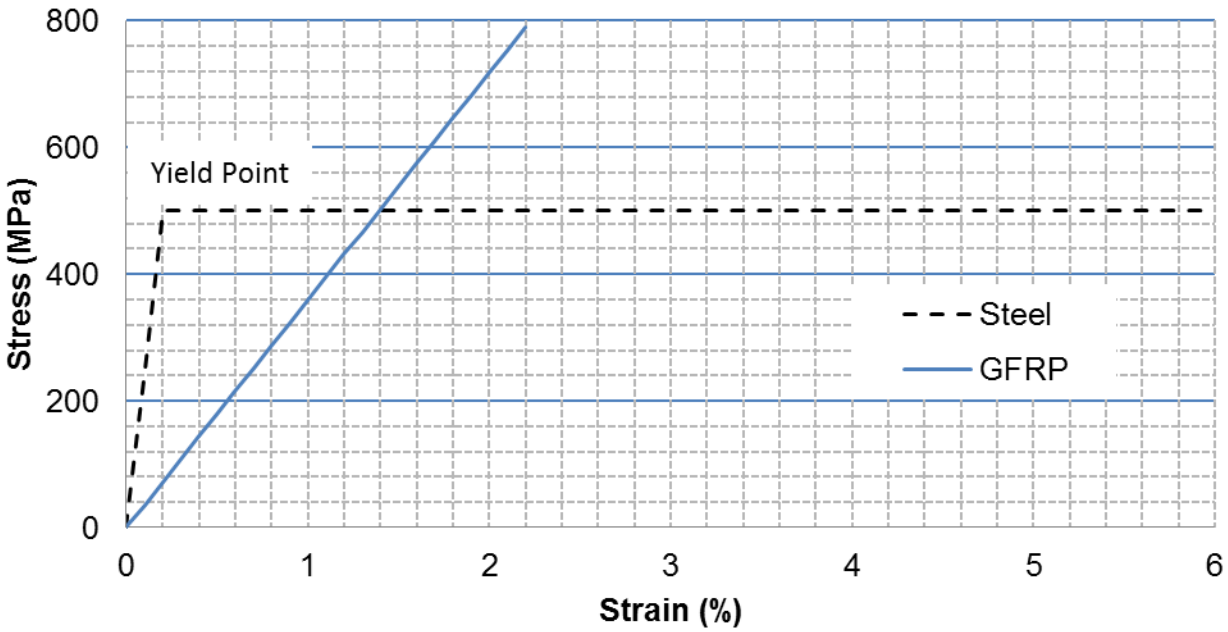

Figure 2-2: Comparison of stress-strain curves for typical values of mild steel and GFRP reinforcement under tension.

2.4.2 *Compressive Behaviour*

The compressive strength of GFRP reinforcement is much lower than the tensile strength resulting in GFRP reinforcement, as it is currently produced, being unsuitable for reinforcement of concrete columns or any other applications where compressive strength would be required (ACI Committee 440, 2006). In general, compressive strengths of GFRP bars are higher for bars with higher tensile strengths, and the compressive modulus of elasticity lower than its tensile modulus of elasticity. Depending on the type of fibre, resin and fibre volume fraction, the compressive strength of a GFRP bar can reach up to 55% of its

tensile strength. The main failure modes for GFRP bars in longitudinal compression are micro-buckling of fibres, transverse tensile fracture and shear failure of fibres without buckling (fib, 2007). In all design guidelines examined, in flexural design the compressive strength of the GFRP bars was neglected, similar to typical flexural design with mild steel reinforcement.

2.4.3 *Shear Behaviour*

Typically no reinforcement exists across layers of glass fibres in a GFRP bar so the interlaminar shear strength depends on the relatively weak polymer matrix of the bar. The shear strength may be increased by offsetting the fibre direction from the longitudinal axis of the bar, which can be achieved by winding fibres transversely to the longitudinal axis of the bar (ACI Committee 440, 2006). This is uncommon practice for most GFRP bar products however. No standard method for determining bar shear strength yet exists to characterize the shear behavior of GFRP bars. For applications where shear strength should be known, strength values should be obtained from the bar manufacturer.

2.4.4 *Bond Behaviour*

The bond performance between a GFRP reinforcing bar and concrete depends on the design, manufacturing process, and environmental conditions as well as the mechanical properties of the bar itself. Much experimental investigation has been done for the bond behaviour of GFRP reinforcing bars. Experiments by Esani, Saadatmanesh and Tao (1996) lead to the authors modifying the ACI 318-71 formula for development length so that the formula for GFRP bar development length is the greater of:

$$l_{db} = 0.0022\left(\frac{A_b f_f}{f_c'}\right) \text{ and } l_{db} = 0.0508 d_b f_f \quad (1)$$

with modifications for top bars and cases where cover is small. A minimum development of 381 mm is prescribed.

As well as the three mechanisms (chemical bond, friction and mechanical interlock) that transfer bond force for typical reinforcement, it was postulated that for GFRP bars, unlike steel, a bond shear failure in the resin could occur as the bond force is transferred to the glass fibres through the resin (ACI Committee

440, 2006). This would lead to fracture between the deformations and the main bar. This was confirmed in experimental tests by Lee et al. (2008) in which steel, sand coated GFRP and helically wrapped GFRP bars were tested for concrete pull-out strength. It was found that bond failure occurred partly on the surface between concrete and resin and partly near the surface between resin and glass fibres. The bond strength of GFRP bars tended to increase at a constant rate as the compressive strength of concrete increased, similar to trends seen for deformed steel bars (though the rate was smaller for the GFRP bars). Soong, Raghavan and Rizkalla (2011) found that the resistance to bar pullout from GFRP bar lugs (deformations) is comparable to that from sand particles bonded to the bar.

2.4.5 *Linear and non-linear creep*

Creep is the inelastic deformation of a material that occurs under sustained load over a long period of time. Many material types are affected by creep to differing degrees including concrete and timber. When the strain capacity is reached creep-rupture will occur, which is the tensile fracture of the material. Figure 2-3 shows the general creep behavior of FRP bars or tendons. Three stages of strain behavior occur: primary secondary and tertiary. The primary stage occurs immediately following load application following an initial period of elastic strain (fib, 2007). The secondary stage represents a constant strain period due to constant stress. If the stress level is kept at a low enough level, the creep of the GFRP bar will be confined to the secondary stage only and the tendons could have unlimited service life (Dolan, Bakis, & Nanni, 2001). In the tertiary stage fibres fail rapidly as the strain capacity is exceeded and the bar will rupture.

The duration of time at which creep rupture occurs under a constant load is known as the endurance time. The endurance time decreases as the ratio of the sustained tensile strength to the ultimate strength of a GFRP bar increases. The endurance time can also decrease under sufficiently adverse environmental conditions, such as high temperature, ultraviolet radiation exposure, high alkalinity, wet and dry cycles, or freezing and thawing cycles. Steel bars will not creep except under extreme temperatures due to fire (ACI Committee 440, 2006).

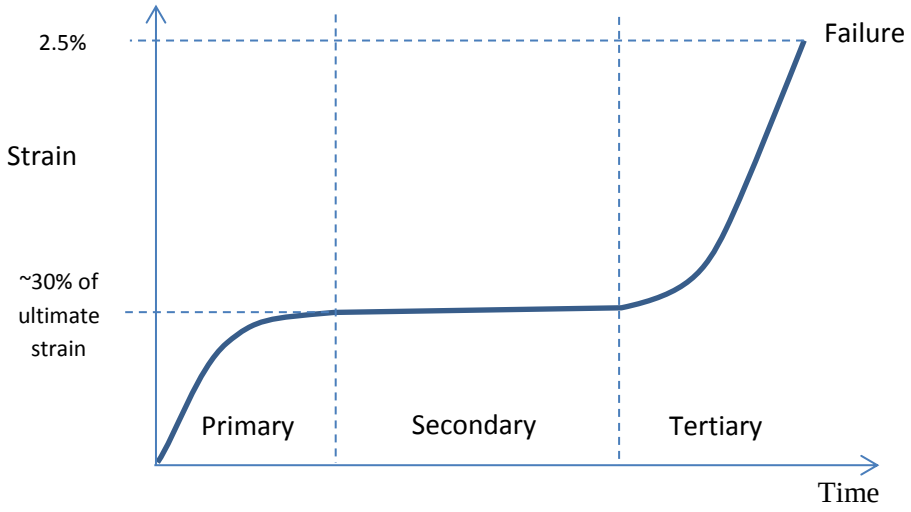

Figure 2-3: Schematic diagram of the three stages GFRP of creep deformation.

When designing with GFRP, the percentage of the ultimate load that the tendons may be loaded to must be known so that the tertiary creep stage will never be reached (Dolan, Bakis, & Nanni, 2001). Dolan, et al. (2001) predicts the useful tensile capacity of a GFRP bar in concrete at 20-30% of its ultimate strength from a series of test with a spring loaded test frame. The ACI Committee 440 (2006) reported that the ratio of stress at creep rupture to the initial strength of a GFRP bar after 50 years has been extrapolated at 0.29 in one study, while it was found to be 0.55 in another. Mufti, et al. (2007) states that 25% of the ultimate tensile stress of the GFRP bars must not be exceeded for non-prestressed reinforcement.

2.4.6 *Fatigue*

There has been extensive research on FRP material fatigue in the last 30 years, but this has been focused mainly on aerospace applications. No fatigue limits have yet been defined for GFRP bars however some studies have shown that GFRP bars achieve a similar fatigue behavior to steel bars (ACI Committee 440, 2006). Recent tests by Noel and Soudki (2014) have shown that the fatigue lives of GFRP bars embedded in concrete were less than those in air by approximately a full order of magnitude as shown in the graph in figure 2-4. This is thought to be due to bond-slip between the concrete and reinforcing bar.

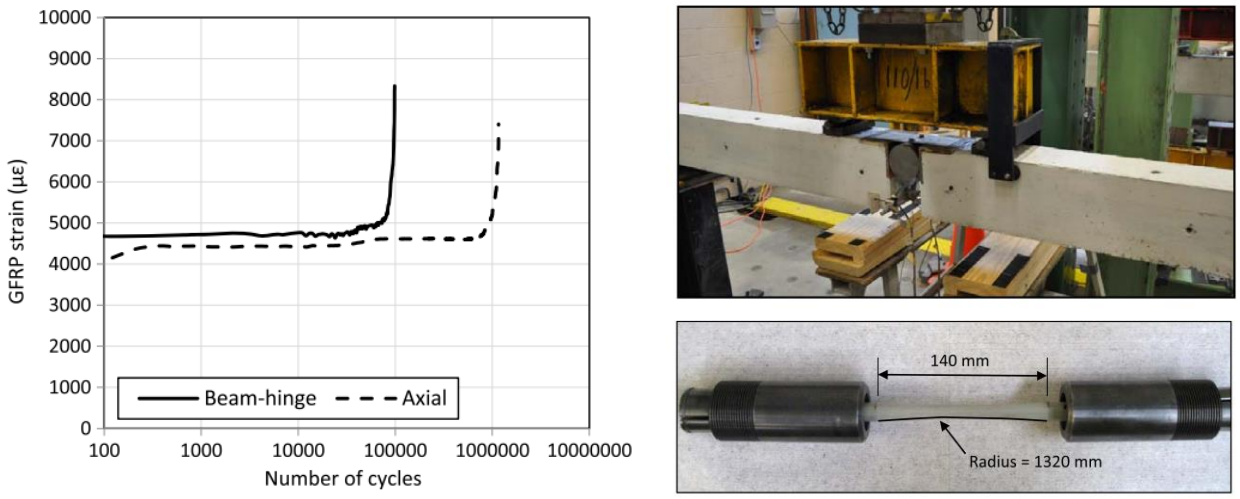

Figure 2-4: Left: Typical change in GFRP strain at maximum load under cyclic loading. Right top: Photo of 'Beam hinge' test set-up; GFRP specimen embedded in concrete. Right bottom: GFRP axial fatigue specimen. Figures from Noel and Khaled (2014).

2.4.7 *Durability*

Many factors affect the durability of GFRP bars including moisture, ultraviolet exposure, elevated temperature, alkaline or acidic conditions, and saline solutions (ACI 440). Primarily the concern is for reduction of tensile and bond properties.

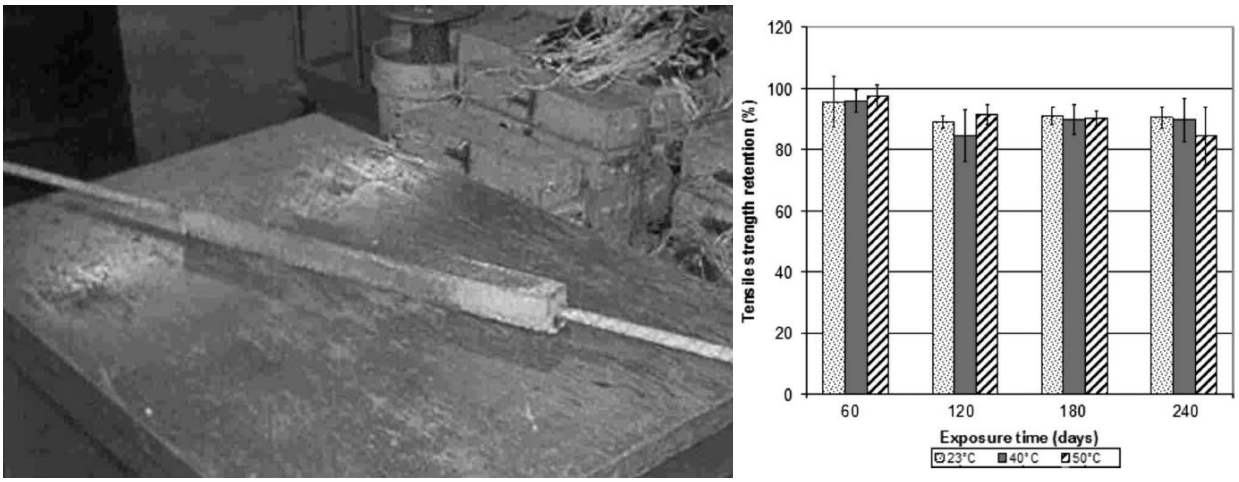

Figure 2-5: Left: GFRP bar specimen wrapped in cement mortar before being exposed to tap water and tested by Robert, Cousin and Benmokrane (2009). Right: Tensile strength retained by GFRP bars after conditioning in moist concrete at three different temperatures.

Overestimation of the adverse effect of moisture on GFRP bar durability has led to conservative design of GFRP reinforced structures. Research by Robert, Cousin and Benmokrane (2009) has shown that the concrete environment is generally not as harsh as the alkaline solutions used in testing. GFRP bar samples

embedded in concrete were exposed to tap water at 23, 40 and 50ºC to accelerate the effect of a moist concrete environment (See figure 2-5). The bars were then tested to determine the resulting reduction in tensile strength. The experiments also demonstrated that even at high temperatures (increasing from 40 to 50ºC over 240 days) the reduction of tensile strength was minor, with a strength reduction of only 10-16% of the original tensile strength. Scanning electron microscopy (SEM) observations before and after aging revealed no microstructural degradation of the bar surface which was contradictory to earlier testing by Benmokrane and Wang (2002) in which GFRP bars were directly immersed in an alkaline solution.

2.5 Structural Concrete Members Reinforced with GFRP

This section comprises an overview of research done on the flexure and shear behaviour of concrete members reinforced with GFRP bars. Both GFRP reinforced beams and two-way slabs have been considered.

2.5.1 *Beams reinforced with GFRP bars*

In the past decade significant developments have been made in understanding the behavior of GFRP reinforced beams. It has been found that a GFRP reinforced beam compared with a steel reinforced beam designed for the same load will behave differently due to the difference in properties of the reinforcement types. For the same area of reinforcement, a GFRP reinforced beam was found to exhibit more deflection than a steel reinforced beam due to the much lower modulus of elasticity of GFRP compared with steel. More strain must occur in the GFRP bars to carry the same amount of tensile stress as the steel bars. As concrete cracks when subject to tensile force, the cracks in the GFRP reinforced beam will be larger also. Subject to bending moments, GFRP reinforced concrete beams behave linearly up until cracking, and then linearly with reduced stiffness (Abdalla, 2002).

Figure 2-6 shows load deflection curves from experimental beam testing carried out by Abdalla (2002). It can be seen that a higher reinforcement ratio leads to higher global stiffness post-cracking and the post-cracking stiffness is also approximately linear. It is also clear that beams reinforced with GFRP have a

significantly lower post-cracking stiffness than the beam reinforced with CFRP. This was attributed to the lower modulus of elasticity of the GFRP bars (42 GPa) than the CFRP bars (147 GPa).

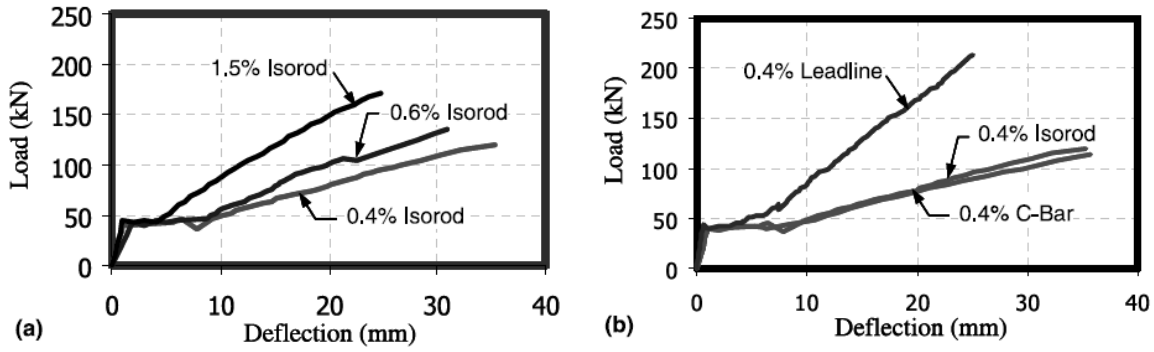

Figure 2-6: Load – deflection behavior of beams tested by Abdalla (2002). a) Effect of reinforcement ratio for GFRP bar (Isorod) reinforced slabs. b) Effect of reinforcement type: Isorod and C-bar are GFRP bar products, Leadline is a CFRP bar product.

Longer beams often failed due to concrete crushing along the top fibre of the beam, rather than rupture of the reinforcement in the bottom of the section.

Empirical design formulae have been developed through studies of the flexural behavior of GFRP reinforced beams. Note that in general, the flexural design formulae of GFRP beams can be applied to one-way slabs also.

For shorter beams, in which failure in shear is most likely, it has been found that the shear failure modes for GFRP beams are similar to that of steel reinforced beams. In this way it has been assumed that summing the contributions of shear reinforcement and concrete is valid in the GFRP case (Guadagnini, Pilakoutas, & Waldron, 2003). However it has been found on more than one occasion that the design approach described by ACI 440 is very conservative in terms of shear reinforcement and applying the steel design approach described in ACI318 is unconservative (Yost, Gross, & Dinehart, 2001) (Deitz, Harik, & Gesund, 1999) . Due to this several equations have been developed to more accurately predict the shear capacity of a GFRP reinforced beam.

It was discovered that members failing by shear (for members containing stirrups) gave more warning of impending failure than members failing in flexure; both in terms of flexural concrete crushing and flexural bar failure (Bentz, Massan, & Collins, 2010).

2.5.2 *Two-way slabs reinforced with GFRP bars*

Recently a number of researchers have investigated the behaviour of FRP reinforced slabs, including GFRP. A significant portion of the existing experimental research on GFRP reinforced slabs has focused on concentrated loading of the slab to simulate either a vehicle load on a bridge deck (or equivalently a column reaction in a typical column-slab connection for a building). Investigations have found that punching shear will typically govern as a failure mechanism over bending for a GFRP reinforced slab loaded in this way (El-Gamal, El-Salakawy, & Benmokrane, 2007) (Ospina, Alexander, & Cheng, 2003) (El-Ghandour, Pilakoutas, & Waldron, 2003) (Hassan, Ahmed, & Benmokrane, 2013) (Dulude, Hassan, Ahmed, & Benmokrane, 2013) (Bouguerra, Ahmed, El-Gamal, & Benmokrane, 2011).

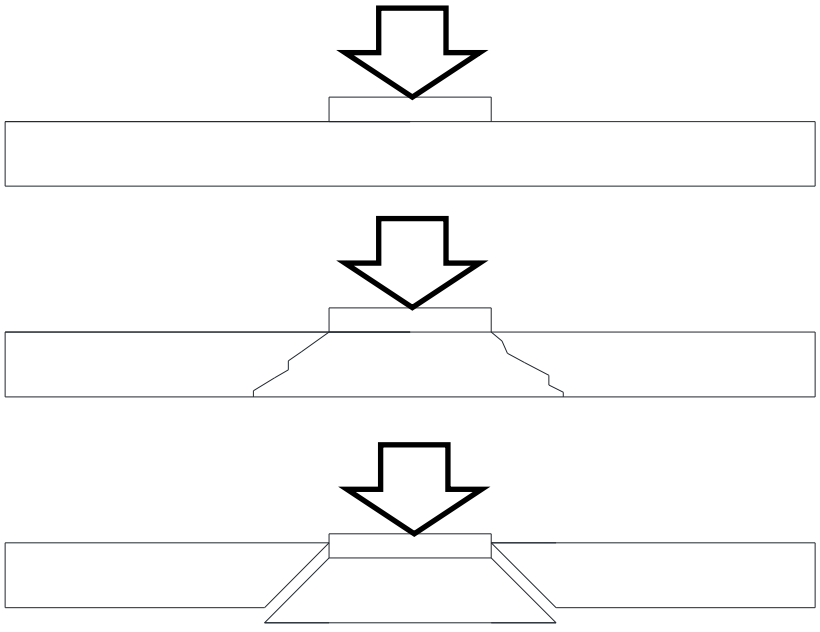

Figure 2-7: Schematic drawing showing a punching failure occurring. Top: concentrated load. Middle: Inclined cracks forming out from the loaded area. Bottom: Failure occurring as a cone shaped wedge of concrete separates from the slab.

Punching shear is a brittle shear failure mechanism specific to load bearing flat slabs and is caused by a high stresses surrounding a concentrated load or support. Punching shear can be problematic in buildings for column-slab connections and, as in the case of a bridge deck, surrounding concentrated loads on flat slabs. An inclined crack forms immediately surrounding the load area until brittle failure occurs with a 'punching cone' of concrete separating from the rest of the slab (figure 2-7). The flexural reinforcement may or may not yield before the slab fails in punching shear (fib, 2001). Slab thicknesses (where punching failure is a possibility) are often determined based on the punching capacity of the slab.

Due to the complexity of the problem, there is no generally agreed upon model used for design practice. Many empirical models for predicting punching shear strengths have been proposed, but they are not necessarily based on how the load is transferred in the slab. Analytical models have been developed to more accurately model the punching mechanism such as those by Menetrey, Hallgren and Staller (fib, 2001). The 1996 analytical model by Menetrey suggests that there is a link between punching and flexural behaviour which depends on the assumption of crack inclination angle (fib, 2001). Figure 2-7 shows the load transfer in a punching shear mechanism as described in the model proposed by Menetrey. Analytical models such as this are complex and not ideal for use by practicing engineers for design or analysis.

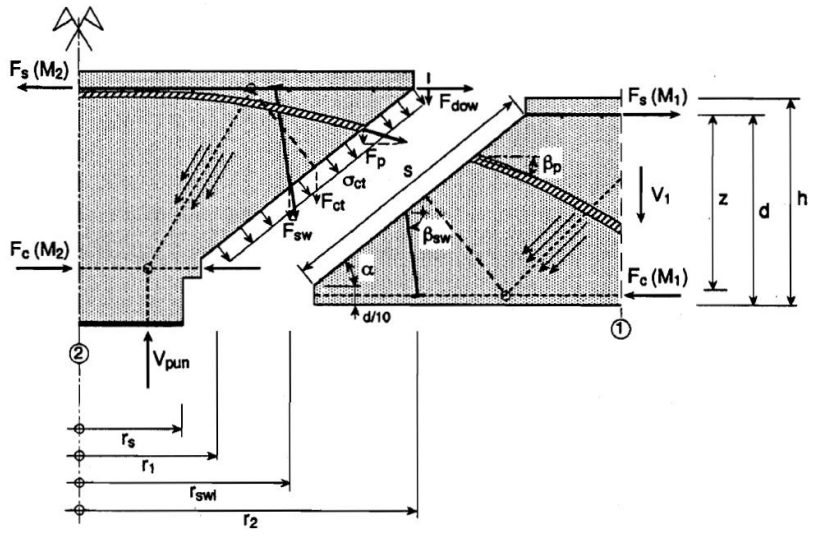

Figure 2-8: Representation of a punching shear failure from a general reinforced slab (fib, 2001).

Many different empirical formulae for V_c have been published. In the most basic form V_c is generally a function of the concrete compressive strength (f'_c), the critical perimeter surrounding the load footprint (b_0, at a specified distance away from the load area such as 0.5d), the effective depth of the section (d) and the tensile reinforcement ratio (ρ_f).

$$V_c = f(f'_c, b_0, d, \rho_f) \tag{2}$$

The punching shear design formula given by in ACI 318-05 is as follows:

$$V_c = 0.33\sqrt{f'_c} b_0 d \tag{3}$$

The difference in shear behavior of GFRP and steel reinforced slabs is due to the difference in elastic modulus, ultimate tensile strength and bond for each material. Some models based on experimental testing have been developed to empirically predict the punching shear of GFRP slabs. Generally, existing research has been done by comparing GFRP reinforced concrete slabs having the equivalent reinforcement area of a steel reinforced slab. This leads to inferior structural behaviour of the GFRP reinforced deck due to the modulus of elasticity of GFRP being a quarter of that of the steel (Lee, Yoon, Cook, & Mitchell, 2009). The ACI 318-05 formula was developed for two-way slabs reinforced with conventional steel and, due to the relatively low modulus of elasticity of GFRP, it cannot be directly used to predict the punching capacity of GFRP reinforced concrete slabs.

A modified version of this formula is given by ACI 440.1R-06:

$$V_c = \frac{4}{5}\sqrt{f'_c} b_0 k d \tag{4}$$

where and kd is the cracked transformed section neutral axis depth. d is the depth of the reinforcement and k depends on the reinforcement ratio and the modular ratio between the GFRP reinforcement and the concrete:

$$k = \sqrt{2 \cdot \rho_f \cdot n_f + \left(\rho_f \cdot n_f\right)^2} - \rho_f \cdot n_f \tag{5}$$

Table 2-3 contains a selection of models proposed to calculate punching shear strength of GFRP reinforced slabs (and two for a typical steel reinforced slab).

Table 2-3: Punching strength capacity models for reinforced concrete slabs.

JSCE (1997)	$V_c = \beta_d \beta_p \beta_r f_{pcd} b_{0:0.5d} d$ $\beta_d = \left(\frac{1000}{d}\right)^{1/4} \leq 1.5$ $\beta_p = \left(100\rho_f E_f / E_s\right)^{1/3} \leq 1.5$ $\beta_r = 1 + 1/(1 + 1.25u/d)$ $f_{pcd} = 0.2\sqrt{f_c'} \leq 1.2\ MPa$ $u = perimeter\ of\ loaded\ area$
El Ghandour et al. (1999)	$V_c = 0.33\sqrt{f_c'}\left(\frac{E_f}{E_s}\right)^{1/3} b_{0;0.5d} d$
El Ghandour et al. (2000)	$V_c = 0.79\left[100\rho_f\left(\frac{E_f}{E_s}\right)\left(\frac{0.0045}{\varepsilon_y}\right)\right]^{1/3}\left(\frac{f_c'}{25}\right)^{1/3}\left(\frac{400}{d}\right)^{1/4} b_{0;1.5d} d$
Matthys and Taewre (2000)	$V_c = 1.36\frac{\left(100\rho_f \frac{E_f}{E_s} f_c'\right)^{1/3}}{d^{1/4}} b_{0;1.5d} d$
Ospina et al. (2003)	$V_c = 2.77\left(\rho_f f_c'\right)^{1/3}\sqrt{\frac{E_f}{E_s}} b_{0;1.5d} d$
El-Gamal et al. (2005)	$V_c = 0.33\sqrt{f_c'} b_{0;0.5d} d\alpha$ $\alpha = 0.5\left(\rho_f E_f\right)^{\frac{1}{3}}\left(1 + \frac{8d}{b_{0;0.5d}}\right)$
ACI 440.R1-06 (2006)	$V_c = \frac{4}{5}\sqrt{f_c'} b_{0;0.5d} k d$ $k = \sqrt{2\rho_f n_f - \left(\rho_f n_f\right)^2} - \rho_f n_f$
ACI 318-05 (2005) (steel reinforced concrete design)	$V_c = 0.33\sqrt{f_c'} b_{0:0.5d} d$
AS/NZS 3101 (2006) (steel reinforced concrete design)	$V_c = v_c b_0 d$ Where v_c is smallest of: a) $v_c = \frac{1}{6} k_{ds}\left(1 + \frac{2}{\beta_c}\right)\sqrt{f_c'}$ b) $v_c = \frac{1}{6} k_{ds}\left(\frac{\alpha_s d}{b_{0;0.5d}} + 1\right)\sqrt{f_c'}$ c) $v_c = \frac{1}{3} k_{ds}\sqrt{f_c'}$

	$\alpha_s = 20, \qquad k_{ds} = \sqrt{\frac{200}{d}} \qquad \beta_c = \frac{long\ side\ of\ load\ area}{short\ side\ of\ load\ area}$

Each of these models has a similar basic form with additional factors based on experimental tests carried out by the authors and from literature.

2.5.3 *Ductility of GFRP reinforced concrete members*

Ductility is inelastic energy dissipation for a structure allowing redistribution of internal forces when the structure is near failure. This contributes to the robustness of a structure by allowing the load to travel through an alternative load path in the case of a localised failure. In standard reinforced concrete design practice a ductile failure mechanism is generally preferred and is achieved by relying on the ductility of steel. The GFRP bars themselves cannot be relied upon to provide any ductility as due to the linear stress-strain behaviour up until rupture, the bars have limited inelastic energy dissipation. Ductility must therefore be designed into the system as a whole to avoid a sudden brittle failure. Robustness in GFRP reinforced concrete member can be created by introducing redundancy through the use of bigger overstrength factors in design. Due to their low modulus of elasticity GFRP bars will stretch approximately 20 mm per metre of original length before failure giving warning by producing large deflections and wide cracks.

Ductility is often expressed in terms of deformation by calculating the ratio of ultimate deformation to yield deformation. As GFRP reinforced members display no yield behavior this definition is not valid to describe GFRP reinforced concrete ductility. Another method to describe ductility considers energy absorption which often calculated as the ratio of inelastic to total energy absorption of the system. The difficulty with a GFRP reinforced member is determining how much of the total energy is inelastic. Grace et al.(1998) suggested a modified method for determining a ductility value which does not require existence of a yield point. The method results in a rating of the member failure type as ‘ductile’, ‘semiductile’ or ‘brittle’. Figure 2-8 shows visually the regions of the area under the load – deflection curve which are used to calculate the energy ratio. The boundary between elastic and inelastic energy is

the theoretical path that the load-deflection curve would take if it was unloaded immediately before the point of failure. It is clear from the ductility classification that members exhibiting more inelastic energy absorption are more ductile.

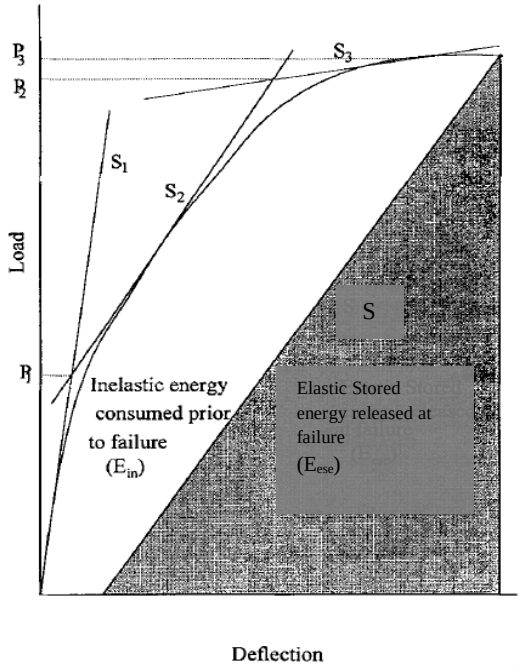

$$Energy\ Ratio = \frac{E_{in}}{(E_{in} + E_{ese})}$$

Ductility Classification:

energy ratio > 75%	"Ductile"
74% > energy ratio > 70%	"Semi-ductile"
energy ratio < 69%	"Brittle"

Figure 2-9: Graph showing definition of inelastic and elastic energy, and how ductility is classified using the calculated "energy ratio". Figure reproduced from Grace et al. (1998).

2.6 Design Guidelines for Structures Reinforced with GFRP bars

In the past two decades considerable research has been undertaken to better understand the properties of various GFRP bar products and to develop guidelines for their use in structural applications. In general, these guidelines have evolved by making modifications to existing steel reinforced concrete codes based on experimental testing of the material. GFRP bars behave very differently to steel bars so there are questions surrounding the appropriateness of this method of design guideline development. Design with GFRP reinforcement is more complex than a direct substitution of steel reinforcement with GFRP and a shift in thinking is required for practicing engineers who are used to designing with steel reinforcement. The most notable differences between the design of GFRP and steel reinforced structures is the considerably low modulus of elasticity and lack of any yield behaviour in the GFRP bars.

The United States, Europe, Canada and Japan have developed their own design guidelines (ACI Committee 440, 2006) (fib, 2007) (Fico, 2008). In general these guidelines are governed by serviceability limit states, considering stress limits and cracking and deflection limits.

European design guidelines were born out of the EUROCRETE project which was a collaborative research program from 1993 to 1997. Partial safety factors take into account both short and long term behaviour of FRP reinforcement, but the guidelines give no consideration of designing for a dominant failure mode (Fico, 2008).

Japanese design guidelines are based on modified steel reinforced concrete code of practice after experimental and analytical work. The guidelines consider material and member safety factors but also give no indication of the expected failure modes (Fico, 2008).

Canadian guidelines are available for both reinforced of prestressed FRP reinforcement. They do consider failure modes and specify a compressive failure except in some cases such as T-beam design where GFRP rupture is allowed as a very large amount of GFRP would be required to achieve compressive failure. (Mufti, et al., 2007) (Fico, 2008)

United States design guidelines are based on modifications of the American Concrete Institute (ACI) steel code of practice and include knowledge gathered from worldwide research and field applications. They accept both compressive (concrete crushing) and tensile (FRP bar rupture) failure mode but strength reduction factors vary depending on the expected failure mode (ACI Committee 440, 2006). The recommendations in the guidelines are intended to be conservative (Fico, 2008). The ACI 440.1R-06 design guidelines have been used as a basis for the design of the GFRP slab specimen detailed in chapter 4.

2.7 Current GFRP use in structures

Currently there is widespread use of GFRP bars as concrete reinforcement throughout the world. Hundreds of structures have been built showcasing the potential for GFRP reinforcement to be used in

further applications, and extensive studies have been undertaken to determine the field performance of such structures. Applications such as bridge decks, parking garages and marine structures have been built with GFRP bars (El-Salakawy, Benmokrane, & Desgagne, 2003).

This has created the need to develop design procedures for the use of GFRP reinforcement. The United States, Europe, Canada and Japan have developed their own design guidelines. In general, these guidelines have evolved by making modifications to existing steel reinforced concrete codes based on experimental testing of the material.

Two case study bridges deck systems using GFRP reinforcement were examined to determine the suitability of these structures in certain environments. GFRP reinforcement has become a more acceptable alternative for use in bridge decks due to its light weight and non-corrosive properties when compared to steel reinforcement. The existing high costs associated with construction with GFRP reinforcement are expected to reduce should larger commercialisation of GFRP production occur in future.

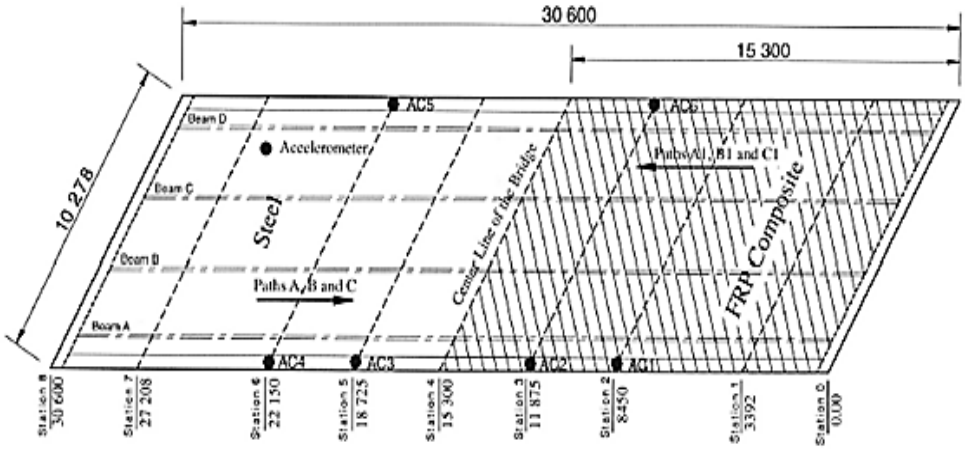

Figure 2-10: Plan view of Wotton bridge showing the two halves of bridge deck reinforced with different materials (El-Salakawy, Benmokrane, & Desgagne, 2003).

2.7.1 *Wotton Bridge*

Wotton Bridge, in Quebec, Canada, is essentially a full-scale long term test comparing the performance of GFRP reinforcing bars to conventional steel reinforcing bars. The bridge was completed in October 2001

and opened for traffic use. One half of the bridge has steel reinforcement, while the other is reinforced with sand coated FRP composites as shown in figure 2-10. Most of the reinforcement in the second half is GFRP, however the reinforcement for the bottom of the slab in the transverse direction is Carbon fibre

reinforced polymer bars (CFRP). Figure 2-11 shows V-Rod samples, the GFRP bar type with sand coated exterior used in Wotton Bridge. Table 2-4 shows the reinforcement configuration for each half of the bridge.

Figure 2-11: Samples of the sand coated GFRP product used in Wotton Bridge. Photo credit to the manufacturer, Pultrall inc.

Table 2-4: Reinforcement configuration of Wotton Bridge. Reproduced from El-Salakawy, Benmokrane, & Desgagne (2003).

Type of bar	Main (transverse) direction		Secondary (longitudinal) direction		Overhang (transverse), top
	Top	Bottom	Top	Bottom	
Steel	No. 15M at 150 mm (ρ = 1.00%)	No. 15M at 150 mm (ρ = 0.85%)	No. 15M at 225 mm (ρ = 0.67%)	No. 15M at 150 mm (ρ = 0.57%)	No. 15M at 75 mm (ρ = 2.00%)
FRP	No. 16 at 150 mm (glass, ρ = 1.00%)	3 No. 10 at 90 mm (carbon, ρ = 1.00%)	No. 16 at 165 mm (glass, ρ = 0.90%)	No. 16 at 165 mm (glass, ρ = 0.76%)	No. 16 at 75 mm (glass, ρ = 2.00%)

The bridge consists of a single span of 30.6m supported on four reinforced concrete I-beams as shown in figure 2-12. The deck has a width of 10.3m and slab depth of 0.2m. The design of the FRP reinforcement followed the new Canadian Highway Bridge Design Code (Mufti, et al., 2007) using the relevant FRP properties in place of those for steel.

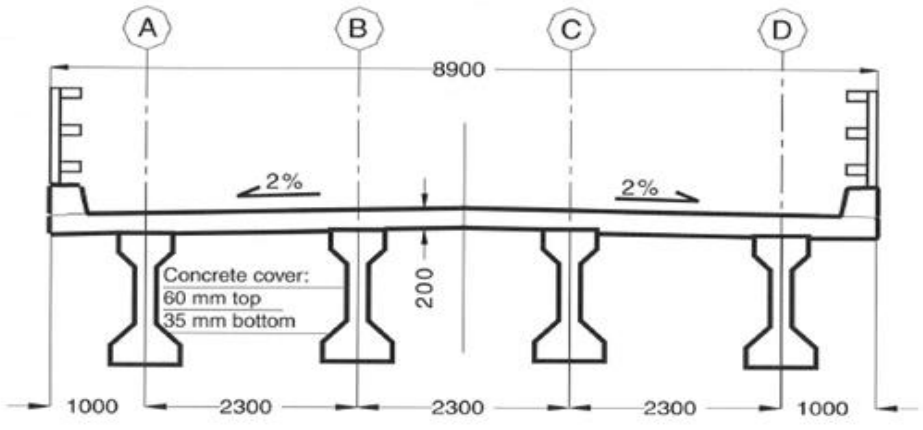

Figure 2-12: Cross-section of Wotton Bridge.

The bridge was fitted with strain gauges at critical locations in order to record the field performance of the bridge. A field test (proof loading) was performed after construction of the bridge. A truck was placed statically on the bridge to model six different paths, and then another was added in two cases to achieve the worst case loading combination. Following the field tests the internal temperature and the strain data of the bridge was monitored for a year. Figure 2-12 shows deflection data collection occurring as trucks are driven slowly across the bridge.

Test results showed that the FRP portion of the bridge deck behaved very well. Deflections were well within the limits set by the Canadian code and maximum recorded strains for the static truck loading were only 0.13% of the ultimate for FRP and just 4% for the service load over one year. Strain values in the concrete due to truck loads were significantly lower than the predicted cracking strain (El-Salakawy, Benmokrane, & Desgagne, 2003). Ongoing test data will be valuable to allow direct comparison between steel and FRP reinforced bridge decks.

Figure 2-13: Deflections measurements are taken for Wotton Bridge in Canada as it is statically loaded with trucks (El-Salakawy, Benmokrane, & Desgagne, 2003).

2.7.2 *US Highway 151*

The US highway 151 bridge deck is relevant to this research project as a case study from a cost analysis perspective. The main objective for building this bridge, and an adjacent twin bridge reinforced with only steel reinforcement, was to compare constructions costs and methods of the two bridges rather than long term effects.

The bridge is almost entirely reinforced with GFRP, with a small amount of steel used also. It should be noted that while this bridge reinforcement was largely GFRP, deck panels and grids made from GFRP were used in the design as well as bars. The bridge deck consists of two 32.7m continuous spans supported on five reinforced concrete I-beams. The deck has a width of 12.9m and slab depth of 0.216m.

Although the initial material cost for the GFRP reinforced deck was 60% higher than the steel reinforced deck (approximately $632,000 compared with $392,000) the construction time for the GFRP deck was considerably faster than the steel deck (Berg, Bank, Oliva, & Russel, 2006). The rate of concrete placement on the GFRP reinforced bridge deck was 51.15m^3 per hour compared to 29.05 m^3 per hour for the steel reinforced deck. This meant that the GFRP deck was able to reduce construction costs by 57% compared to steel. It is expected that the high initial costs for a similar bridge may be reduced in the future as there is increased demand for FRP products and they are produced on a larger scale.

Additionally, long term cost savings due to decreased need for maintenance works or increased service life of the bridge deck are also anticipated to benefit the life cycle costs of the GFRP reinforced bridge deck (Berg, Bank, Oliva, & Russel, 2006). Long term monitoring of this bridge and its twin will be conducted to determine comparisons between the long term behaviour of both GFRP and steel reinforced bridge decks.

3 Experimental Tensile Testing

3.1 Introduction

This chapter details the preparation and findings of experimental tensile testing on a series of GFRP bar samples in four bar sizes. The objectives of this testing are to:

1. Understand and overcome the difficulties of testing GFRP bars in tension
2. Determine the Tensile Modulus of Elasticity, E of the bars by testing the bars in tension.
3. Determine the Ultimate Tensile Strength, UTS by continuing the tests until the bars failed.
4. Compare the strength of different bar sizes.

Pultron Composites Ltd supplied samples of GFRP bar to the University of Canterbury (UC). Mateen-bar is the glass fibre reinforced polymer (GFRP) product produced by Pultron. The bars are manufactured by pultrusion; a continuous process of manufacture where strands of glass fibres are drawn through a bath of resin and then shaped resulting in a constant cross-section. Though the exact details of the fabrication of the bars are unknown this was not necessary for the testing conducted. The surface deformations (similar to a deformed steel reinforcing bar) are added to the bar, leaving a helical indentation on the surface. Table 3-1 shows a comparison between steel and GFRP reinforcing bar properties, including specific properties for Mateen-bar.

Table 3-1: Comparison of Mateen-bar properties with those of typical steel rebar and GFRP bar. Table taken (with Mateen-bar properties added) from ACI 440.1R-06.

	Steel	GFRP	Mateen-bar
Nominal Yield Stress, MPa	276 to 517	N/A	N/A
Ultimate Tensile Strength, MPa	483 to 690	483 to 1200	550-750 (guaranteed)
Elastic Modulus, GPa	200.0	35.0 to 51.0	49-53
Yield Strain, %	0.14 to 0.25	N/A	N/A
Rupture Strain, %	6.0 to 12.0	1.2 to 3.1	2.5

GFRP bars are considerably weaker in compression than tension, and must be gripped in an unconventional manner to perform tensile testing so that the jaws of the testing machine do not crush the specimen (unlike steel which can be gripped directly). As the process of determining the tensile strength and modulus is fairly complicated, repeatability and detailed records of testing method are important. Premature failure is possible due to stress concentrations at the anchorage points, so an adequate grip should allow failure to occur in the middle of the specimen during testing (ACI Committee 440, 2006). This is typically done by constructing a test specimen consisting of the GFRP in a steel tube (that can be gripped by the testing machine) with a cementitious grout or epoxy resin surrounding the bar to bond the two together. ASTM International provides "ASTM D 7205 - Standard Test Method for Tensile Properties of Fiber Reinforced Polymer Matrix Composite Bars" which was used as a guideline for the testing (ASTM Committee D30, 2006). The ideal failure mode of the GFRP bar is a splitting of the bar which ends in rupture (S. Kovaoz, 2005).

3.2 Samples and Testing Method

3.2.1 *Sample Preparation*

Tensile testing for ultimate tensile strength and tensile modulus of elasticity were performed on 40 bars. A tensile testing sample consisted of a steel tube grouted to either end of the Mateen-bar as shown in figure 3-1. The steel tube was able to be gripped by the jaws of the testing machine and successfully transfer the force to the bar through the bond created by the grout inside the tube and surrounding the GFRP.

Some samples were sent 'ready to test' with the appropriate steel grippers epoxied to the bar ends, and a further set of samples were sent as plain bars for UC to assemble for testing. The results for the 'ready to test' sample tests are not presented here, as those samples were used to become familiar with the testing procedure before preparing the actual samples.

UC was supplied with forty plain bar samples in the product sizes as given in table 3-2.

Table 3-2: Summary of plain bar samples received from Pultron.

Nominal Diameter (mm)	Root Diameter (mm)	# samples sent
10	9.2	10
12	11.2	10
16	15.2	10
22	21.2	10
Total No. samples sent		40

UC was required to make up test specimens using the plain bars. This was done following guidelines provided by Pultron. *ASTM D 7205 – Standard Test Method for Tensile Properties of Fiber Reinforced Polymer Matrix Composite Bars* was used as a guide for preparation and tensile testing, though the reproducibility of testing procedure and results was considered to be paramount.

Table 3-3: Summary of specimen dimensions.

GFRP bar nominal diameter (mm)	Overall specimen length (mm)	GFRP bar length (mm)	Steel tube			
			Type	Outer diam. (mm)	Inner diam. (mm)	Length (mm)
10	1300	1300	25nbx3.2	33.7	25	300
12	1300	1300	25nbx3.2	33.7	25	300
16	1500	1500	32nbx3.2	42.4	32	400
22	1500	1500	32nbx3.2	42.4	32	400

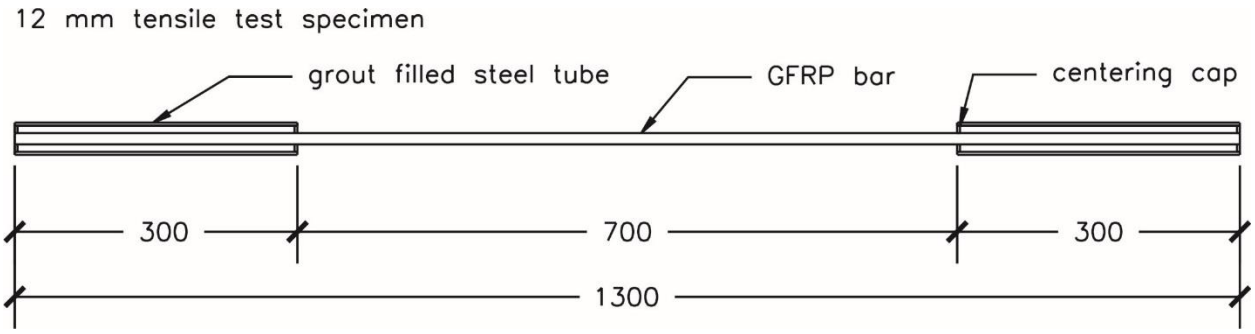

Figure 3-1: Drawing of 12 mm tensile testing specimen. All other specimens dimensions vary as per Table 3-3.

Care was taken to ensure the following:

- Bars were aligned in the centre of the steel tube using plastic guides, to ensure the grout was evenly distributed around the bar and the test would be purely tensile.

- The grout was poured so that it filled the entire tube to ensure maximum available bond length was achieved.
- Safety precautions against the hazard of broken glass fibres were used (Detailed in 3.2.2)

Figure 3-2: Wooden stand with steel tubes inserted into drilled holes. Plastic caps with holes drilled through the centre to act as centering guides for GFRP bars.

The samples were prepared using the following method:

1. Bars were cut to length to ensure that the minimum bar lengths were achieved. Table 3-3 shows the specific lengths and dimensions for bar and tube for each specimen type. Note that the required length to use the safety cover effectively was longer than minimum required lengths but was not maintained at 40 times the diameter as in other independent tests of Mateen-bar. This should be noted when using the results of this test series.
2. Steel tubes were cut to length, and cleaned with a wire brush (internally) and turpentine to ensure no burrs or dirt would hinder the grout from bonding the steel.
3. A wooden stand was prepared to hold the steel tubes vertically while grout was poured (figure 3-2)
4. Plastic caps were pre-drilled using a lathe to ensure high accuracy with central holes (figure 3-2). These were placed over the ends of the bar to guide the bar while the grout was curing.

5. The ends of the bar with cap in place were taped up to prevent grout leaks and the bars inverted and re-inserted into the wooden tray (figure 3-3).
6. The GFRP bars were placed into the steel tubes, ensuring that the ends were protruding slight past the taped holes to make sure they are centred. The caps to put down over the top of the steel tube were fixed with a piece of tape roughly halfway up the GFRP bar for easy fitting following the grout pour (figure 3-4).
7. Grout was mixed following the instructions on the packet. Sika 212 grout was used. The grout was poured by hand into the tube surrounding the GFRP bar using a measuring jug with a (modified) long narrow pouring lip. Plastic caps were fitted (figure 3-4).
8. The grout was allowed to cure overnight, before the steps 5 – 7 could be repeated to attach the second steel tube to the other end.
9. At least 7 days of curing was allowed before testing the specimens. Any tape or spilled grout on the outside of the tube must be removed before testing.

Figure 3-3: Plastic caps inserted into one end of the tube. Ends taped to ensure no grout leaks.

The 16 and 22 mm bar test specimens were prepared, all over two days (to allow curing of one end before inverting) and the 10 and 12 mm bar specimens were prepared at a later stage also over a two day period. The samples were not subjected to specific conditions prior to or during testing. Pultron had advised that

Mateen-bar was not highly sensitive to moisture, so pre-conditioning was not deemed necessary. Prior to testing the samples had been stored in the UC structures lab, nearby to the testing machine.

Figure 3-4: Tubes with lower ends capped and taped, inverted in wooden stand. GFRP bars inserted into steel tubes, note caps taped halfway up bar to allow easy fitting after grout is poured. Finished pour with cap fitted.

3.2.2 *Safety Precautions*

The glass fibres released into the air upon failure of a GFRP bar, may be hazardous to those nearby. To reduce this risk, a safety shield to contain the fibres was fabricated out of two aluminum tubes (figure 3-5). The larger tube was fastened to the bottom steel gripper.

For the first part of the test (when the extensometer was needed) the second slightly smaller tube would sit inside the first. Upon removal of the extensometer, the second tube was moved up, over the top steel gripper and fastened in place. There was more than enough overlapped length to allow for elongation of the bar during testing. After testing, this shield was removed, and GFRP fragments carefully disposed of.

Broken shards of the bar are very likely to cause tiny glass splinters when handled with bare skin. At all stages of handling the Mateen-bar directly, gloves were worn to minimize the risk of glass splinters.

Figure 3-5: Safety shield set-up. Left: Larger tube fastened to bottom steel gripper, with smaller tube sitting inside. Right: Smaller tube extended and fastened to top gripper for continuing testing.

3.2.3 *Testing Method*

All testing was conducted using the UC AVERY testing machine (figure 3-6), in the UC Civil Structures Laboratory. The testing machine did not move with a controlled displacement rate, as specified by ASTM D 7205, but with a controlled loading rate. This was not deemed to be a significant issue due to the elastic behavior of GFRP.

The following method was used to carry out the testing:

The larger part of the safety shield was fastened to the lower steel tube at the end of the specimen. The smaller part was inserted into the larger part.

Depending on the bar diameter to be tested, a different loading range was chosen. (e.g. 200 kN load range for 12 mm bar).

Figure 3-6: Left: Extensometer (50mm gauge length) attached to exposed portion of bar. Right: The Avery Universal Testing Machine in the University of Canterbury Civil Structures Laboratory.

A mark was made on each end of the steel tubes, 130 mm in from the ends. The specimen was put into the testing machine and gripped by the jaws, ensuring that the full 130 mm jaw length was engaged (using the marks as a visual guide).

An extensometer of 50mm gauge length was used for all tests (figure 3-6). This was placed on the GFRP bar in the upper portion (not covered by the safety shield). The pin was removed prior to testing.

Loading began until the bar was loaded to ~30% of the predicted ultimate load. At this point the extensometer was removed and the upper tube of the safety shield was raised and fastened to the upper steel gripper. The testing continued until failure of the bar.

Records of load (kN), displacement (mm) and strain were recorded by a computer to use in the evaluation of results. (See Appendix A.)

3.3 Results

During testing, and once the extensometer had been removed, the bar was completely covered by the aluminium safety shield so was therefore not visible at the point of failure.

In some of the preliminary tests, pull out failure occurred instead of the ideal failure where the bar would rupture into many long strands of fibre glass. The two types of failure (figure 3-7) could be clearly identified by the noises made by the bar breaking. In some instances the sample failed due to (approximately 20mm) pull out of the bar from the epoxy, sometimes with small parts of the bar delaminating from the rest of the sample. This gave a single, very loud bang. In most cases (all of the cases presented in this here) the bar failed by rupturing into many fine stands of fibre glass (a perfect failure) and this was identified by a series of loud pops and cracks as the individual strands broke. Figure 3-8 shows a failed GFRP bar sample alongside one that had yet to be tested.

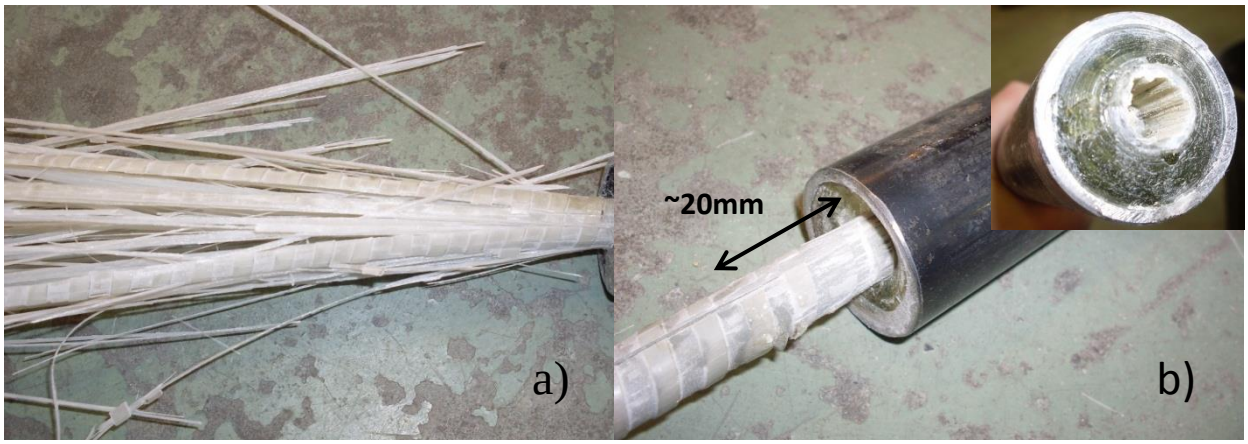

Figure 3-7: Close up photographs showing the two different failure types observed: a) Fracture of bar over entire length. All tests presented in this chapter failed in this manner. b) Pull out failure in epoxy (Inset: view from end of steel tube, clearly showing cavity where bar has pulled out).

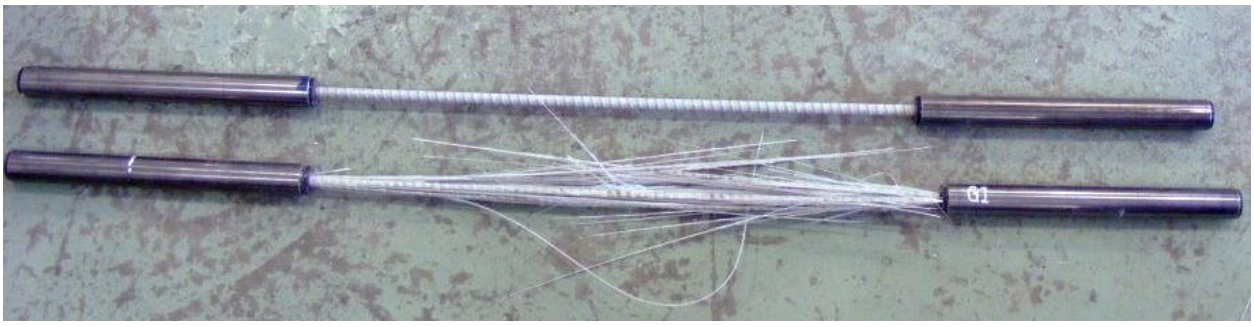

Figure 3-8: Comparison of 'ready to test' specimen with specimen after testing.

Figure 3-9 shows a plot of the load-displacement data in the initial stages of testing (while the extensometer was still attached to the bar). Further graphs and more detailed results are presented for each test in Appendix A. Tables 3-4 to 3-7 below present a summary of the results for UTS and E modulus for each bar diameter. Error in the use of the extensometer led to incorrect strain values for the first two tests

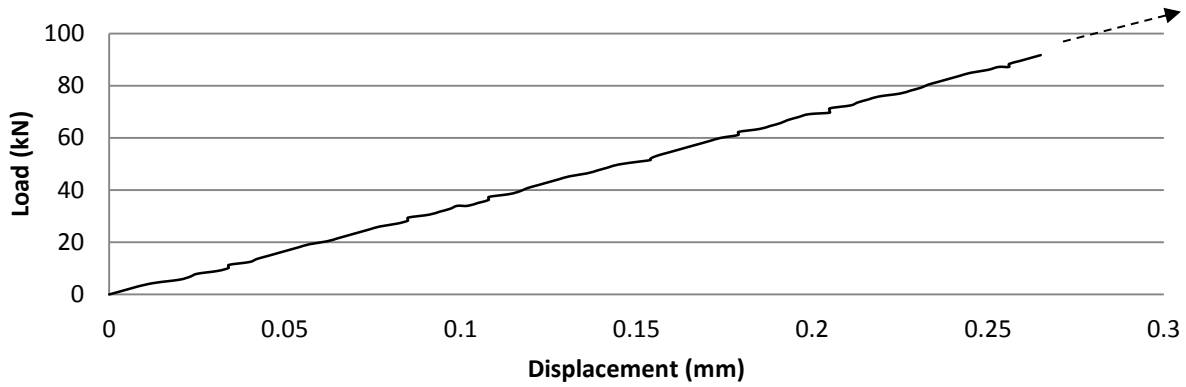

Figure 3-9: Load vs displacement graph for a tensile test on a 22mm sample of Mateen-bar. The behaviour is clearly elastic. Note: The test continued beyond this load range until failure, but the extensometer used to record the displacement was removed for safety reasons.

of the 16 mm bar and the 9th test of the 22 mm bar, so no E modulus values were calculated for these tests. The total sample size for the 16mm bar tests is smaller than ten, due to two of the bars being 'wasted' when trying an epoxy product instead of grout for attaching steel grippers to the ends in two preliminary tests of the bar setup (which produced an incorrect pull-out failure).

Table 3-4: Summary of results for 10 mm Mateen-bar tensile tests.

10 mm	Date: 19/12/2013										Load rate: 0.08x200kN per minute = 16 kN/min		
Sample No.	1	2	3	4	5	6	7	8	9	10	**Mean**	**Std. Dev.**	**COV (%)**
UTS (MPa)	915	906	974	966	923	949	872	983	983	923	939	37	4.0
E modulus (GPa)	57.6	59.7	61.4	61.4	65.3	62.2	57.2	57.6	56.4	57.9	59.7	2.8	4.7

Table 3-5: Summary of results for 12 mm Mateen-bar tensile tests.

12 mm	Date: 18/12/2013										Load rate: 0.08x200kN per minute = 16 kN/min		
Sample No.	1	2	3	4	5	6	7	8	9	10	**Mean**	**Std. Dev.**	**COV (%)**
UTS (MPa)	882	888	865	865	854	871	865	888	882	894	875	13	1.5
E modulus (GPa)	50.2	54.4	52.4	52.3	53.1	53.8	52.8	53.2	52.6	54.3	53.0	1.2	2.3

Table 3-6: Summary of results for 16 mm Mateen-bar tensile tests.

16 mm	Date: 17/7/2013										Load rate: 0.03x500kN per minute = 15 kN/min		
Sample No.	1	2	3	4	5	6	7	8	-	-	**Mean**	**Std. Dev.**	**COV (%)**
UTS (MPa)	852	867	864	905	874	902	874	902			880	20	2.3
E modulus (GPa)	-	-	47.5	51	51.8	50	51.8	51.6			50.6	1.4	2.8

Table 3-7: Summary of results for 22 mm Mateen-bar tensile tests.

22 mm	Date: 18/7/2013										Load rate: 0.03x500kN per minute = 15 kN/min		
Sample No.	1	2	3	4	5	6	7	8	9	10	**Mean**	**Std. Dev.**	**COV (%)**
UTS (MPa)	890	901	895	885	890	879	903	880	925	885	893	16	1.8
E modulus (GPa)	50.6	51.5	50.1	48.4	49.6	50	52.9	51.7	-	49.6	50.5	1.7	3.3

Tables 3-8 and 3-9 show a comparison of the calculated values of guaranteed tensile strength and specific tensile modulus with those given in the Key Specifications of Mateen-bar, issued March 2012 by Pultron. The guaranteed tensile strength values were calculated as the mean UTS value minus three standard deviations. Figure 3-10 shows the Gaussian distribution for the 22 mm nominal bar size, including the guaranteed tensile strength value shown at the lower end of the probability density function.

Table 3-8: Comparison of experimental and manufacturer's guaranteed tensile strength.

	UTS (MPa)	Guaranteed tensile strength (MPa)	
Bar size (mm)	**Mean**	**Experimental**	**Pultron**
10	**939**	827	750
12	**875**	836	750
16	**880**	819	690
22	**893**	845	690

Table 3-9: Comparison of experimental and manufacturer's specified tensile modulus.

	Specified tensile modulus (GPa)	
Bar size (mm)	**Experimental**	**Pultron**
10	60	53
12	53	53
16	51	51
22	50	51

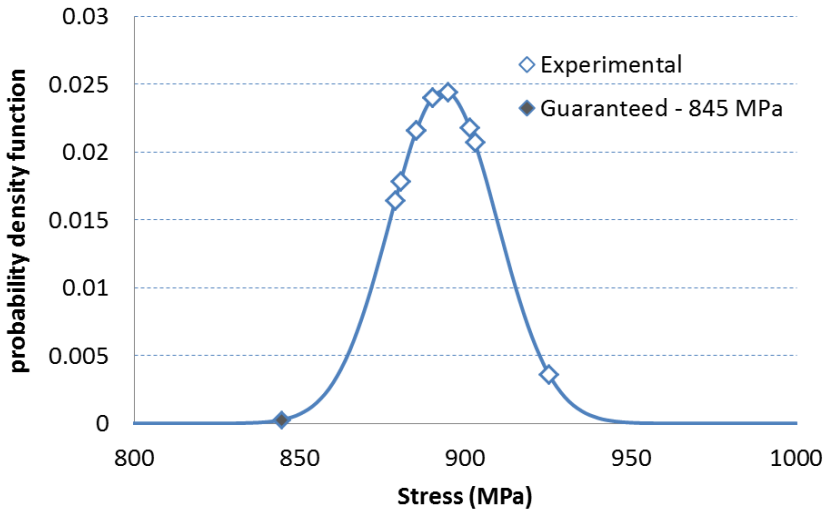

Figure 3-10: Gaussian distribution of tensile strength for the 22mm bars. The guaranteed tensile strength value (μ-3σ) as calculated from the experimental values is also shown.

3.4 Discussion

In all tests splitting failure occurred along the length of the bars. Failure did not occur in the grouted anchorage.

The Ultimate Tensile Strength (UTS) was calculated for each test from the ultimate load reached during testing, divided by the root area of the bar. The guaranteed values calculated from these tests did not seem to show a trend of increasing with a decrease in bar diameter, as implied by the guaranteed strength values given. All experimental values (Table 11) were within 3% of each other.

The maximum coefficient of variation for the UTS values calculated is 4.0% for the 10 mm bar tests, with the other three values between 1.5 and 2.3%, showing that the spread of data is very close in general, but was significantly more spread out for the 10 mm bar tests.

The Elastic Modulus (E) was calculated from strain values taken at the beginning of the test, while the extensometer was still gripped onto the bar. Calculations were generally done using the strain values between 0.001 and 0.003 as suggested in the ASTM standard, or as close as possible to reduce the chance of the values being affected by initial movements of the sample. To check if the selected values were appropriate to use, they were checked against a plot of stress vs strain to confirm they came from a stretch of data that was clearly linear. The average tensile modulus was found to increase as the bar diameter decreased. The calculated values for specified tensile modulus matched or were higher than those given by Pultron for the 10, 12 and 16 mm diameter bar tests. The value for the E modulus for the 22 mm bar was slightly lower than the given values but only by 2%. As this is an average value this is assumed to be an acceptable validation of the modulus values given in the Mateen-bar Key specification (See Appendix C).

The maximum coefficient of variation for the calculated E modulus is 4.7% for the 10 mm test, with the other three values between 2.3 and 3.3%. This confirms that the 10 mm test had a larger variance in data for both variables.

The variability in the 10 mm bar tests is thought unlikely to be due to the specimen preparation, as both the 10 mm and 12 mm specimens (which displayed ideal results) were prepared simultaneously and to the same method. The testing was carried out on separate days, though only one day apart and with care as to use the same testing method.

Comparison with other product specifications in table 13 shows that Mateen-bar is currently taking a more conservative approach in specifying strengths by grouping similar bar sizes to reduce the complexity of the specification tables. Note that while the bars tested here were 12mm nominal diameter, the other products do a standard size of 13mm. Pultron also manufacture a bar in this size and the guaranteed tensile strength is still the same at 750MPa so the comparison in the table is valid. Mateen-bar strength values are quite comparable with C-BAR and Aslan-100 products, while the strengths specified for V-ROD are approximately 50% higher than any of the other bar products shown. In the rightmost two columns are values for the second generation (GII) Mateen-bar product for which data values were released at the time of writing (A 12mm and 22mm bar size had not yet been released in the GII series). Other bar sizes had not yet been released (See Appendix D for most recent Mateen-bar specification). It can be seen that the tensile strength values of these bars are considerably higher than the first generation product and are more comparable to V-ROD strengths. The tensile modulus however is much greater than any of the other bar products. All bar products included in table 13 are manufactured using the Pultrusion process as described briefly in 3.1.

Table 3-10: Comparison of Mateen-bar product specifications with other GFRP reinforcing bars. GTS stands for Guaranteed Tensile Strength, and E is Elastic modulus (Tensile).

Product Name:	C-BAR		Aslan 100		V-ROD standard		Mateen-bar		Mateen-bar GII	
Manufacturer:	Marshall Composite Systems, LLC.		Hughes Brothers, Inc.		Pultrall, Inc.		Pultron Composites Ltd.		Pultron Composites Ltd.	
Bar size, diam.	GTS (MPa)	E (GPa)	GTS (MPa)	E (GPa)	GTS (MPa)	E (GPa)	GTS (MPa)	E (GPa)	GTS (MPa)	E (GPa)
#3, 10mm	780	42	827	46	1100	52.5	750	53	1240	60
#4, 13mm	725	42	758	46	1140	52.5	750	53	-	-
#5, 16mm	655	40	724	46	1130	52.5	690	51	1045	58
#7, 22mm	630	40	655	46	1100	52.5	690	51	-	-

3.5 Conclusions

The GFRP reinforcing bar product Mateen-bar, manufactured by Pultron Composites Ltd., was tested in the University of Canterbury Civil Structures Laboratory to determine the ultimate tensile strength and tensile modulus.

The difficulty of testing GFRP bars in tension without localized crushing of the bar was overcome by using grouted steel grippers to distribute the gripping force along the bar. Safety issues were also mitigated by the use of an aluminium bar cover and appropriate personal protective gear.

The experimental and specified values for the tensile modulus were in good agreement. The ultimate tensile strength results were found to be higher than the guaranteed values given by Pultron's Mateen-bar product specification for the 12, 16 and 22 mm diameter bar tests. Based on these results, this means that any design using the current specified guaranteed strength values would be acceptable for structural applications of Mateen-bar.

Discrepancies in the experimental results are to be expected for GFRP tensile tests due to complexities introduced by the end gripping system. Though the experimental tensile strength values exceeded the design values given by Pultron, there were some clear discrepancies in the trends of calculated guaranteed strength values with those given in the specifications. The test series for 10 mm bars showed more variability than the other bar diameter tests.

This trend of decreasing strength for increasing bar size was not seen in the experimental results, however with further testing across a broader range of sizes this trend may have been observed.

Recommendations for any further testing by the University of Canterbury (or other organization) would be to prepare and test groups of specimens, so that each group contained a set of each different bar diameter. Each group would be prepared over the same two day period and tested (following an

appropriate curing time) all on the same day. This would eliminate any variation due to grout differences between each bar diameter test series, and any changes to test conditions over time.

Mateen-bar currently has similar values to other pultruded GFRP bar products on the market, though the manufacturers may look to make their specified strengths less conservative with the results from further tests in order to be seen as a more competitive alternative to other products.

4 Experimental Slab Testing: Motivation and Design

4.1 Motivation

Bridges are critical to New Zealand's state highway network and the transportation industry. Due to the harsh coastal environments that many New Zealand bridges are located in, there is potential for corrosion of steel reinforcement leading to loss of capacity and high maintenance and repair costs. The bridge deck is directly subjected to moving vehicle loads and is therefore most vulnerable to deterioration and fatigue. GFRP bars are being considered a viable alternative to steel reinforcement for bridge decks in places such as Canada, where there is heavy use of deicing salts.

There are currently no New Zealand studies on the feasibility for GFRP bars to be used as bridge deck reinforcement. Chapters 5 and 6 describe experimental tests of GFRP and steel reinforced concrete slabs, representing a section of a bridge deck. The rest of chapter 4 describes the specimen design for the two phases of slab testing; bending and punching shear tests of GFRP and steel reinforced slabs. Both test phases used identical specimens (except for reinforcement type and ratio).

The objectives of these experiments are:

1. To understand the flexural and punching shear behavior of a bridge deck slab reinforced with deformed GFRP reinforcing bars.
2. To verify existing GFRP reinforced concrete design recommendations and make any additional recommendations appropriate to New Zealand bridge deck design based on the results found.

4.2 Design of experimental specimens

Twelve isolated, full scale 'bridge deck slab section' specimens were manufactured and tested. Six of the slabs were reinforced with GFRP bars, and the other six with steel bars as used in a typical New Zealand bridge deck design. The six GFRP reinforced slabs were identical in design, as were the six steel reinforced slabs. The main variable was the slab reinforcement material and therefore reinforcement ratio, due to the differing strength characteristics between GFRP and steel.

4.2.1 *Materials*

GFRP bars

The GFRP bar product used in these experiments was Mateen-bar, manufactured and supplied by Pultron Composites Ltd. Refer to sections 2.1 and 3 for details of the bar properties and Appendix C for full product specifications. Limited experimental research has been done on the use of this product as reinforcement for concrete members. Some simple beam tests have been carried out, but no laboratory testing of slabs reinforced with Mateen-bar are known to the author.

Steel

The supplied steel was Grade 500 deformed bars, with seismic ductility (D500E12 and D500E20). The two diameters were taken directly from the standard bridge design used (as detailed in 4.2.2).

No additional investigation into or testing of the properties of the steel was done, as these are already well understood.

Concrete

Ordinary concrete was prepared to the target compressive strength of 40 MPa. The compressive strength was 48 MPa after curing for 28 days and 57 MPa at the time of testing (overall averages for three batches of concrete).

4.2.2 *Specimen Description*

The slab design was based on a standard I-beam bridge design taken from Research Report 364 (NZTA, 2008). This document by NZTA is a collection of standard precast concrete bridge beam designs for use in typical bridge superstructure design in New Zealand. The purpose of the document is for NZTA to save costs on similar bridge designs by utilizing these standard profiles. New Zealand bridge design practice is currently a cast in place substructure with a precast decking system (NZTA, 2008). The decking systems consist of single and double hollow core sections, super T and I sections. Only the Super T and I beam sections require a cast in place slab separate from the beams. The slab design for the experimental part of this project will be based on the slab for an I-beam bridge. This typology was chosen the slab for the I-

beam bridge has a much longer 'free' span length between supports (I-beams or Super T flanges) than the Super T bridge configuration.

All experimental slabs were designed based on NZTA Research Report 364 to the dimensions of an I-beam bridge spanning up to 20 m. Figure 4-1 shows the cross section of the bridge. The quantity and layout of the steel reinforcement was taken directly from this design. The GFRP reinforced bridge deck was design to have the same dimensions and a similar dependable moment capacity as the steel reinforced deck design. It is important to note that the GFRP design requires considerable over-design. The two slab design cross-sections are shown in figure 4-2. It can immediately be seen that the GFRP reinforced section has a much greater reinforcement ratio than the steel reinforced section. The manufacturer currently recommends a stress limit of 20% of the UTS be used in design. Due to the limited knowledge of GFRP reinforced concrete behavior at the design phase of this project, it was elected to use the limiting value of 20% UTS with no extra regard for loading type (dead or live load) or load duration. This resulted in large redundancy in the design, which is evident in the experimental results.

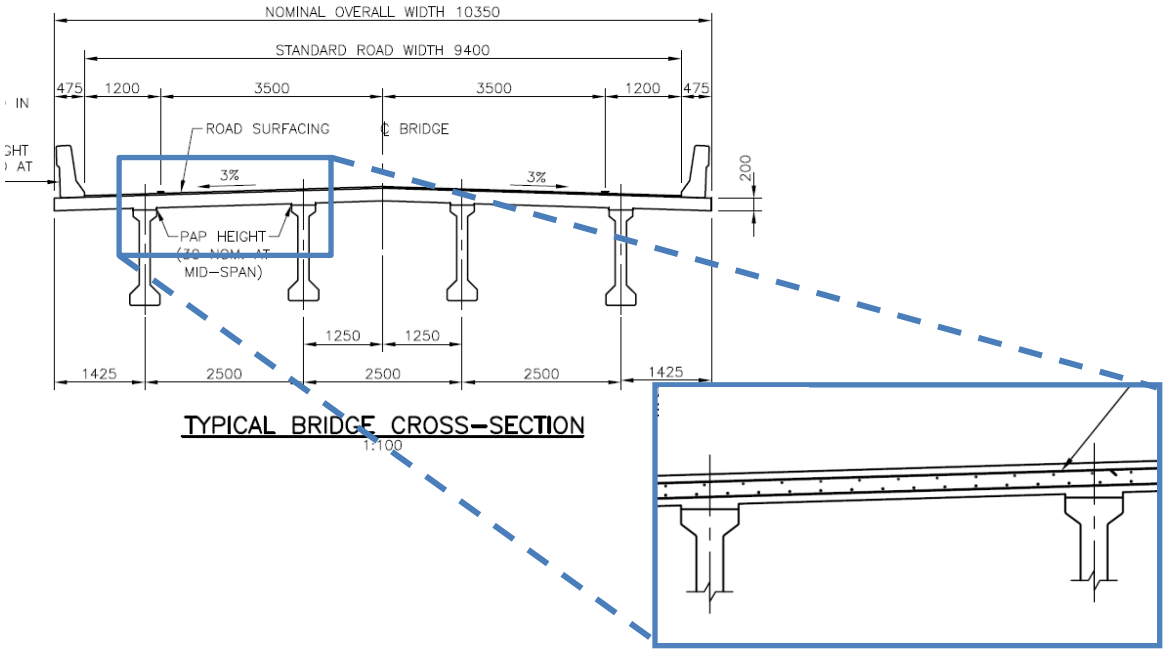

Figure 4-1: CONCEPT: Take existing design of steel reinforced bridge deck from NZTA Research Report 364, and modify with GFRP reinforcement. Cross-section of I beam bridge typology (NZTA, 2008); Close-up of cross- section showing position of longitudinal and transverse deck reinforcement.

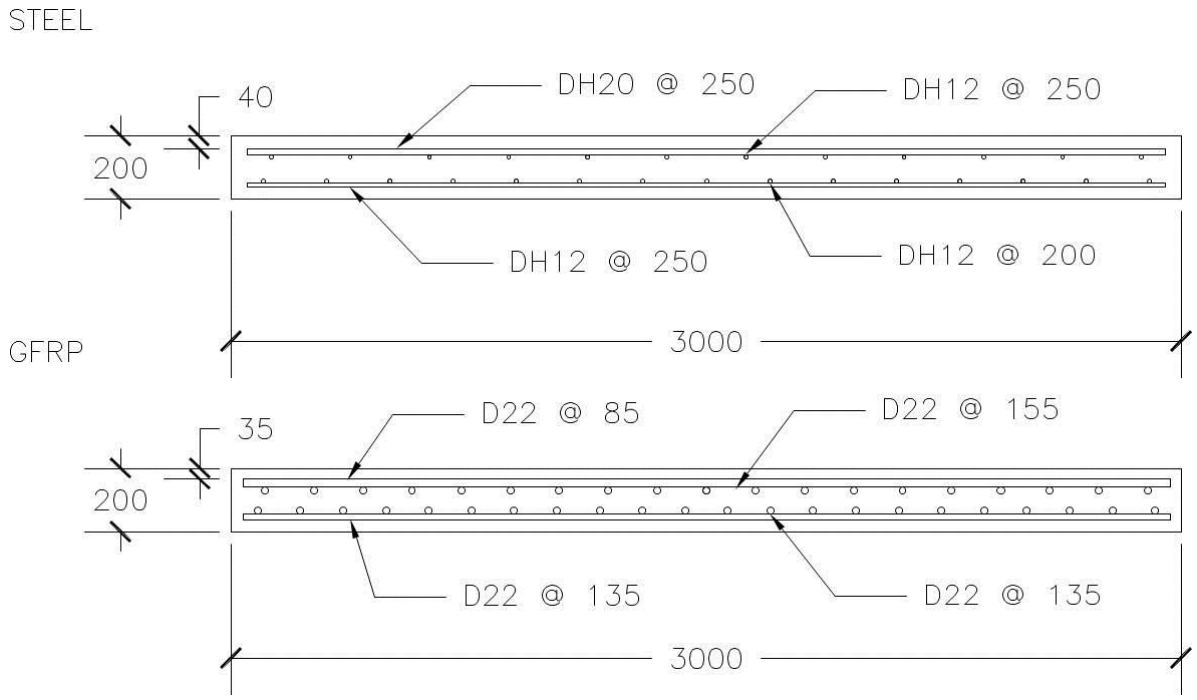

Figure 4-2: Transverse (main direction) cross-sections of steel and GFRP reinforced sections.

Each slab was 3000 x 2600 mm, and 200 mm deep. The individual specimens were coded for identification: S-1 to S-6 for the six identical steel slabs and G-1 to G-6 for the six identical GFRP slabs. The slabs were all reinforced with main (longitudinal) and secondary (transverse) reinforcement at the top and bottom of the slabs. The reinforcement geometry is shown in Table 4-1.

Table 4-1: Slab reinforcement layout.

Reinforcement type	**Bottom Reinforcement**		**Top Reinforcement**	
	Longitudinal	**Transverse**	**Longitudinal**	**Transverse**
GFRP	22 mm @ 135 (ρ = 1.9%)	22 mm @ 135	22 mm @ 85	22 mm @ 155
Steel	12 mm @ 250 (ρ = 0.3%)	12 mm @ 200	20 mm @ 250	12 mm @ 250

Designing the GFRP slab in this way is unlikely to yield the most efficient design, however direct comparability was desired in the tests. Chapter 7 will address recommendations for bridge deck design using GFRP reinforcement.

The ends of the steel bars were hooked to help prevent anchorage failure, however it was impractical to used hooked GFRP bars so straight bars were used. (Hooked bars would need to be formed at the time of

manufacture, and the appropriate bend radius for the bar diameter would not have been well accommodated in the slab depth). The specified cover for the steel reinforced section of 50 mm was unable to be achieved in the manufacturing process, so a reduced cover of 40 mm has used in the updated design drawings.

It should be noted that a tensile strength of 1000 MPa was assumed in preliminary test specimen design calculations for the GFRP bars at the time of design as the tensile properties had not yet been accurately determined in laboratory tests, nor had a more recent version of Pultron's Mateen-bar technical submittal been released. The final design is analysed in depth in the following chapters considering the product data values given in Appendix C.

Figure 4-3: Left) Strain gauge attached to side of steel bar, with waterproof wax coating over top. Another waterproof membrane was added, before wrapping in electrical tape for further protection during the concrete pouring. Right) All strain gauge leads exiting through a PVC pipe offcut and bundled out of the way and to keep them safe during pouring and transportation.

During construction each slab was instrumented with strain gauges in specific locations to measure changes in strain in the bars during testing. Reasonable effort was made to ensure that the location of the strain gauges was comparable between the steel and GFRP reinforced specimens, however a different bar layout meant that the strain gauge readings are not directly comparable in some locations. This was considered where necessary during analysis of results. Figure 4-3 shows a strain gauge attached to a steel bar and the leads taped and bundled securely prior to the concrete pour.

All twelve specimens were fabricated at a precast concrete manufacturing company.

The following two chapters describe the flexural and punching shear testing procedures carried out on these slabs.

5 Experimental Slab Testing: Flexure

5.1 Introduction

This chapter details the findings of experimental flexural testing on six full-scale slab specimens as described in Chapter 4. The particular specimens tested were S-1, S-2, S-3 and G-1, G-2, G-3. The behavior of a GFRP reinforced slab was compared with a steel reinforced slab and three repetitions were carried out for each slab type.

5.2 Experimental Programme

5.2.1 *Test set-up*

Testing occurred using the frame set-up shown in figures 5-1 and 5-2. All slabs were tested in the same manner, over a clear span of 2500 mm. The distance between the two load beams was 800 mm, giving a shear span of 850 mm. The force was applied through a hydraulic actuator controlled by a computer. A single 1000kN load cell was used to measure load applied to the specimens during testing. The load was applied downwards using a hydraulic jack, and the load was either spread evenly to the two load beams. Simple supports were provided by cylindrical metal bars sitting between metal plates supported by three adjustable height supports on each side.

5.2.2 *Instrumentation*

The layout of the strain gauges is shown in figure 5-3. In addition, linear displacement potentiometers were attached to the surface of the concrete slab to monitor the compressive strain in the concrete. Spring loaded linear displacement potentiometers were used to monitor the vertical displacements of the specimen at certain points.

The potentiometers were placed symmetrically to allow an average measurement to be calculated and with some redundancy in case an instrument did not work properly in the testing. Figures 5-4 and 5-5 show the position of the potentiometers.

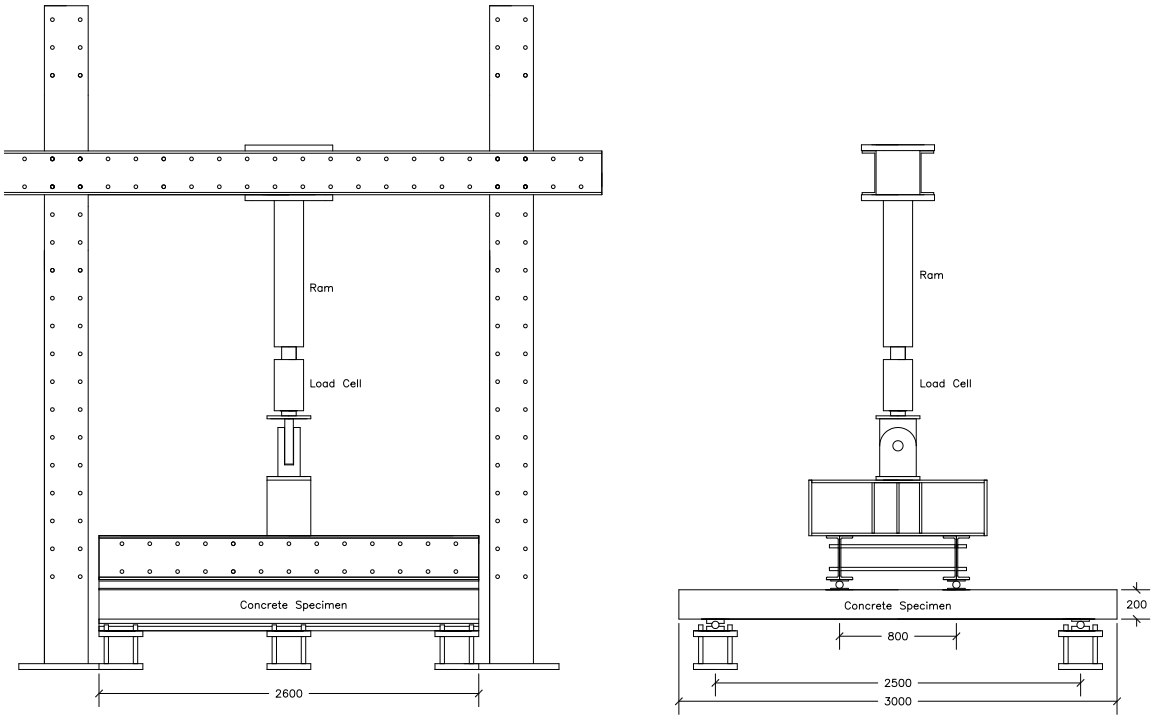

Figure 5-1: Drawing of test set-up. Left: Load frame and supports for flexural test. Right: Four 'point' bending set up (outer frame excluded). All dimensions are in mm.

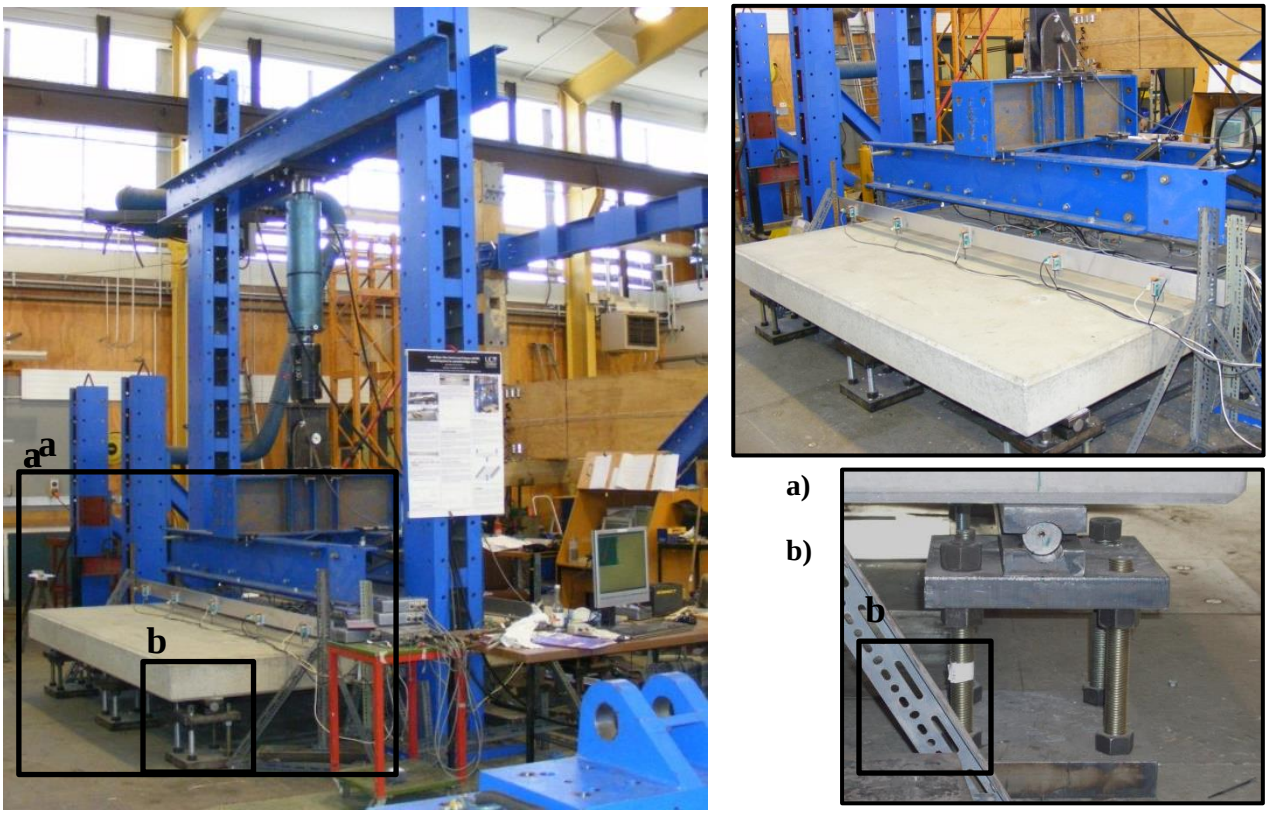

Figure 5-2: Left: Overall photo of bending test set-up. Right: a) Slab specimen with surrounding load frame and instrumentation. b) Close up photo of single support with pinned joint.

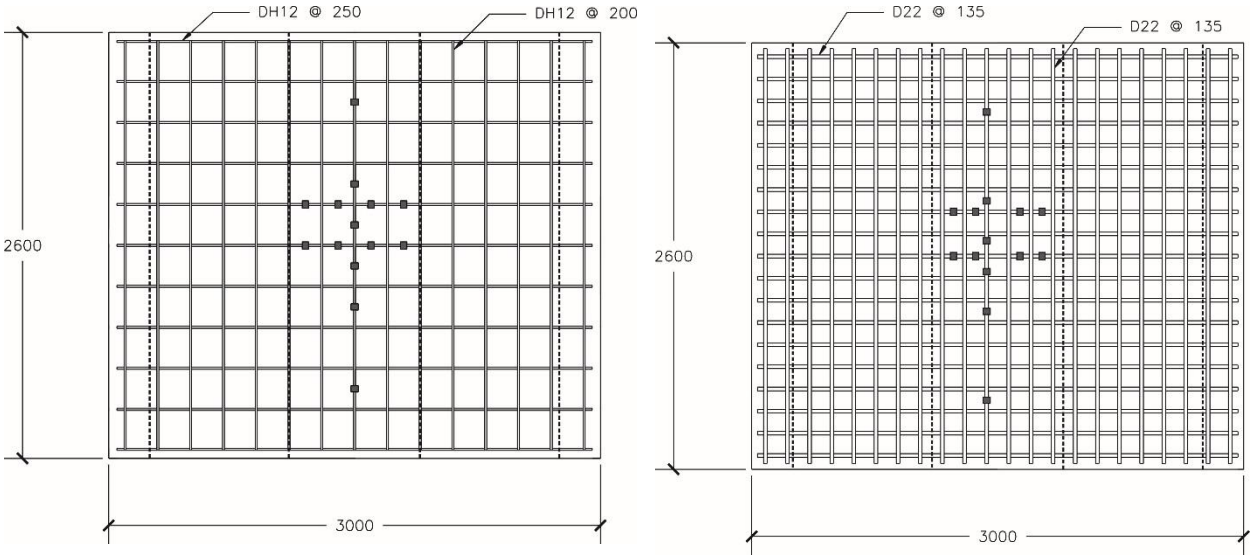

Figure 5-3: Strain gauge layout for steel (left) and GFRP (right) reinforced slab. Note: Only bottom bars shown. Dotted lines show position of load (inner) and supports (outer).

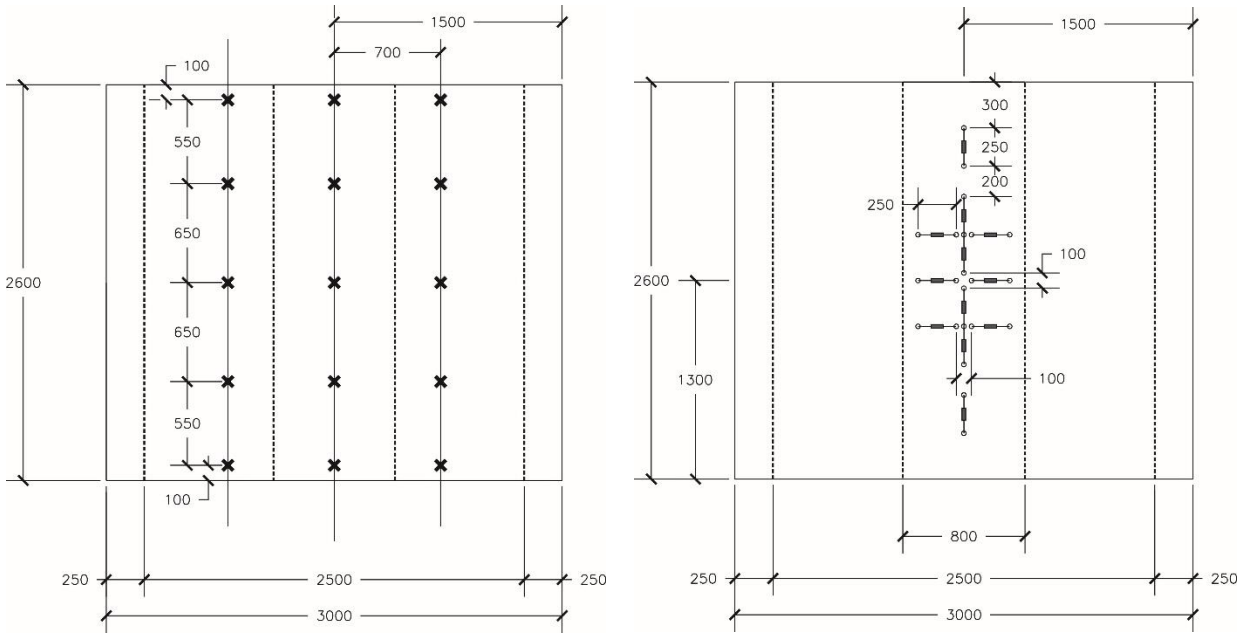

Figure 5-4: Left) Spring potentiometer position (crosses) on slab surface. Dotted lines show position of load (inner) and supports (outer). Right) Symmetrical surface rod potentiometer position on slab surface. The gauge length for each potentiometer was 250 mm.

Figure 5-5: Left) Linear potentiometers and Spring potentiometers set up between the loading beams before testing (prior to leads being attached).

5.2.3 *Loading Protocol*

The loading protocol for the test is shown in figure 5-6. Cyclic loading was chosen over monotonic as this more accurately represents the unload-reload nature of live loading on a bridge deck. The specimen was loaded and then unloaded, in 40kN increments for three repetitions, and then the load was increased in further increments until failure. During this time cracking was observed and strain and load vs displacement data monitored.

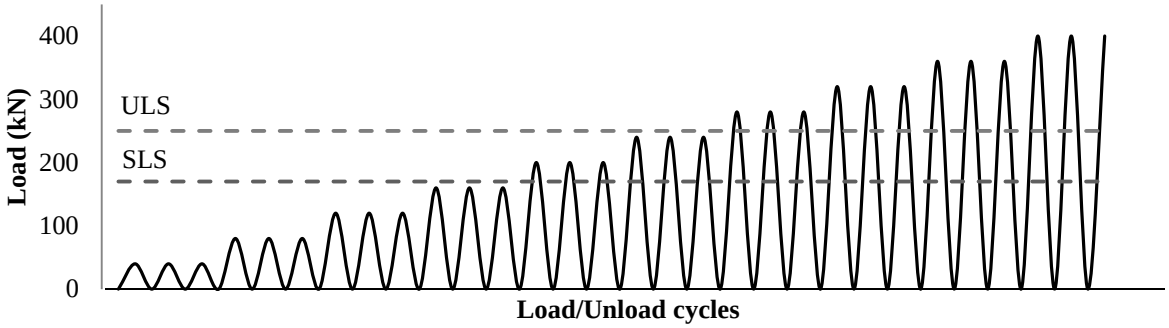

Figure 5-6: Loading protocol for the bending test. Load/unload cycles are repeated three times, then increased in increments of 40 kN. Design values of ultimate limit state (ULS) and serviceability limit state (SLS) are shown.

5.3 Results and Discussion

Applied load (P), deflections at serviceable loads, and strain data for GFRP and steel reinforced slabs were obtained and compared. The applied load is defined as the load (kN) measured by the load cell during testing. Load values corresponding to serviceability limit state (P_{SLS}) and ultimate limit state (P_{ULS}) were calculated based on loads given in the NZTA (2013) bridge manual. P_{SLS} is equal to 170 kN and P_{ULS} is equal to 250 kN. See Appendix B for the calculations and assumptions made.

5.3.1 *Global Behaviour*

Serviceability

Figures 5-7 and 5-8 show the total applied load versus the midspan deflection for the slabs. It is clear from both figures that the results of the three replicate slabs for each reinforcement type were very similar. This indicates that there was good control of materials and specimen manufacture as well as testing procedure. All slabs behaved similarly prior to any cracking. The first change in slope in the load-deflection response curve corresponds to flexural cracking in the specimen. Cracking loads for each slab are given in table 5-1. The cracks formed along the edges of the slab perpendicular to the loading beams, and cracking was typical of a four point bending test; vertical cracks formed first in the centre between the load points and vertical and diagonal cracks formed in the shear spans. Figure 5-9 shows the cracking

patterns at an applied load of 400 kN (not the SLS load, but the figure is useful to see the crack locations). The cracking happens as expected at spacing which reflects the spacing of the transverse reinforcing bars.

Table 5-1: Summary of experimental load data.

Rebar Type	Slab Code	Cracking Load (kN)	Yield Load (kN)	Failure Load (kN)
Steel	S-1	80	250	441
	S-2	78	240	402
	S-3	102	280	437
Average	S-AV	87	260	426
GFRP	G-1	66	na	na (max 441)
	G-2	55	na	na (max 404)
	G-3	56	na	na (max 422)
Average	G-AV	59	-	-

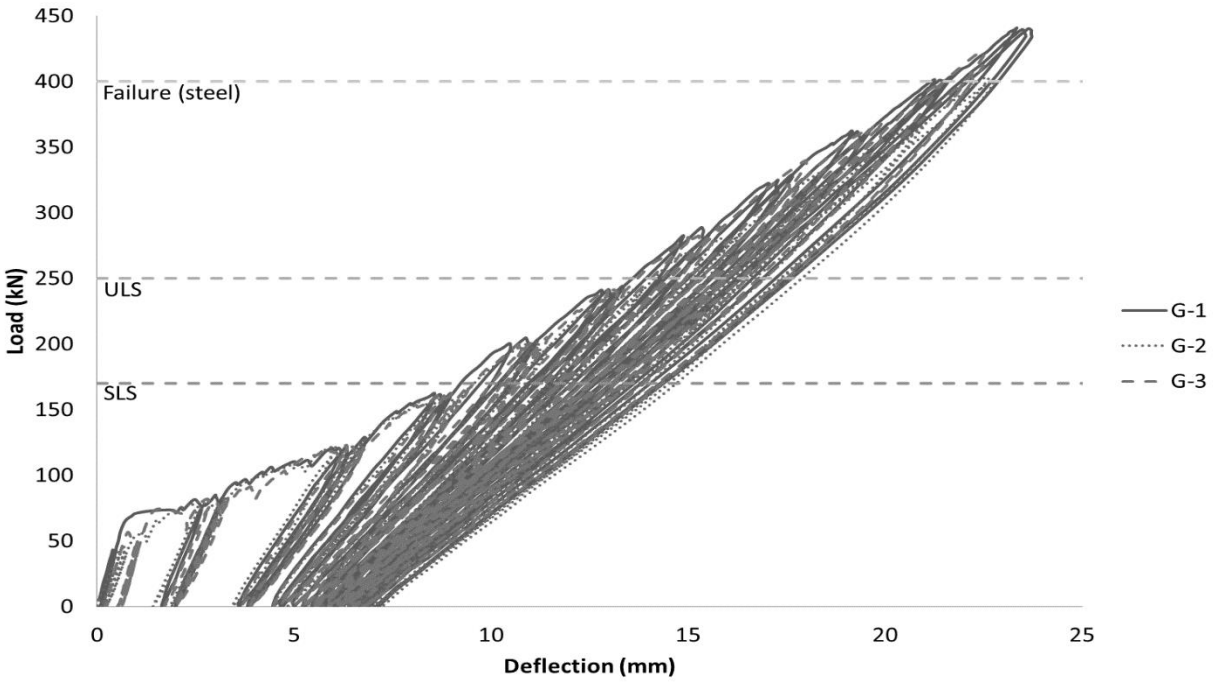

Figure 5-7: Global slab behaviour: Applied load vs midspan deflection of GFRP reinforced slabs.

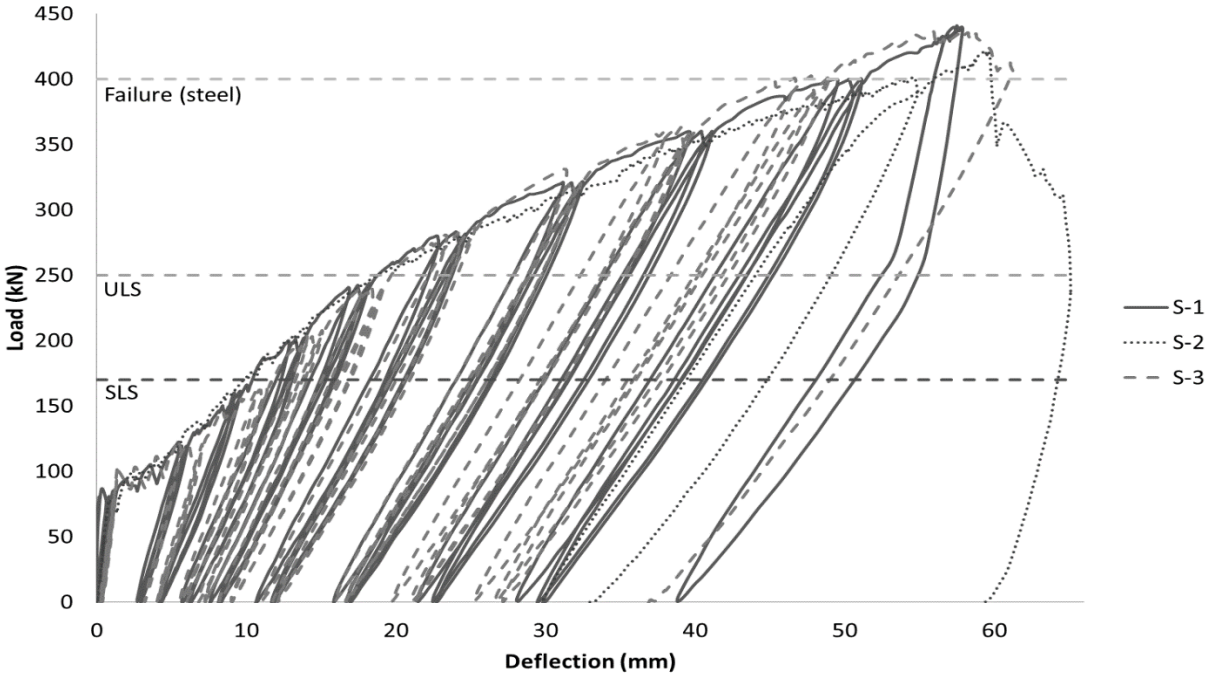

Figure 5-8: Global slab behaviour: Applied load vs midspan deflection of steel reinforced slabs.

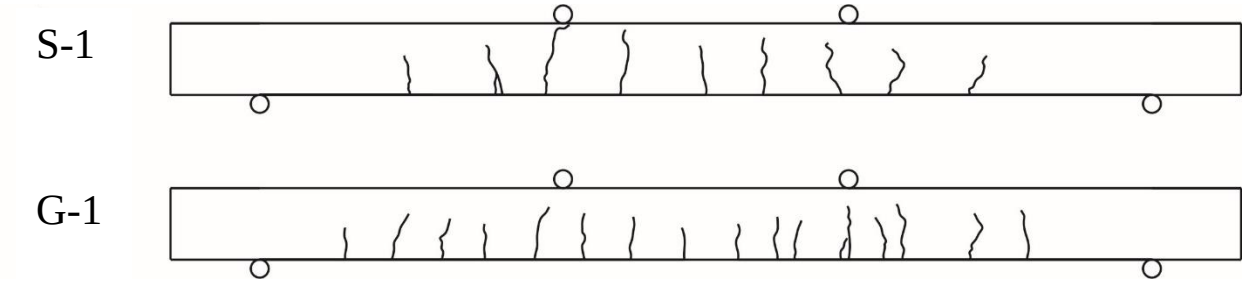

Figure 5-9: Crack patterns along the side of the slab for an applied load, P, of 400 kN. Circles above and below represent load points (inner) and supports (outer).

Figure 5-10 shows in a direct comparison of both slab types that the initial stiffness of the slab prior to any cracking is governed by the gross section properties, as both slab types show a similar initial stiffness. Post crack, the stiffness of each slab type is greatly affected by the reinforcement type and reinforcement ratio. Even though the elastic modulus of GFRP is approximately ¼ that of steel, the post cracking stiffness for the GFRP reinforced slab is much greater than that of the steel reinforced slab. This is due to the much greater reinforcement ratio that the GFRP slab had compared with the steel slab (1.9% for

GFRP vs 0.3% for steel). If the reinforcement ratios were identical, then GFRP reinforced slab would have a much lower post cracking stiffness than the steel reinforced slab due to the lower elastic modulus. The post cracking stiffness of the GFRP slab is also approximately linear, due to the linear stress-strain behavior of the GFRP reinforcing bars. Slab behavior at serviceable levels is not a concern for this GFRP slab design due to the considerable over-design.

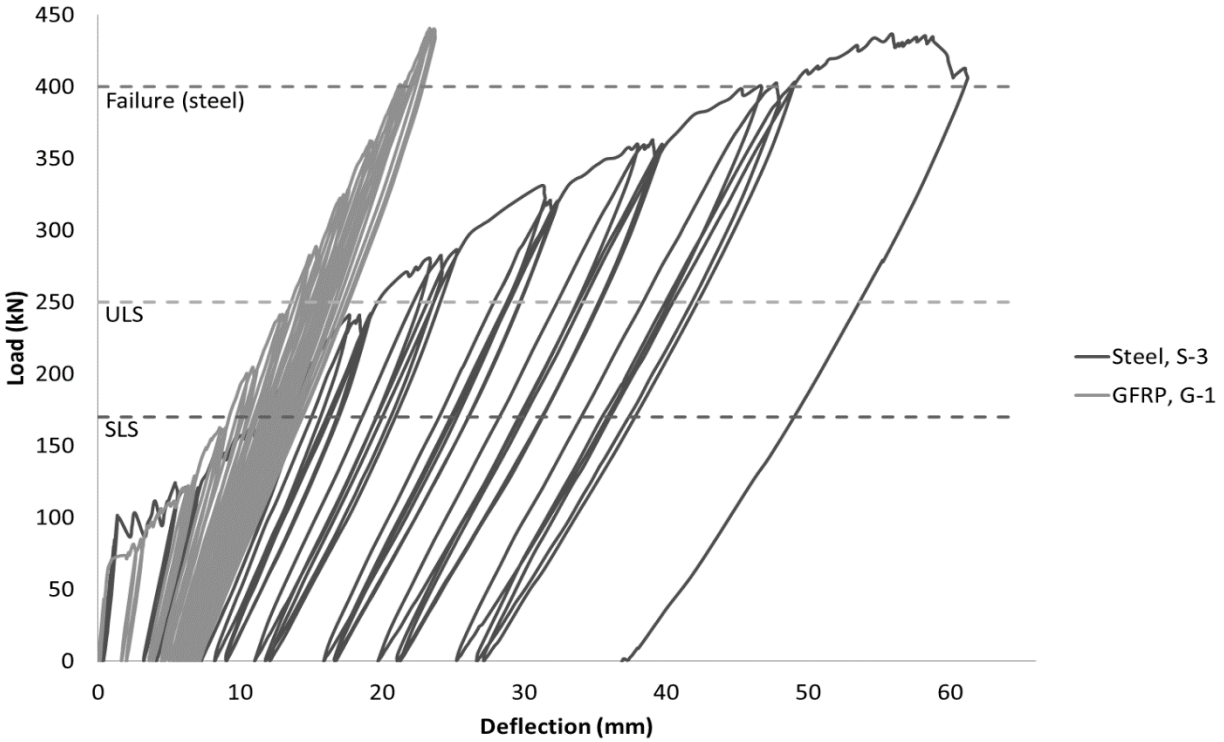

Figure 5-10: Global slab behaviour: Applied load vs midspan deflection comparison between two reinforcement types.

Ultimate

First steel yielding was assumed to occur at the next apparent change in slope of the load-deflection response curve after the cracking point. Assumed yield loads are given in table 5-1.

At ULS the steel slab has approximately 5mm more deflection than the GFRP slab. Similar to the discussion for SLS, this is due to the over-reinforced design of the GFRP slab.

Failure (steel)

All of the steel reinforced slabs were able to be tested to failure, however, due to constraints with available equipment and laboratory strong floor maximum limits the GFRP reinforced slab was unable to

be tested to failure. This slab was therefore tested until the approximate failure load of the steel reinforced slab, to provide a direct comparison up to this loading value of approximately 400 kN. Figures 5-11 and 5-12 show the two slab types loaded to 400 kN.

It is interesting point to note how much more capacity the steel reinforced slab had past the ULS loading level (approximately 60%). This indicates that existing New Zealand bridges may be over-conservative in design, and methods used to assess older bridge stock for remaining service life may be underestimating capacity by a significant margin (e.g. the difference between carrying out a bridge strengthening program or just monitoring). Further research and investigation of the 'true' capacity of existing bridge designs may be worthwhile to confirm this.

A summary of observed deflections is given in table 5-2.

The response of the GFRP reinforced slab is linear after the cracking point as GFRP reinforcement does not yield. The ultimate failure load of the GFRP can be predicted based on the design of the slab and the concrete strain data obtained during the tests. Assuming the stress-strain data would continue to increase linearly as load is increased until failure, the ultimate load was found by extrapolation of the experimental data.

A comparison of the extrapolated failure load for the GFRP slab and the steel reinforced slab is given in table 5-3.

Table 5-2: Summary of experimental deflection data.

Rebar Type	Slab Code	Max Deflection (mm)		
		SLS, P = 170 kN	ULS, P = 250 kN	Failure (steel), P = 400 kN
Steel	S-1	10.9	19.4	48.8
	S-2	9.8	18.8	51.7
	S-3	11.8	20.0	45.6
Average	S-AV	10.8	19.4	48.7
GFRP	G-1	9.9	14.4	21.4
	G-2	9.7	14.5	21.9
	G-3	11.8	14.0	23.5
Average	G-AV	10.5	14.3	22.3

Table 5-3: Extrapolated failure load for GFRP slab compared with experimental failure load.

Rebar type	Ultimate Load (kN)
Steel	426 (experimental)
GFRP	~1200 (extrapolated)

Figure 5-11: Left) Steel slab loaded up to 400 kN. Note that it was difficult to obtain clear photographs during testing due to the necessary frame set-up for loading and displacement data collection. Right) Steel slab at failure (Not the same slab as in left photo). Note the wide crack opening and concrete spalling on top of the section.

Figure 5-12: GFRP slab loaded up to 400 kN.

All slabs were unloaded after testing was complete. The steel reinforced slab (failed) showed significant permanent displacement. The GFRP slab returned to approximately its original form with very little permanent deformation (due to concrete cracking). Figure 5-13 shows one of the GFRP reinforced slabs stacked upon a steel reinforced slab for comparison.

As the GFRP reinforced slabs were not tested to failure the ductility of the system could not be accurately determined using the method by Grace et al. (1998). However it can be seen from the unloading paths on the load – deflection plot that the elastic energy portion of the total energy absorption (up until the test was stopped) is significantly larger than the inelastic portion. Although the final part of the load – deflection curve is unknown, assuming that the energy ratio would remain low (as was seen in other tests of GFRP reinforced slabs to failure) this could be classified as ‘brittle’ ductility (Refer to figure 2-7).

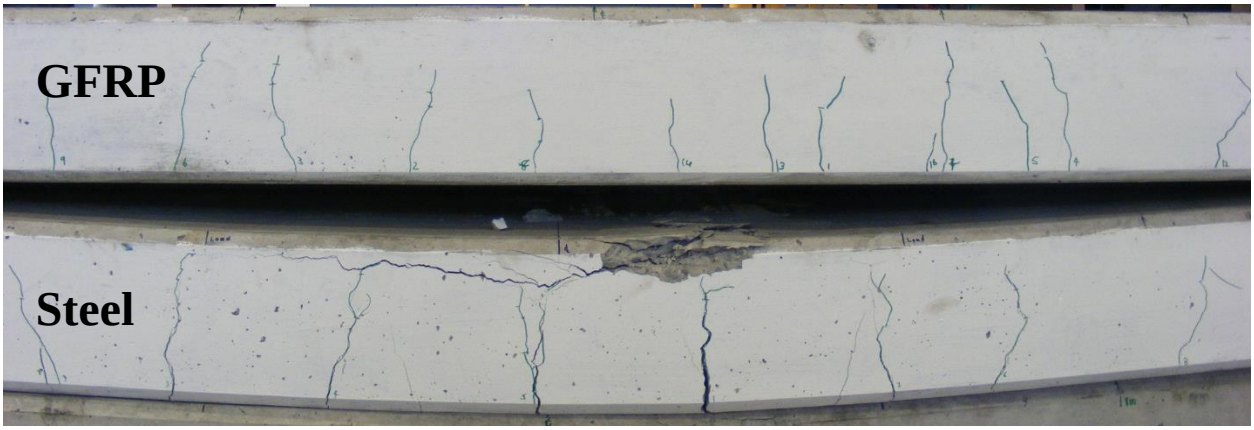

Figure 5-13: Comparison between GFRP and steel reinforced slabs after testing. Note the permanent deflection is much more obvious for the lower steel reinforced slab.

5.3.2 *Local Behaviour*

Serviceability

The following assumptions were made when performing calculations (up to ultimate limit state):

a) Plane sections remain plane until failure

b) Maximum compressive strain ε_{cu} is assumed to be 0.004

c) Concrete tensile strength is ignored

d) GFRP tensile behavior is linear (elastic) until failure

e) A perfect bond exists between the concrete and the reinforcing bars

The stress-strain model proposed by Hognestad in 1951 for unconfined concrete in compression was adopted for simplicity of calculation. The formula for this model is written as:

$$f_c = f_c' \left(\frac{2\varepsilon_c}{\varepsilon_{co}} - \left(\frac{\varepsilon_c}{\varepsilon_{co}} \right)^2 \right) \quad \varepsilon_c \leq \varepsilon_{co} \tag{6}$$

$$f_c = f_c' \left(1 - \beta \left(\frac{\varepsilon_c - \varepsilon_{co}}{\varepsilon_{cu} - \varepsilon_{co}} \right)^2 \right) \quad \varepsilon_{co} < \varepsilon_c \leq \varepsilon_{cu} \tag{7}$$

where f_c and ε_c are the compressive stress and strain in the concrete. f'_c is the cylinder compressive strength of the concrete (f'_c is taken to be 50 MPa for all section analysis calculations), ($\varepsilon_{co} = 0.002$) is the

strain in the concrete at peak stress, β is a degradation factor taken to be 0.15. The stress beyond ε_{cu} is assumed to decreased linearly so that stress is zero at the spalling strain, ε_{sp} = 0.0064.

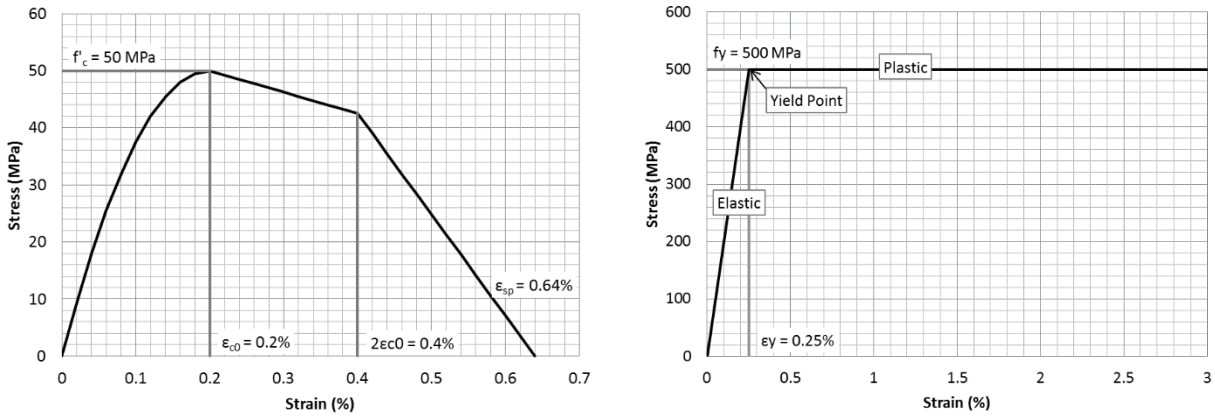

Figure 5-14: Constitutive models used to convert strain data into stress values for concrete (left) and steel (right).

Figure 5-14 shows both the concrete and steel stress-strain curves used in the analysis. The experimental depth of the neutral axis was obtained by geometry after determining average strain values for the concrete compression fibre and the bottom reinforcement. Table 5-4 is a summary of all measured strain values at each significant load value.

Table 5-4: Summary of experimental strain data.

Rebar Type	Slab Code	Max Strain at Service Load, %		Max Strain at Ultimate Load, %		Max Strain at Failure (steel) Load, %	
		Rebar	Concrete	Rebar	Concrete	Rebar	Concrete
Steel	S-1	0.20	-0.07	0.40	-0.12	0.96	-0.31
	S-2	0.19	-0.05	0.40	-0.10	0.77	-0.34
	S-3	0.19	-0.06	0.32	-0.11	0.69	-0.27
Average	S-AV	0.20	-0.06	0.37	-0.11	0.81	-0.30
GFRP	G-1	0.15	-0.05	0.22	0.07	0.35	-0.12
	G-2	0.15	-0.05	0.22	0.08	0.35	-0.13
	G-3	0.13	-0.06	0.19	0.08	0.31	-0.12
Average	G-AV	0.14	-0.05	0.21	0.08	0.33	-0.12

Figure 5-15 shows that the strain levels are fairly similar at P = 170 kN, though GFRP section shows slightly lower levels of strain and a lower neutral axis by ~6.5 mm. Figure 5-16 shows that at serviceable loads, the level of stress in the concrete is fairly similar for both cases, but stress in the GFRP bars is much lower, due to the much lower elastic modulus of GFRP. Theoretical values for the neutral axis assuming post-cracked and linear behaviour for the steel and GFRP reinforced slabs are respectively, 33mm and 26mm. The steel slab has reached the post-cracked behaviour at this stage, whereas the GFRP slab is still shy of this stage as can be seen from its lower (relative to the section depth) neutral axis position.

Due to the significant over-design of the GFRP slab, both slabs showed very similar global behaviour at SLS. The local behavior seen in the stress and strain distribution supports this observation, excepting that at SLS the GFRP are significantly less stressed than the steel bars. This will largely be due to the fact that the volume of GFRP bars is much greater than the steel bars for the two tested slab designs.

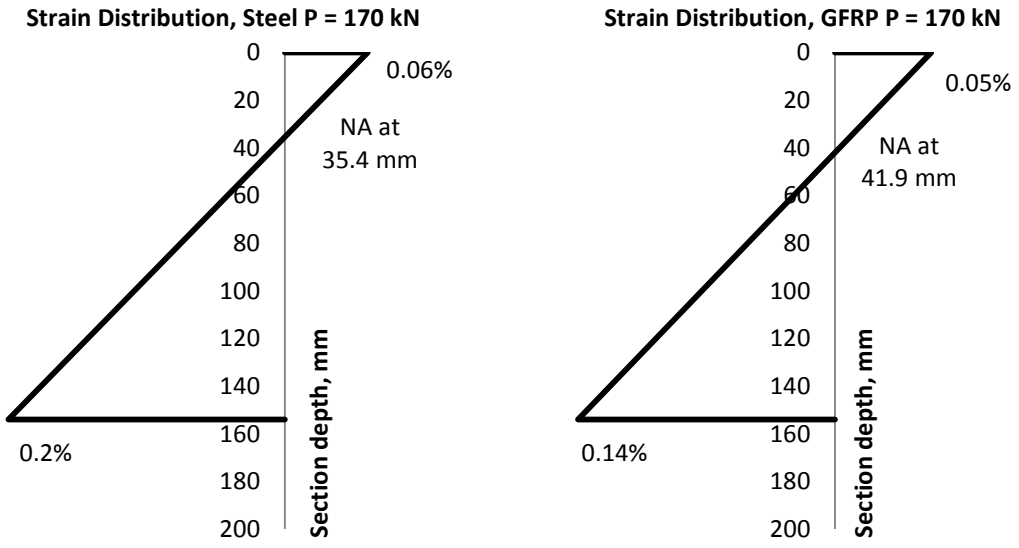

Figure 5-15: Mid-span strain distribution at P = 170 kN for both reinforcement types plotted using experimental strain data.

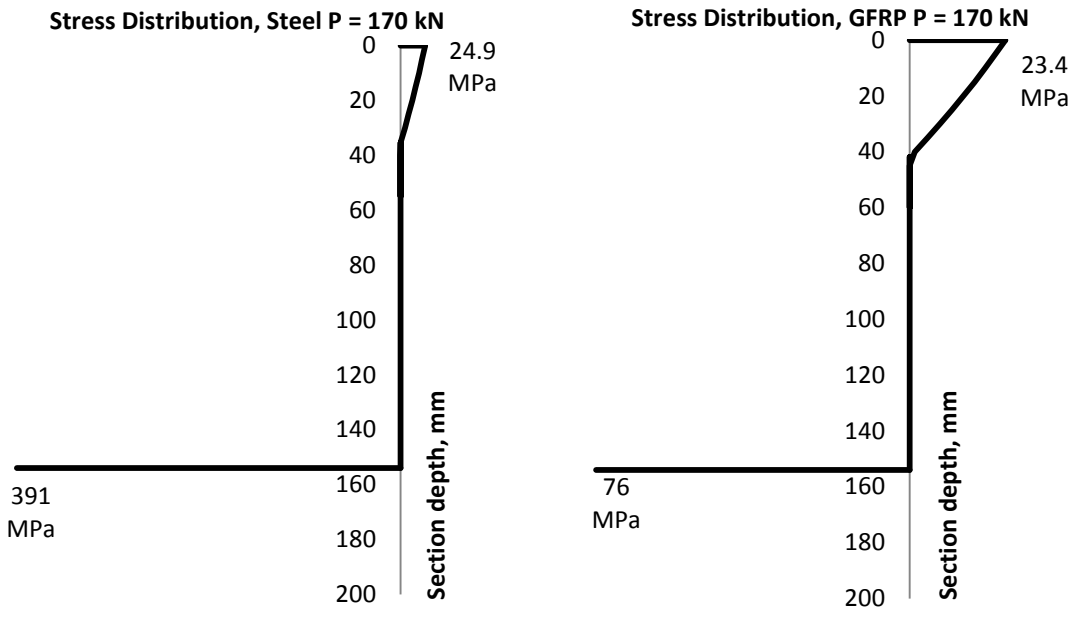

Figure 5-16: Mid-span stress distribution at P = 170 kN for both reinforcement types calculated from the experimental strain data.

Ultimate

Figure 5-17 shows that the strain levels in the steel section at P = 250 kN are greater than those in the GFRP section, and approximately twice as great for the reinforcement.

Figure 5-18 shows that the steel has reached yield point, so will be able to support no further load. The GFRP bars have only reached approximately 14% of their ultimate strength (790 MPa). The concrete stress is approaching (but not yet reaching) its compressive strength of 50 MPa; the steel reinforced section is much closer to reaching this limit than the GFRP section.

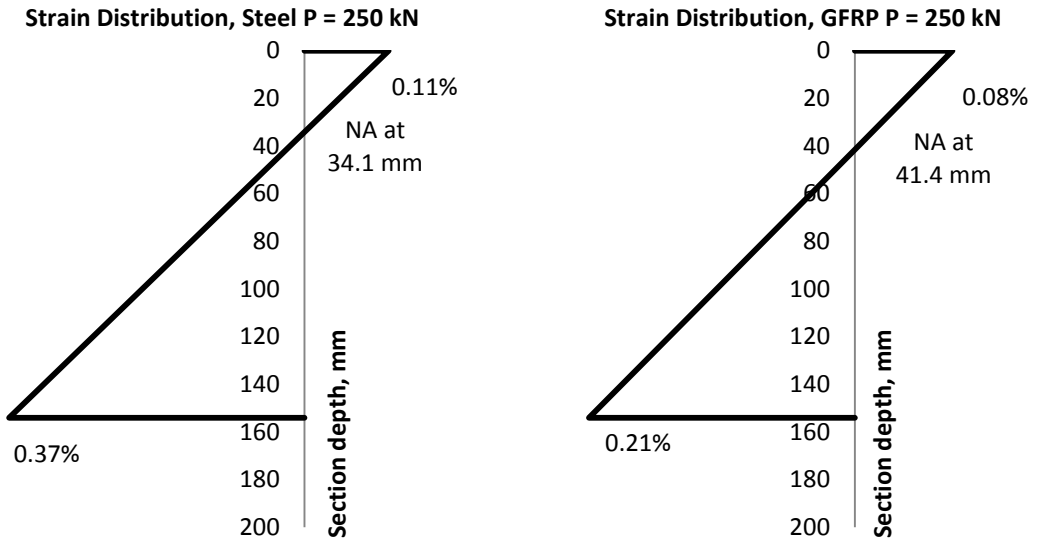

Figure 5-17: Mid-span strain distribution at P = 250 kN for both reinforcement types plotted using experimental strain data.

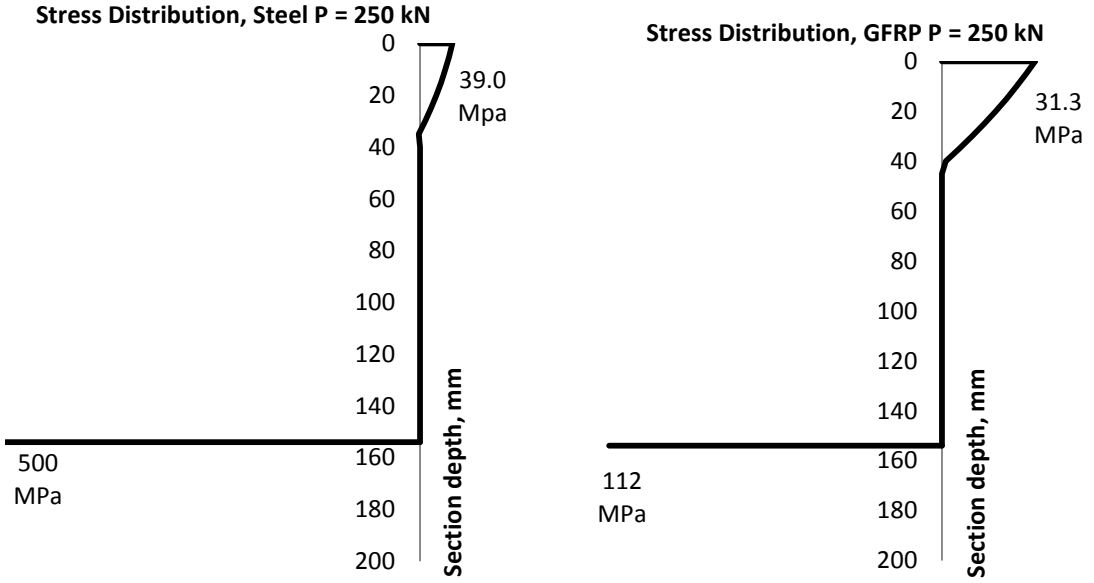

Figure 5-18: Mid-span stress distribution at P = 250 kN for both reinforcement types calculated from the experimental strain data.

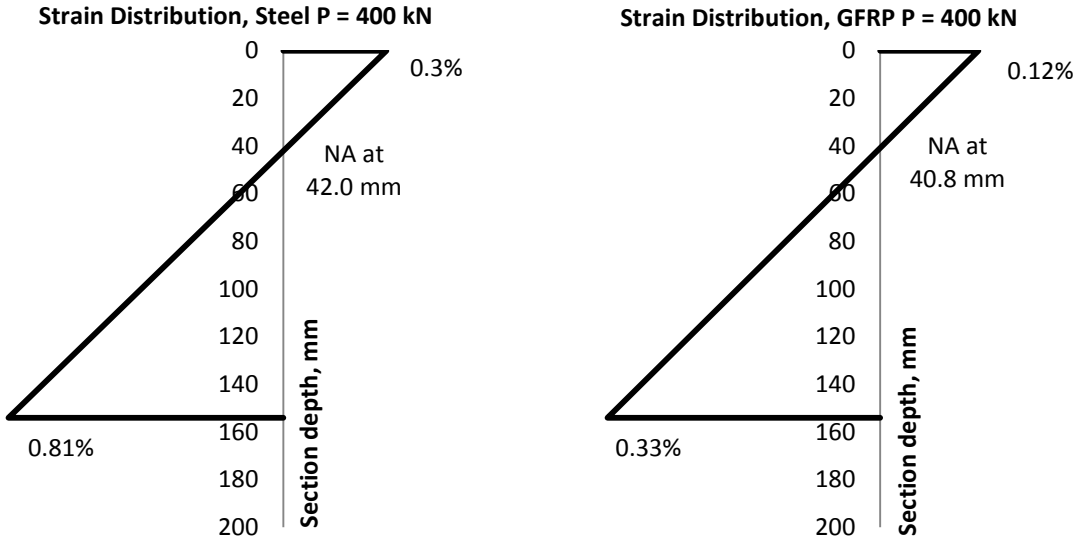

Figure 5-19: Mid-span strain distribution at P = 400 kN for both reinforcement types plotted using experimental strain data.

Failure (steel)

Figure 5-19 shows that the strain levels in the steel section at P = 400 kN are approximately 2.5 times those in the GFRP section, for both the concrete and reinforcement. As the neutral axis positions are quite similar this shows that the load is distributed by similar proportions to the compression concrete tension reinforcement.

The stress in the concrete compression fibre shown in figure 5-20 is only approximate due to the simple models employed to calculate stress. It is assumed that where the concrete stress has reached 50 MPa and then reduced as for the steel case, the concrete will have reached its ultimate strength and the slab will be at (or close to failure). The GFRP bars have only reached 22% of their ultimate strength, so the slab is much closer to failing due to concrete crushing than GFRP bar rupture.

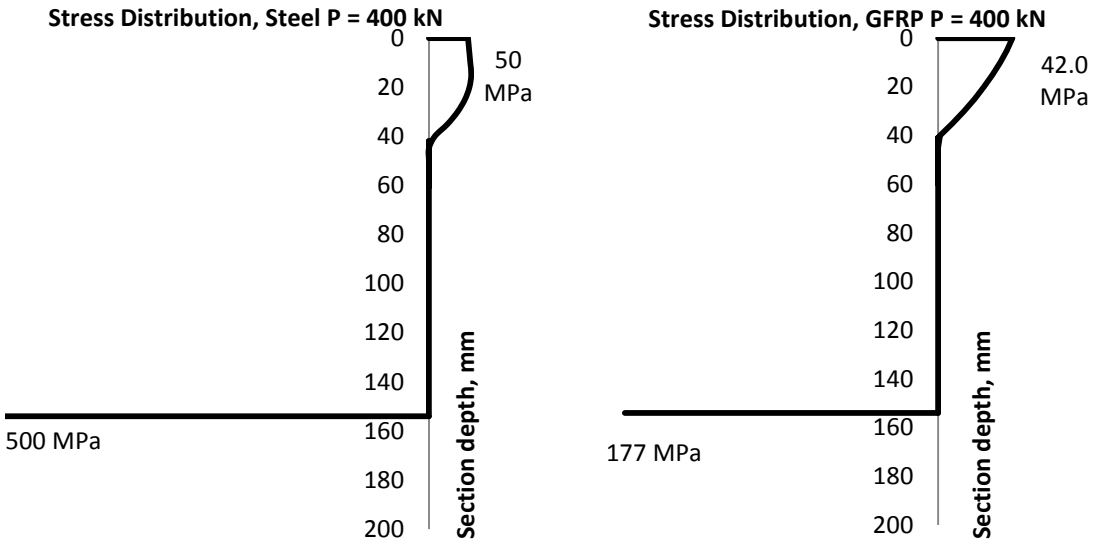

Figure 5-20: Mid-span stress distribution at P = 400 kN for both reinforcement types calculated from the experimental strain data.

5.4 Prediction Models

Several models have been proposed in different studies to predict deflections and crack widths of GFRP reinforced beams and slabs. The beam models will be applied to experimental slab values by assuming a unit width beam section taken from the slab design.

5.4.1 *Deflection*

Deflection is calculated using the following elastic deflection formula created by superposition of the general formula for a point load on a simply supported beam:

$$Midspan\ deflection = \frac{2Qa}{6E_c I_e L}(1250^3 - (L^2 - a^2)1250) \tag{8}$$

where:

$$Q = Load\ applied\ by\ each\ spreader\ beam$$

$$a = 850\ mm\ (shear\ span)$$

ACI committee 440 recommends simple equations based on reviews of existing experimental research at the time of publication, 2006. An expression for the effective moment of inertia, I_e, is used to determine the fraction of the gross moment of inertia, I_g, and the cracked moment of inertia, I_{cr}, that the deflection

behavior is determined from. A modified expression of Branson's equation for effective moment of inertia is given by ACI 440.1R-06:

$$I_e = \left[\frac{M_{cr}}{M_a}\right]^3 \beta_d I_g + \left[1 - \left(\frac{M_{cr}}{M_a}\right)^3\right] I_{cr} \leq I_g \tag{9}$$

where:

$$\beta_d = \frac{1}{5}\left(\frac{\rho_f}{\rho_{fb}}\right) \leq 1.0 \tag{10}$$

M_a is the applied moment considered, and M_{cr} is the moment value at which cracking first occurs. The ratio of M_{cr} to M_a describes whether the section should be transitioning from gross to cracked section behavior. The β_d factor depends on the relative reinforcement ratio. The ratio ρ_f/ρ_{fb} should not be less than 1.4 for a conservative design (failure in due to concrete crushing rather than GFRP bar rupture) so β_d is unlikely to be below 0.28.

Another model by Benmokrane et al. (2005) proposes another expression for I_e in which the transition between I_g and I_{cr} is assumed to be less perfect (Al-Sunna, Pilakoutas, Hajirasouliha, & Guadagnini, 2012).

$$I_e = \alpha_0 I_{cr} + \left(\frac{I_g}{\beta_0} - \alpha_0 I_{cr}\right)\left[\frac{M_{cr}}{M_a}\right]^3 \tag{11}$$

where α_0 and β_0 are 0.84 and 7 respectively. The transition between I_g and I_{cr} happens much earlier for this model than the ACI 440.1R-06 model due to the β_0 factor which accounts for a faster stiffness degradation.

Another deflection prediction model that does not involve calculation of an effective moment of inertia is the model by Razaqpur (2000).

$$\delta_{max} = \frac{2QL^3}{48E_c I_{cr}}\left[3\left(\frac{a}{L}\right) - 4\left(\frac{a}{L}\right)^3 - 8\left(1 - \frac{I_{cr}}{I_g}\right)\left(\frac{L_g}{L}\right)^3\right] \quad (12)$$

where all terms are as defined above and L_g is the length of uncracked beam measured from the supports (assumed to be 500mm in the calculations that follow). This is a much simpler model to use, as it is more compact. However as the effective moment of inertia is not calculated the model does not account for any change in slope to convey the change from gross to cracked section properties.

Figure 5-20 and table 5-5 show a comparison of the deflection prediction models with the G-2 experimental data. Also plotted is deflections calculated with only the gross and cracked moments of inertia as a baseline comparison. It is apparent that the ACI 440.1R-06 model significantly underestimates the observed deflection values. The transition from I_g to I_{cr} happens in this case at approximately the service load which is much higher than the experimental cracking load (~60 kN). This leads to a very inaccurate prediction past the cracking point.

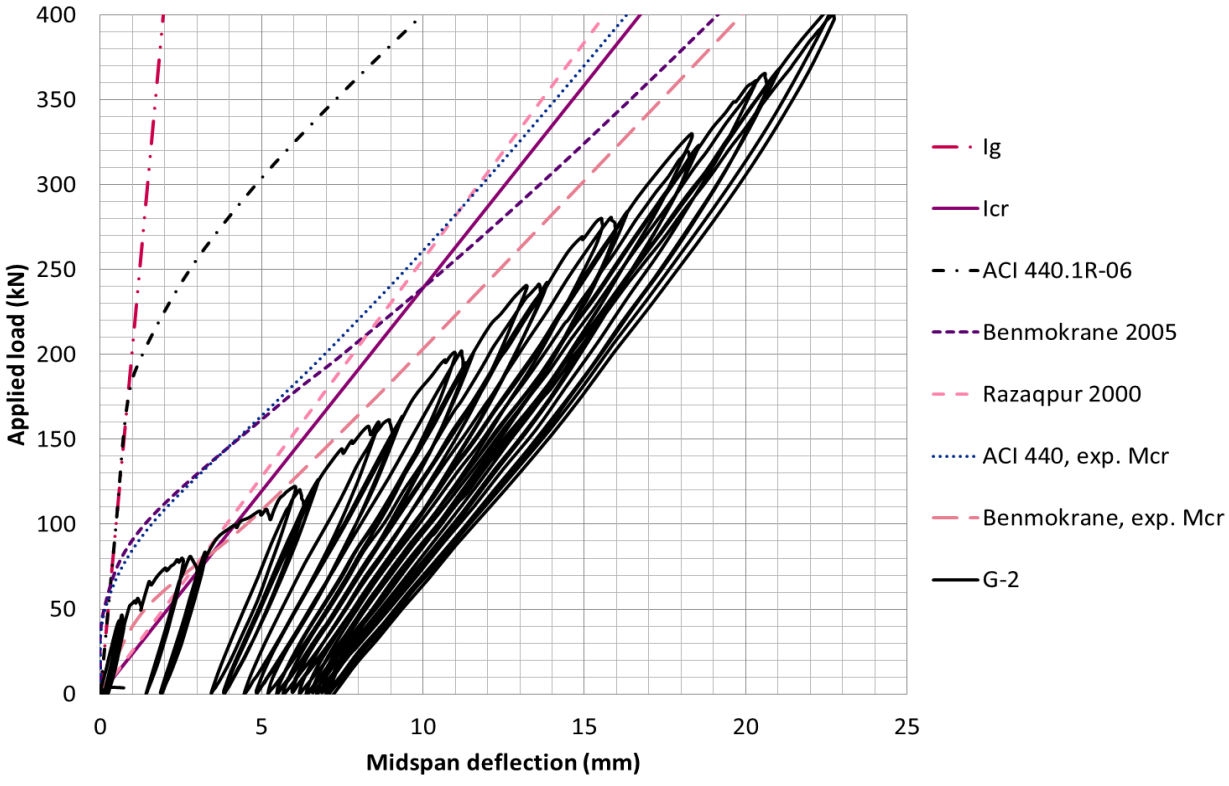

Figure 5-21: Predicted and experimental deflections for GFRP slab in bending

Table 5-5: Midspan deflection in mm at significant load values as observed during testing or calculated using selected equations in literature for the GFRP reinforced slab.

	GFRP					
Applied Load, P (kN)	**Observed**	**ACI 440 (2006)**	**Benmokrane (2005)**	**Razaqpur (2000)**	**ACI 440, with exp. Mcr**	**Benmokrane, With exp. Mcr**
170 kN	10.5	2.3	5.5	7.0	6.6	8.3
250 kN	14.3	6.3	10.7	10.4	10.2	12.4
400 kN	22.3	14.4	19.1	16.6	16.6	19.9

It is clear from figure 5-21 that the section in this case is has made a quick transition into behaving as a fully cracked section so it is unsurprising that the Benmokrane formula here is more accurate than the ACI 440.1R-06 model. In general all deflection predictions underestimate the experimental values. The faster transition assumed by the model proposed by Benmokrane has in some cases (but not this one) lead to overestimates of service deflections (Al-Sunna, Pilakoutas, Hajirasouliha, & Guadagnini, 2012). This formula was calibrated on a limited number of tests, so further improvement may be necessary to make it more appropriate for wider use. Flexibility in the factor β_0 to reflect varying reinforcement ratios as for the ACI 440 equation may help to achieve this. It can be seen that the model by Razaqpur follows closely the deflection profile given by assuming only the cracked section moment of inertia. This model overestimates the deflection initially, but increasingly underestimates the deflection as the load increases.

The deflection was re-calculated using the average experimental value for the cracking moment, M_{cr} at a load value of 60 kN, using both the ACI 440 equation and the Benmokrane (2005) equation as shown in the final two columns of Table 5-5. For both models this improves the accuracy of the deflection prediction. This confirms that the section does transition quickly to fully cracked behavior than predicted by ACI 440.1R-06. The most accurate prediction was given by the Benmokrane (2005) model using an experimental value of M_{cr}.

Other approaches to predicting deflections have been investigated. Kara et al (2012) developed an iterative numerical model (which was not investigated here as it required use of a computer program) considering force equilibrium and strain compatibility. The numerical model was found to more accurately predict experimental values from existing tests from literature than the ACI 440.1R-06 model.

In existing literature approaches to estimate deflections generally underestimate the global deflections but variation in the successful application of a particular model is largely due to differing reinforcement ratios (Saikia, Kumar, Thomas, Rao, & Ramaswamy, 2007). Concrete compressive strength was found to have a significant effect on the moment capacity for over-reinforced sections (Kara & Ashour, 2012). In general, for practical use GFRP sections will be over-reinforced for serviceability and long term behavior requirements. Most models also do not account for any contribution from the top reinforcement which may have a significant effect on deflection for over-reinforced cases. Further research to develop a more accurate model for predicting deflections in over-reinforced sections would be useful for future structural design with GFRP bars.

5.4.2 *Crack Width*

During the experimental testing crack formation and propagation was monitored and recorded. Note that the crack width measurement was done manually using a crack gauge (similar to a ruler), not in any way calibrated or recorded digitally so the experimental measurements can only be treated as approximate.

ACI 440 recommends the use of a formula derived from a physical model which is valid for both steel and GFRP reinforcement, except that it should be modified by a bond coefficient, k_b.

Table 5-6: Crack widths in mm for the steel reinforced slab as observed during testing or calculated using the equation recommended by ACI Committee 440.

Applied Load, P (kN)	Steel	
	Observed	**ACI 440, kb = 1.0**
170	0.1	0.8
400	2.5	3.3

Table 5-7: Crack widths in mm for the GFRP reinforced slab as observed during testing or calculated using the equation recommended by ACI Committee 440.

Applied Load, P (kN)	GFRP		
	Observed	ACI 440, kb = 1.4	ACI 440, kb = 0.65
170	0.1	0.5	0.2
400	0.5	1.2	0.5

Expression for calculating crack widths as given by ACI 440.1R-06:

$$w = 2\frac{f_f}{E_f}\beta k_b\sqrt{d_c^2 + \left(\frac{s}{2}\right)^2} \tag{13}$$

where:

$$f_f = M_s\frac{n_f d(1-k)}{I_{cr}} \tag{14}$$

The bond coefficient is taken as 1 for steel reinforcement. Table 5-6 shows observed and calculated crack widths for the steel reinforced slabs. The calculated crack widths for steel are close for the SLS load, but overestimated for ULS load. This may be due to some additional restraint against cracking from the transverse reinforcement or the large amount of top reinforcement.

Table 5-7 shows observed and calculated crack widths for the GFRP reinforced slabs. A conservative value for k_b of 1.4 should be taken for GFRP bars if kb has not been evaluated from experimental data for a particular product (ACI Committee 440, 2006). Mateen-bar has not had specific research conducted to determine the bond coefficient so the conservative value of 1.4 was first assumed to calculate a predicted crack width value shown in table 5-7. k_b was then varied while keeping all other parameters constant to determine an improved k_b estimate for Mateen bar. A value of 0.65 (shown in the far right column of table 5-7) was determined by trial and error to give the best agreement with the experimental values. As with the steel section, a heavily reinforced section may contribute to smaller crack widths, so the k_b value of 0.65 may in fact be too low for use in design. Further research using a simple beam test with more

accurate crack width measurement can be performed to confirm a lower value of k_b. This will improve the product specifications.

5.5 Summary and Conclusions

This research experimentally investigated the flexural behavior of GFRP reinforced deck slabs.

Based on the experimental and analytical investigation of GFRP reinforced deck slabs, the following conclusions can be drawn:

- Slabs reinforced with steel exhibited a ductile failure mode with yielding of the bars followed by crushing of the top fibre of the concrete.
- Slabs reinforced with GFRP exhibited linear behavior up to cracking, and linear behavior with reduced stiffness after cracking.
- Serviceability requirements are not considered an issue when the GFRP deck design is based on substituting steel for a similar dependable moment capacity. This is largely due to existing strength reduction factors (from design guidelines and manufacturer) which are used to prevent creep rupture.
- Further investigation into long term behavioral properties of this GFRP bar product (and GFRP bar product in general) may reduce the strength reduction factors, allowing a more efficient design.
- In this case the quick transition from gross to cracked section behaviour was not well predicted by the ACI 440.1R-06 model. Improved predictions were given by the Benmokrane (2005) model and when using experimental cracking moment values in the ACI 440.1R-06 model.
- Existing approaches to estimate deflections generally underestimated the global deflections of the GFRP slabs. Most models do not account for any contribution from the top reinforcement. Further investigation is recommended to provide more accurate design equations for over-reinforced sections.

- Further investigation to determine a more accurate value for k_b will improve design guidelines for Mateen-bar as well as provide more insight into whether the ACI Committee equation can be used reliably for heavily reinforced sections or two way slabs in bending.

6 Experimental Slab Testing: Punching Shear

6.1 Introduction

This chapter details the findings of experimental punching shear testing on six full-scale slab specimens as described in Chapter 4. The particular specimens tested were S-4, S-5, S-6 and G-4, G-5, G-6. The behavior of a GFRP reinforced slab was compared with a steel reinforced slab and three repetitions were carried out for each slab type.

6.2 Experimental Programme

6.2.1 *Test set-up*

Testing occurred using the frame set-up shown in figures 6-1 and 6-2. All slabs were tested in the same manner. The force was applied through a hydraulic actuator which was controlled with a manual pump. A single 1000kN load cell was used to measure load applied to the specimens during testing. The load was applied upwards using the hydraulic jack, and the load was transferred to the specimen through a 500 x 200 mm loading footprint. This load area is intended to represent the contact area of a vehicle wheel and was taken from the HN load element (figure 6-3) as given in the NZTA Bridge Manual (2013). Figure 6-4 shows the load footprint and reaction beams. The (upper) reaction beams were positioned in an approximately rectangular position (not fully enclosed on the longer two sides due to available sections), with internal dimensions of 2500 x 2200 mm. The support beams were bolted to six vertical columns to transfer the load to the strong floor for the laboratory. All sections were built up using available beam sections to adequately resist the predicted maximum applied load, with a safety factor of 1.8. The frame was designed conservatively due to the unpredictable nature of the punching capacity of GFRP reinforced concrete slabs.

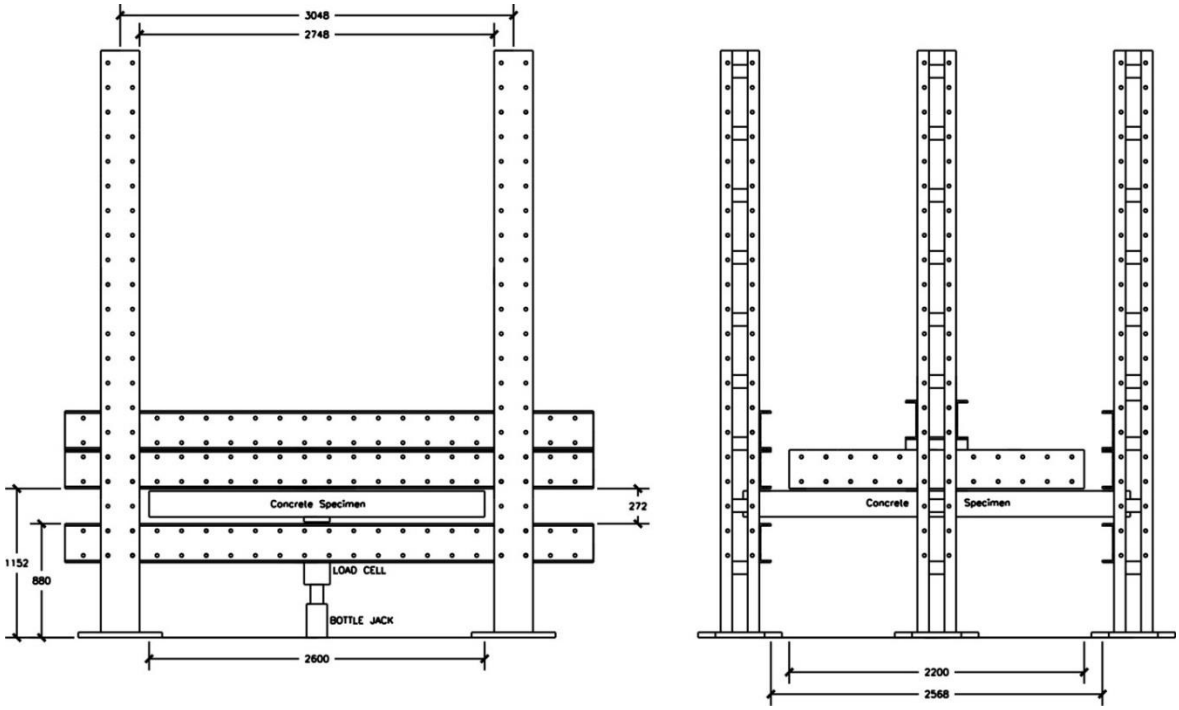

Figure 6-1: Photos of test set-up. Left: Side elevation of load frame and supports for punching shear test. Right: Loading footprint mounted on the load cell and hydraulic jack and supported with temporary timber props.

Figure 6-2: Drawing of test set-up. Left: Front elevation of load frame and supports for punching shear test. Right: Side elevation of load frame and supports. All dimensions are in mm.

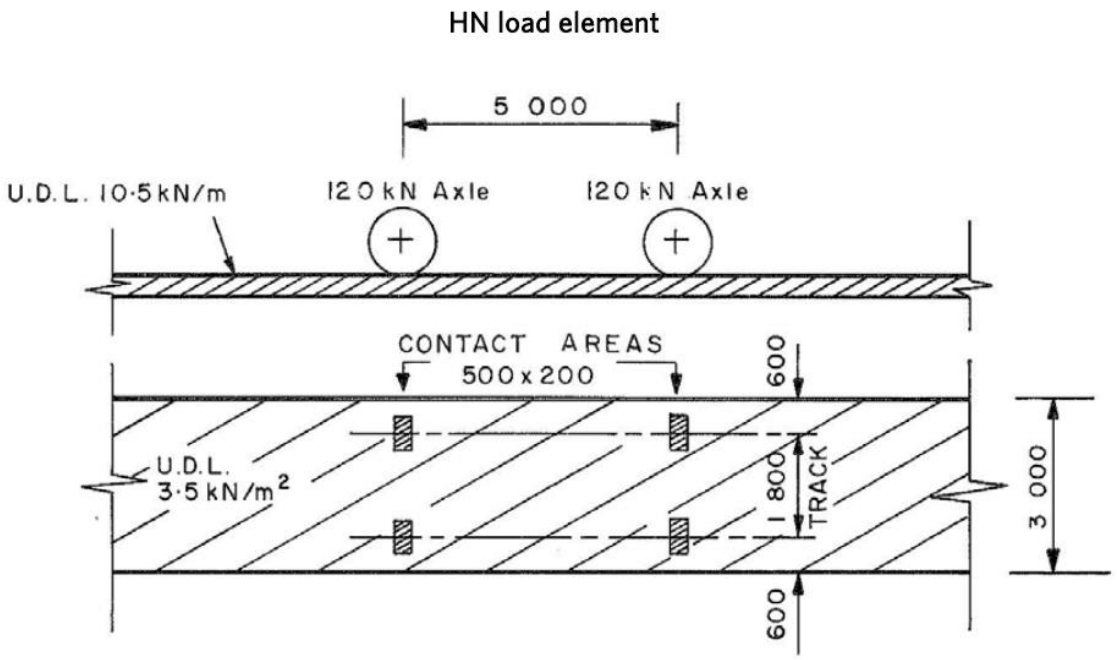

Figure 6-3: HN load element as described in the NZTA Bridge Manual (2013).

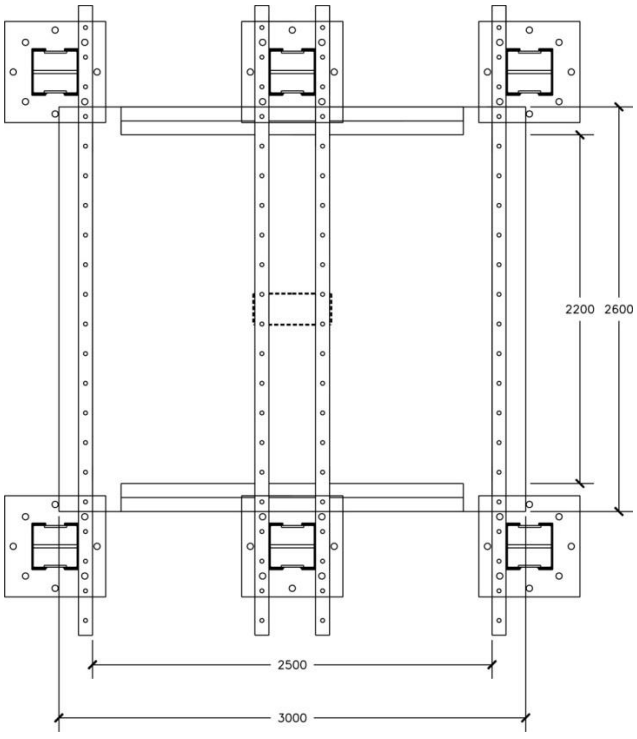

Figure 6-4: Drawing of test set-up in plan view. The load footprint (applied on the underside of the slab) is shown in a dotted outline. All dimensions are in mm.

6.2.2 *Instrumentation*

The layout of the strain gauges is shown in figure 6-5. These were intentionally concentrated around the perimeter of the load area as this was the area where the most strain was expected to develop in the case of a punching shear failure. In addition, linear displacement potentiometers were attached to the surface of the concrete slab to monitor the compressive strain in the concrete. A single string potentiometer was used to monitor the vertical midspan deflection and was attached to the underside of the concrete, 100 mm from the centre of the long side of the load footprint. Figures 6-6 and 6-7 show the positions of the linear potentiometers and string pot. The potentiometers were placed symmetrically to allow an average measurement to be calculated and with some redundancy in case an instrument did not work properly in the testing.

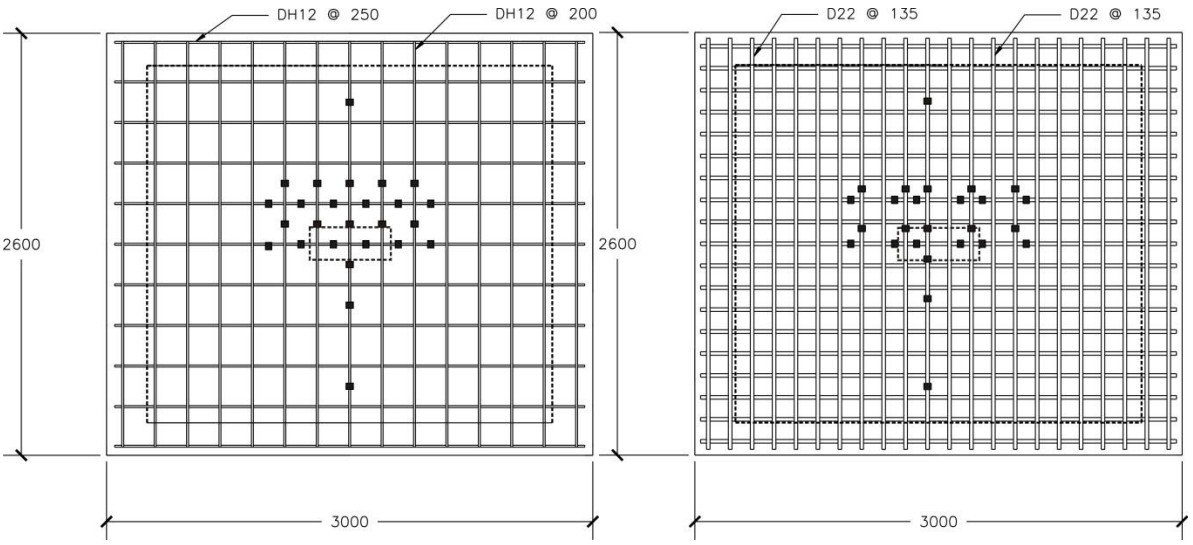

Figure 6-5: Strain gauge layout for steel (left) and GFRP (right) reinforced slab. Note: Only bottom bars shown. Dotted lines show position of load (inner) and supports (outer).

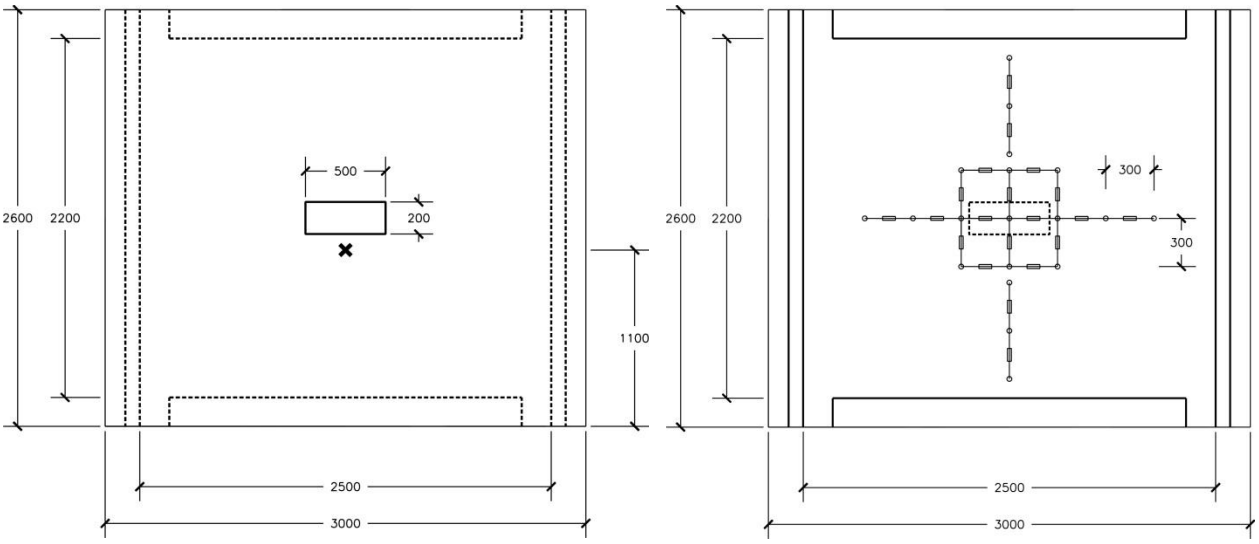

Figure 6-6: Left) String potentiometer position (cross) on underside of slab. Centre rectangle shows position of load footprint and dotted line shows supports. Right) Symmetrical surface rod potentiometer position on slab surface. The gauge length for each potentiometer was 300 mm. Load and supports are portrayed inversely (dotted and bold) to show topside of slab.

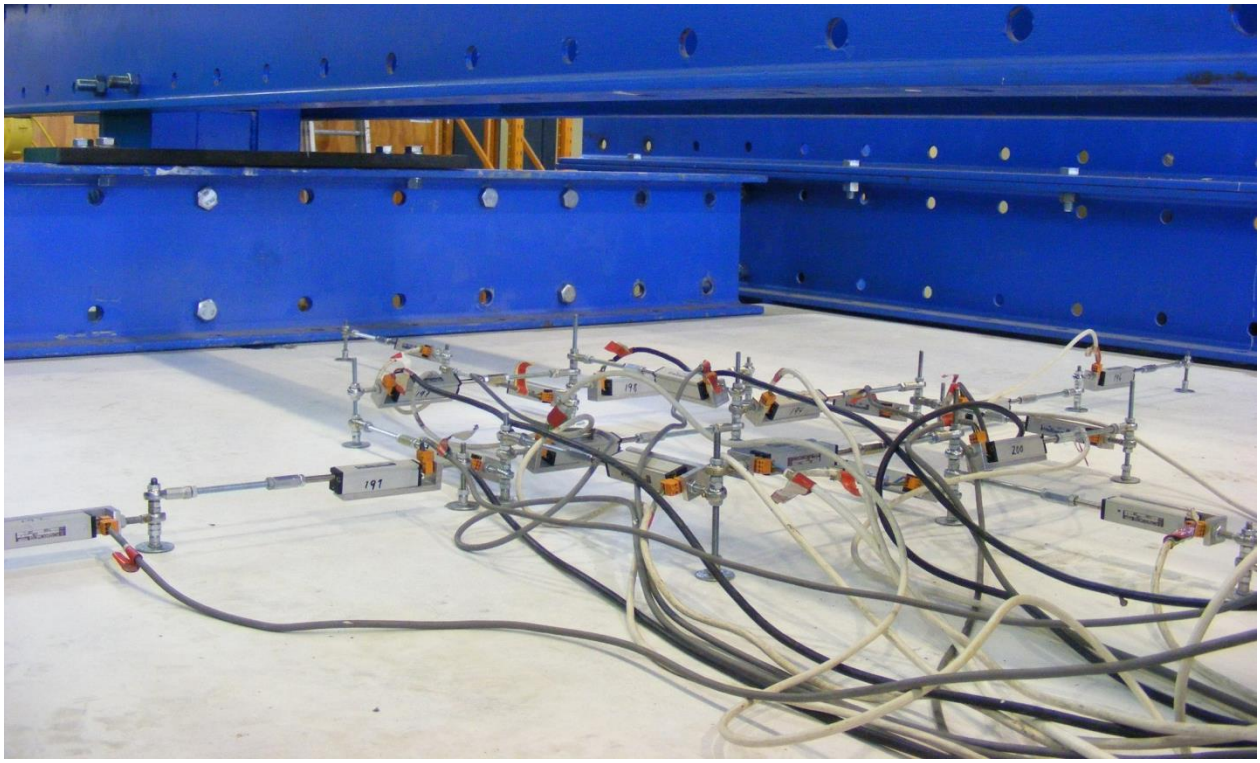

Figure 6-7: Linear potentiometers set up on the top surface of the slab before testing.

6.2.3 *Loading Protocol*

The specimen was loaded in increments of approximately 50 kN and then paused to allow marking of cracks and measurement of crack widths. This process was repeated until failure of the slab. During this time strain and load vs displacement data was monitored. The load vs displacement data as seen in section 6.3 appears quite bumpy as there was some minor unloading each time the test was paused for crack inspection, and to a smaller degree after each motion of the hand pump.

6.3 Results and Discussion

Applied load (P), deflections, and strain data for GFRP and steel reinforced slabs were obtained and compared. The applied load is defined as the load (kN) measured by the load cell during testing. Load values corresponding to serviceability limit state (P_{SLS}) and ultimate limit state (P_{ULS}) were calculated based on loads given in the NZTA (2013) bridge manual. P_{SLS} is equal to 180 kN and P_{ULS} is equal to 300 kN. See Appendix B for the calculations and assumptions made.

6.3.1 *Global Behaviour*

Serviceability and Ultimate

Figure 6-8 shows the total applied load versus the centre slab deflection for each of the slab tests. It is clear from the figure that the results of the three replicate slabs for each reinforcement type were very similar. This indicates that there was good control of materials and specimen manufacture as well as testing procedure. All slabs behaved similarly until the steel bars reached the yield strength and therefore the global stiffness of the section reduced. Overall the capacities of the GFRP and steel reinforced slabs were very similar, excepting the obvious difference due to elastic and yield behavior of GFRP and steel respectively.

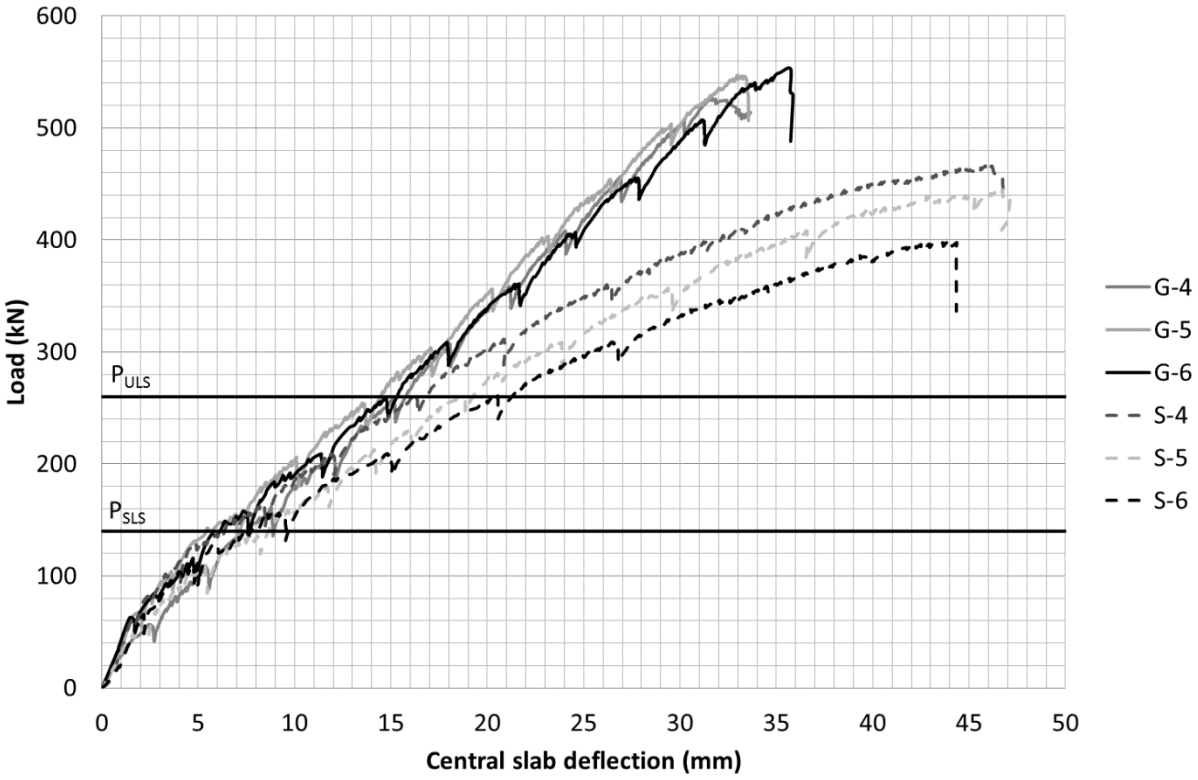

Figure 6-8: Global slab behaviour: Applied load vs midspan deflection of both GFRP and steel reinforced slabs.

Table 6-1: Summary of experimental load data.

Rebar Type	Slab Code	Cracking Load (kN)	Yield Load (kN)	Failure Load (kN)
Steel	S-4	57	160	467
	S-5	45	163	445
	S-6	66	146	398
Average	S-AV	56	156	437
GFRP	G-4	46	na	528
	G-5	62	na	547
	G-6	61	na	553
Average	G-AV	56	-	542

Table 6-2: Summary of experimental deflection data.

		Midspan Deflection (mm)		
Rebar Type	**Slab Code**	**P_{SLS} = 140 kN**	**P_{ULS} = 260 kN**	**Failure Load**
Steel	S-4	6	16	46
	S-5	9	19	47
	S-6	8	20	44
Average	S-AV	8	18	46
GFRP	G-4	8	16	32
	G-5	5	14	33
	G-6	6	15	36
Average	G-AV	6	15	33

A summary of significant loading values and deflections at SLS and ULS are given in tables 6-1 and 6-2. Cracking and yield loads were difficult to identify due to the manual loading which caused a very uneven load displacement curve to be plotted.

Note that the dead load of the slab is excluded in the presentation of the results for simplicity and better comparison (Plots of raw load vs displacement data showed an obvious slip in the system between the ram taking the weight of the slab and any further load being applied. Plots of experimental results presented have been corrected for slip, with dead load also excluded). For this reason an adjusted value of P_{SLS} is used in the analysis of the modified results: $P_{SLS\ (ex\ DL)} =$ 140 kN. The adjusted value of P_{ULS} used in the analysis of the modified results is $P_{ULS(ex\ DL)} =$ 260 kN.

Failure

First steel yielding was assumed to occur at the next apparent change in slope of the load-deflection response curve after the cracking point. Throughout the testing all GFRP reinforcement remained in the elastic range.

Globally the performance of these two slab types was not remarkably different under concentrated loading, when considering the more contrasting performances in the bending only tests presented in Section 5. While the GFRP slabs were on average 24% stronger than the steel reinforced slabs, the main difference in the ultimate deflections was due to the differing tensile properties of the two bar types. The post cracking behavior of the GFRP reinforced slab is clearly elastic, while there is a drop in stiffness of the steel section as load increases indicating yield behaviour.

All steel reinforced slabs failed at an average applied load of 437 kN, while the GFRP slabs failed at an average load of 542 kN. The steel data had a much greater variance in ultimate load, (range was 69 kN for steel reinforced slab ultimate loads, compared to only 25 kN for GFRP) which is presumed to be due to the yield behavior of steel (less predictable than elastic-only behavior of GFRP at relatively low loads).

6.3.2 *Local Behaviour*

Serviceability and Ultimate

During testing cracks formed on the upper surface of the slab (figure 6-8), starting with a few main cracks (indicating flexural behavior) and then spreading out radially in a grid like pattern generally reflecting the spacing of the lower (underside of theoretical bridge) reinforcing grid.

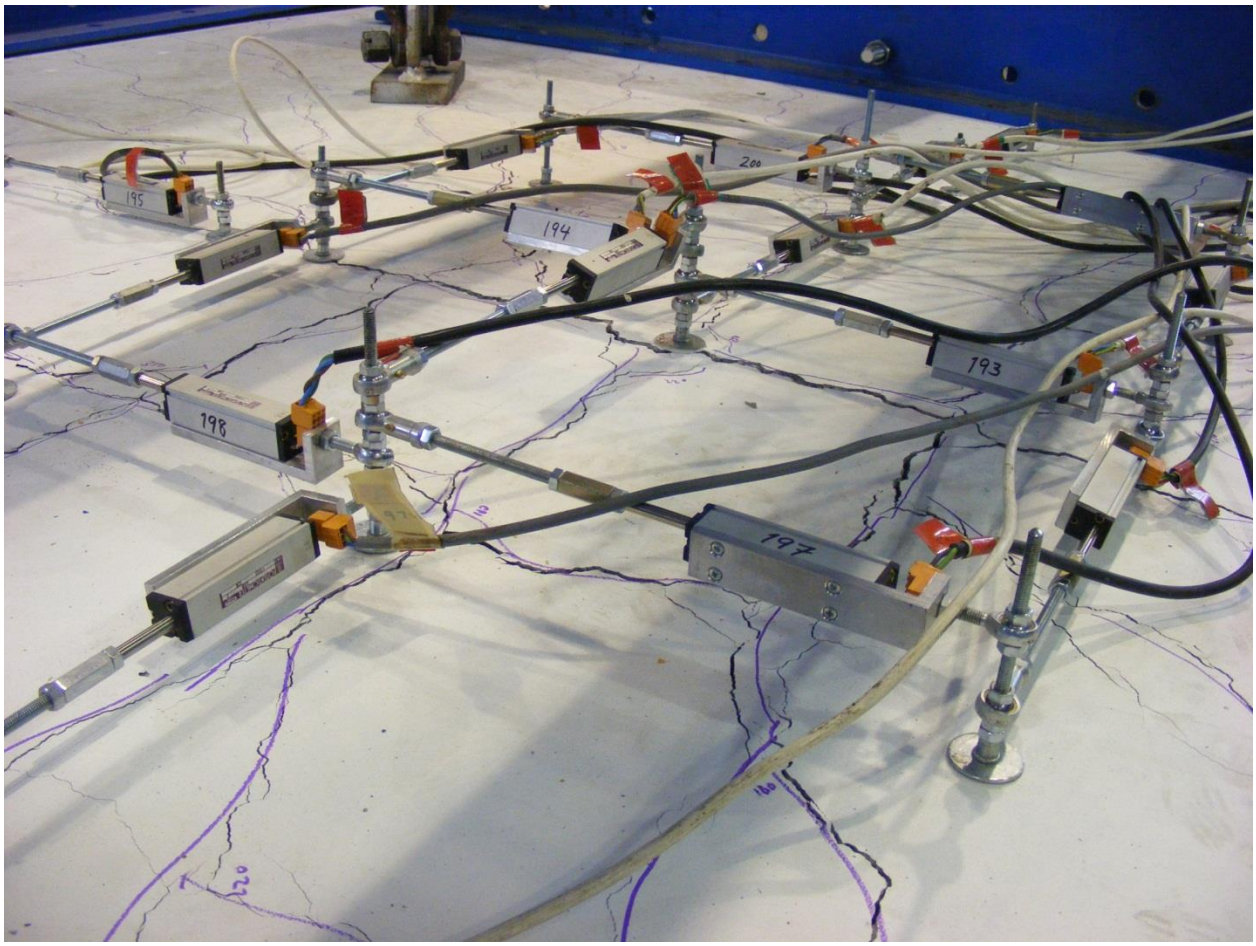

Figure 6-8: Cracks forming as the slab was loaded. Both slab types showed similar crack patterns. Note that it was difficult to obtain clear photographs during testing due to the necessary frame set-up for loading and displacement data collection.

Figure 6-9 shows a comparison of the maximum crack values for the GFRP and steel reinforced slabs averaged for each of the 3 repeated slab tests. Note that the maximum value recorded during testing was not necessarily the maximum value reached before failure, but the last value recorded before it was deemed unsafe take measurements from on top of the slab. The crack width measurement was done manually using a crack gauge (similar to a ruler), not in any way calibrated or recorded digitally so the experimental measurements can only be treated as approximate. At serviceability level the crack widths are relatively close at approximately 0.5 mm. At design ultimate limit state there is a much greater difference between the two slab types; GFRP is approximately 0.8 mm while steel is approximately 2.5 mm.

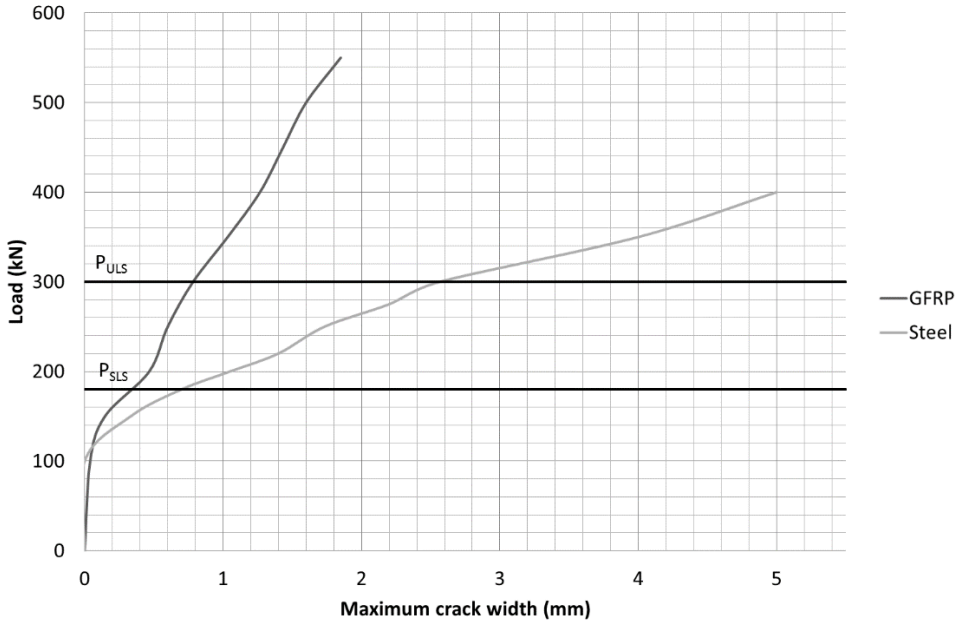

Figure 6-9: Comparison of maximum crack width increase with increasing load.

Failure

All tested deck slabs exhibited a punching shear failure mode around the loaded area. A punching cone developed for each of the slabs. The top surface of the failure zone (corresponding to the underside of the bridge deck) was approximately oval.

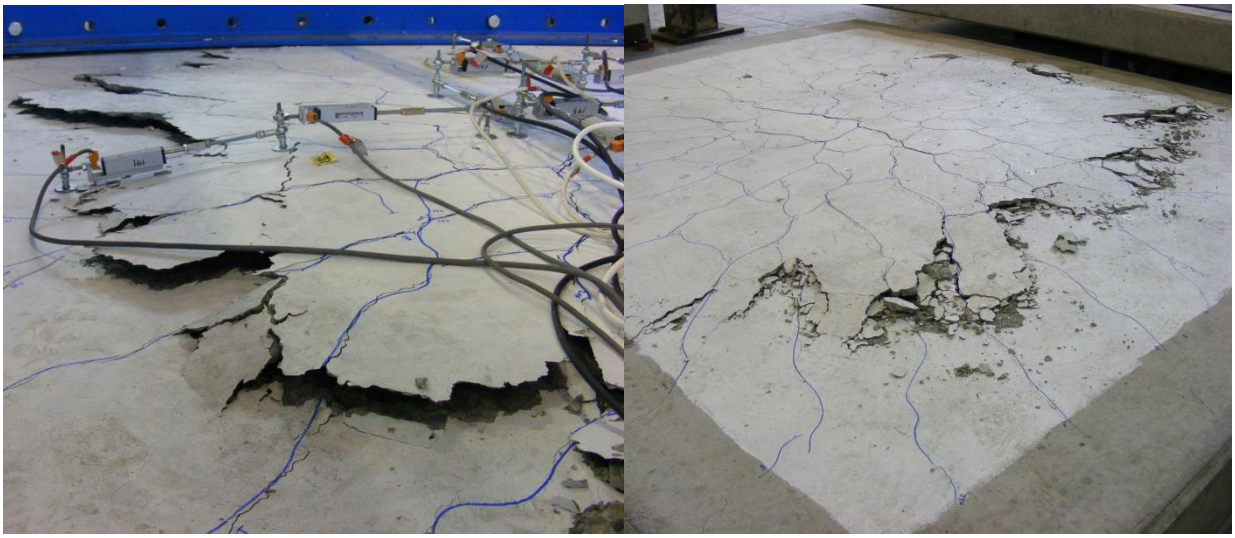

Figure 6-10: Steel reinforced slab at failure. Note the approximately circular failure on the top surface.

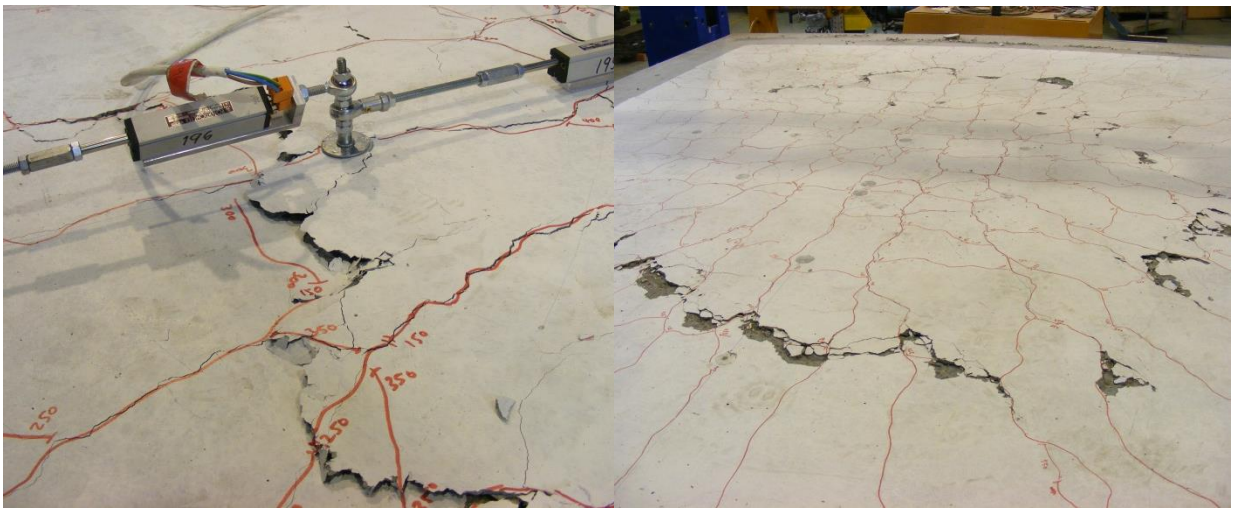

Figure 6-11: GFRP reinforced slab at failure. Note the approximately circular failure on the top surface.

Figures 6-10 and 6-11 show a comparison between the steel and GFRP reinforced slabs respectively at failure and after removal from the testing frame. The damage was visually very similar, with punching cones of similar dimensions forming (approximately 1.75 x 2.0 m oval on the top surface). The GFRP reinforced slab showed less permanent deflection than the steel reinforced slab, as the GFRP bars were still in their elastic range even as the slab itself reached failure. There was more spalled concrete around the punching cone in the steel reinforced case. Figure 6-12 shows a steel reinforcing bar exposed when the loose spalled concrete had been removed by hand.

Figure 6-12: Exposed steel reinforcing bar after excess cracked concrete had been removed from around the punching cone.

Figure 6-13 shows the bottom failure surface (corresponding to the topside of the bridge deck) that was generally rectangular with approximately the same dimensions as the loading footprint. Other than this loading indentation, there was generally no other damage to the compression surfaces.

Figure 6-13: Failure around the 500 x 200 mm loading footprint. This failure was seen for all six slabs.

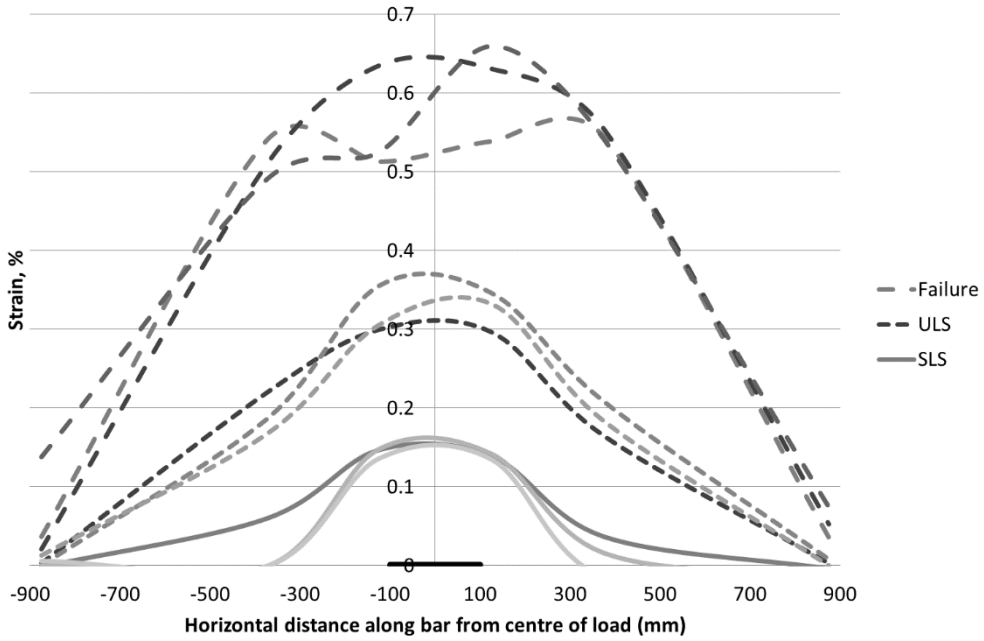

Figure 6-14: Longitudinal section: Average GFRP bar strain distribution horizontally across the loading point at significant load levels. The horizontal bar at 0% strain indicates the 200 mm width of the load footprint in this orientation. Note that 'Failure' indicates failure of the slab, not the GFRP bars which only reached ~40% ultimate capacity around the load footprint.

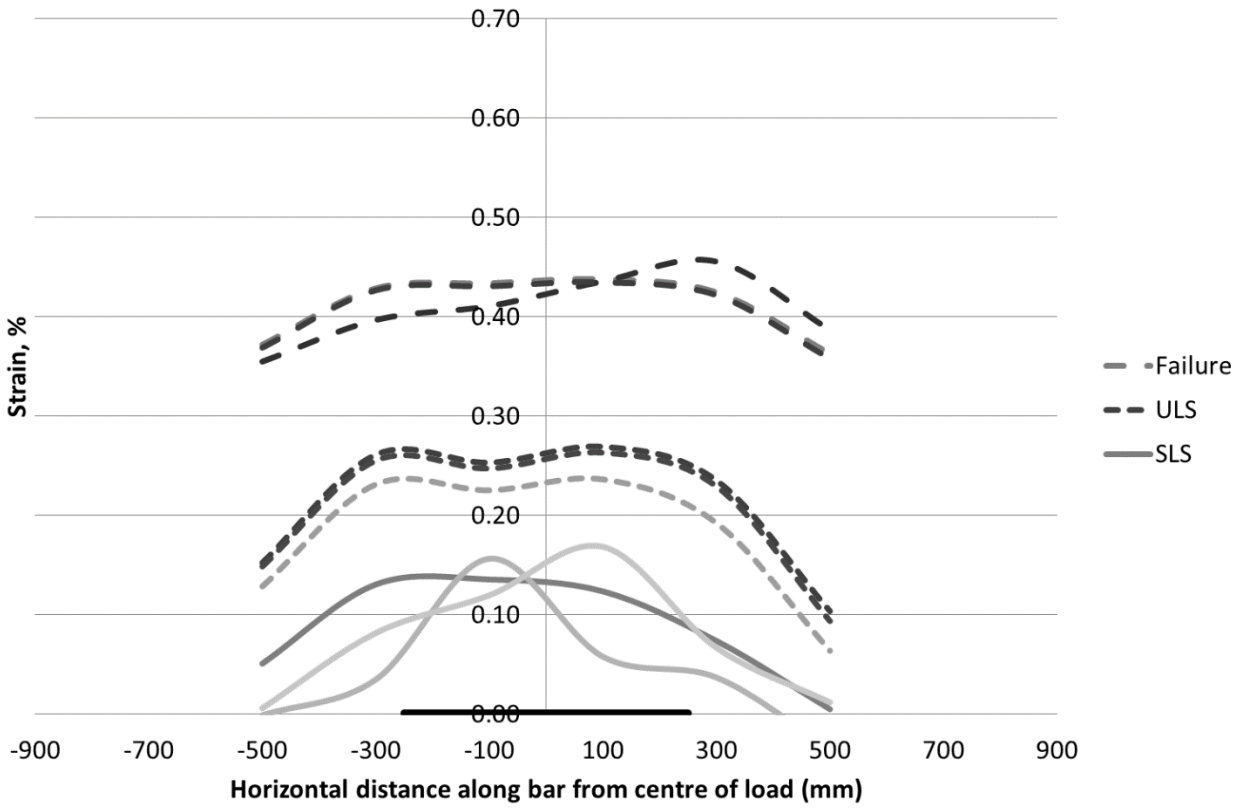

Figure 6-15: Transverse section: Average GFRP bar strain distribution horizontally across the loading point at significant load levels. The horizontal bar at 0% strain indicates the 500 mm width of the load footprint in this orientation. Note that 'Failure' indicates failure of the slab, not the GFRP bars which only reached ~40% of ultimate capacity around the load footprint.

Figures 6-14 and 6-15 are plotted from the strain data obtained during testing from the strain gauges attached to the GFRP bars. Figure 6-14 is a longitudinal section through the centre of the slab and loading area with a 200 mm width of load footprint As the load is increased the strain develops in the bar length from a localized area in the centre (0.4 m at P_{SLS}) to a much wider length of bar (~2m at the point of slab failure) is engaged. In the transverse section in figure 6-15, the load is distributed over a larger distance with a 500 mm width of load footprint. The strain distribution at serviceability is more variable amongst the three tests, most likely due to variability in the initial point of strain development. As the load increases the strain is more evenly distributed along the section of bar immediately above the loading footprint, with a noticeable drop off of strain either side of ~0.8 m of bar length centering over the load.

It can be noted that at the point of GFRP reinforced slab failure the rebar is only at ~0.65% strain in the longitudinal direction. This is less than half of the rupture strain of the GFRP bars used (~1.5%) indicating that the though the slab failure is brittle, it is also only localised and the remaining structure will still have some redundancy which may help to prevent brittle failure.

The strain data for the steel reinforced slabs is not presented in this way as the bars had begun to yield not long after the serviceability limit had been exceeded.

6.4 Prediction Models

6.4.1 *Punching Shear Capacity*

Several models have been proposed in different studies to predict the shear capacity of GFRP reinforced slabs. Most studies on GFRP reinforced concrete slabs consider comparison with steel reinforced slabs by replacing the steel rebar with equal areas of reinforcement. In those cases the axial stiffness (the product of the elastic modulus and reinforcement area) of the section is lower (ACI Committee 440, 2006). This means that the neutral axis is not quite as deep which implies that the compression region of the cross section is also reduced and cracks will be wider.

Nominal shear resistance in a reinforced concrete section, V_n, is the sum of that provided by the concrete, V_c, and the steel shear reinforcement, V_s. In the case of a typical two way slab design, there is no specific shear reinforcement. The concrete contribution to shear strength is understood to be provided by four mechanisms: the contribution from uncracked concrete, aggregate interlock, dowel action and residual stresses across inclined cracks. The ACI 440 committee recognizes that little research has been done to understand the contribution of dowel action from the longitudinal bars to the shear resistance, but they assume that due to lower strength and stiffness of GFRP in the transverse direction the contribution is less than an equivalent steel section. Existing guidelines for GFRP reinforcement design generally exclude dowel action due to GFRP bars having low shear strength.

In the case of these experiments, the GFRP slab is considerably over reinforced when compared to the steel design as the aim of this design was to give the same dependable moment capacity when accounting for long term effects.

Table 6-3 shows a comparison in axial stiffness per metre width of the slab reinforcement, calculated as the total reinforcement area multiplied by the elastic modulus. Also shown is a fictional case in which the steel reinforcement is replaced with an equal area of GFRP reinforcement. Immediately it can be seen that the axial stiffness of the GFRP slab is greater than the steel slab by 65%. Although the elastic modulus of GFRP is a quarter of that of steel, the area of GFRP bars was approximately 7 times that of the steel due to the necessary over-reinforcement. Had the GFRP had the same area as the steel rebar, the stiffness would have been significantly lower than the steel slab by 73%. This clearly shows why there were no issues with the GFRP slab in these experiments being too flexible or showing a lot of cracks at serviceable levels, which was contrary to findings by other researchers who tested beams and slabs with a similar area of steel and GFRP.

Table 6-3: Comparison of reinforcement axial stiffness for the steel slab design, GFRP slab design and a fictional GFRP case with equal reinforcement area to the steel.

	Rebar area ($mm^{2/}m$)	**Elastic modulus (MPa)**	**Axial stiffness (kN) per m**	**AE/AE_{steel}**
Steel	452	200,000	90400	1.00
GFRP (as tested)	2816	53,000	149248	1.65
GFRP (same area as steel)	452	53,000	23956	0.27

Table 6-5 a) and b) gives a comparison of theoretical punching shear strength values calculated using the models from literature (presented in earlier in table 2-3) for the same geometry and material properties as the experimental slab.

Table 6-4 a and b: Comparison between the experimental and calculated punching shear strength of both GFRP (a) and steel (b) reinforced slabs.

a) GFRP	V_c (kN)	V_{exp}/V_c
Experimental, V_{exp}	591	1.00
JSCE (1997)	580	0.98
El Ghandour et al. (1999)	465	1.27
El Ghandour et al. (2000)	2523	0.23
Matthys and Taewre (2000)	2335	0.25
Ospina et al. (2003)	2893	0.20
El-Gamal et al. (2005)	725	0.82
ACI 440.R1-06 (2006)	382	1.55

b) Steel	V_c (kN)	V_{exp}/V_c
Experimental, V_{exp}	442	1.00
ACI 318-05 (2005)	367	1.20
AS/NZS 3101 (2006)	751	0.59

It can be seen that there is considerable variation in the predictions of punching shear strength of GFRP reinforced slabs based on the models from literature. The ACI 440 model underestimates the punching behaviour, as well as the earlier 1999 model by El-Ghandour et al. which is likely due to the model not considering reinforcement ratio. Significant over-estimations of punching shear strength are made by the later 2000 model by El-Ghandour et al. and the models by Matthys and Taerwe and Ospina et al. For this particular slab design it seems that the critical perimeter (at 1.5d away from the perimeter of the load area) used in these three models yields a rather inaccurate prediction. Basic substitution of this critical perimeter with the critical perimeter at 0.5d as used in the other models gives more appropriate (if a little low) values.

The models by JSCE and by El-Gamal et al. are the most accurate predictions from the models evaluated of the experimental behaviour of the GFRP reinforced slab, with some conservatism (~2% and 20% less than the experimental value respectively) as is required for design. The JSCE model takes into account size effect in the formula which other studies have found lead to a more accurate prediction of punching shear capacity than other models (Dulude, Hassan, Ahmed, & Benmokrane, 2013).

Two existing prediction formula for punching shear design of steel reinforced concrete are included for comparison. The ACI 318 model underestimates the punching shear by ~20%, while the AS/NZS model overestimates the capacity by ~40%. This indicates that empirical punching shear strength formulae used in typical reinforced concrete design are not necessarily in agreement.

6.5 Summary and Conclusions

This research experimentally investigated the flexural behavior of GFRP reinforced deck slabs.

Based on the experimental and analytical investigation of GFRP reinforced deck slabs, the following conclusions can be drawn:

- Both slab types (reinforced with steel and GFRP) exhibited a punching shear failure mechanism when tested under simulated wheel loading.
- Slabs reinforced with GFRP exhibited linear behavior up to cracking, and linear behavior with reduced stiffness after cracking.
- A combination of flexural and shear effects were seen during loading of each of the specimens, but all slabs failed with formation of a punching cone.
- The GFRP reinforced slabs in this case produced higher punching shear strengths, greater post-cracking stiffness, and better crack control compared to the steel reinforced slab and the generalized results from literature for GFRP slabs with an equivalent reinforcement area (when compared to steel). This was due to the much higher concentration of reinforcement for the GFRP reinforced slabs in this case.

- Although punching shear is a brittle failure mechanism, when occurring in a GFRP reinforced slab it is highly unlikely for the rebar to reach ultimate strength. This means that even if a structure had a local failure, there would still be significant redundancy in the slab deck to contribute to life safety requirements (e.g. to allow passengers to safely evacuate on foot across a damaged bridge).
- When comparing the relative performance of the GFRP and steel reinforced slabs in flexure and under concentrated loads, punching shear strength must be considered as a possible failure mechanism as it may be more critical than flexural failure.

7 Recommendations for design of GFRP reinforced concrete bridge decks

7.1 Introduction

The purpose of this section is to identify some recommendations for future design of GFRP bridge decks. All recommendations are made in order to improve the efficiency of the design which is largely done by finding acceptable ways to reduce the amount of reinforcement required, thus reducing up-front costs. A process for design including some immediately applicable recommendations is outlined.

7.2 Recommendations

The following are recommendations that could be implemented into a design process with little or no further investigation (though validation would be advised before use in design)

- Ultimate limit state loading could be counted as a short term loading scenario, so it was assumed it would not contribute to any possible creep effects over the long term.
- For serviceable loads, Dead loads could be counted as 'long term' loading and therefore stress limited to the recommended value in ACI440.1R-06 of $0.2f_{pu}$. Live loads are not typically sustained so could be excluded from consideration as 'long term' so the author recommends allowing up to 0.75fpu to resist live load demands at SLS.
- Deflection limits could be increased, allowing more flexible deck systems as this would be well accommodated with GFRP reinforcement. Whether this is appropriate at all would depend hugely on the structure type and importance.
- Cover may be reduced below normal steel RC limits in some instances when using GFRP.

The other recommendations require further investigation to determine the extent of their benefit towards the design:

- More investigation into the long term behavior of GFRP bars. The detrimental effect of creep is the main uncertainty in GFRP reinforced concrete design. More certainty in the behavior of

individual GFRP bars could perhaps mean that the design strength of GFRP bars does not have to be reduced to such a low percentage (currently around 20-30% depending on the manufacturer or design guideline chosen). This would provide designers with more certainty and contribute to GFRP bar products being seen as a more reliable and competitive alternative for steel reinforcing.

- Exploring hybrid solutions which could combine GFRP bars with another reinforcing type, e.g. mild steel or other FRP bars.
- Determine k_b Bond dependent coefficient. This is in reference to the GFRP product used, as some existing products have kb factors provided by the manufacturer.
- Further improvement of the tensile testing procedure and guidelines to improve repeatability of tests therefore improving the reliability of data. This is likely to increase the ultimate tensile strength of bars and therefore the dependable strength used in design.

7.3 Design Outline

The following is an outline of a GFRP bridge deck slab design procedure based on current knowledge. Comments regarding critical design choices are provided. For further guidance refer to ACI 440.1R-06 and the NZTA Bridge Manual.

For the purpose of this design example the second generation (GII) of Mateen-bar will be used. As of November 2014 GII bar data exists for nominal diameters of 6, 8, 10, 16, 25 and 32. The most recent Mateen-bar specifications (November 2014) refer to ACI 440.1R for stress limitations. See Appendix D for the most recent Technical Submittal.

Loads described as being Ultimate Limit State (ULS) are recommended to be treated as short term load (i.e. assuming that no detrimental creep effects will take place). An environmental reduction factor as described in ACI 440.1R-06 of 0.7 should be applied to the ultimate tensile strength to account for ‘creep rupture and fatigue endurance’ as well as moderate temperature effects for both short and long term loading. Table 7-1 shows a comparison of bar design strengths for SLS and ULS based on the reduction

factors mentioned for 25 mm (GII) nominal diameter Mateen-bars. Table 7-2 describes the Design method for a GFRP reinforced concrete slab.

Table 7-1: Design strengths for GII 25mm Mateen-bars applying reduction factors as given by ACI440.1R-06 considering only SLS as long term loading. GTS = 1025 MPa.

25mm, GTS = 1025 MPa	ULS (f_{fu})	SLS – Live Load ($0.2f_{fu}$)	SLS – Dead Load ($0.75f_{fu}$)
Reduction factor	0.7 (Environmental)	0.7*0.2	0.7*0.75
Design strength (MPa)	717.5	143.5	538.1

Table 7-2: Design Method: Main tension reinforcement for a bridge deck slab.

Design Procedure:	**Calculation example:**
Determine the following design inputs/constraints. Geometry of slab, including depth and span length. Concrete target compressive strength. Cover concrete depth. In some cases is may be reasonable to reduce the cover (when compared to typical steel reinforcement cover). In the example this has been kept at a reasonable 40 mm as reducing cover may lead to splitting failure and decrease of bond strength.	For simplicity assume the same geometry as for the test specimens. Span between beams = 2.5m Depth = 200 mm Cover = 40 mm
Define applied loads and determine moment and shear demands Knowledge of the loading type (in a bridge deck design this includes concentrated loads) allows an efficient design to be found by considering all possible failure mechanisms. Punching shear may be a design constraint depending on the depth of the slab. Further guidance on the loading combinations to consider can be found in the NZTA Bridge Manual.	**Dead Loads** calculated per m width of slab: <u>Self-weight:</u> UDL: 0.2m*24kN/m^3 = 4.8 kN/m per m Moment: 4.8*2.5m^2/8 = 3.75 kNm/m <u>Superimposed dead load:</u> Surfacing + future services = 1.5 kN/m^2 + 0.25 kN/m^2 = 1.75 kN/m^2 (NZTA BM) Moment: 1.75x2.5m^2/8 = 1.4 kNm/m Total DL moment: 5.1 kNm/m MDL(SLS) =1.0*5.1 = 5.1 kNm/m MDL(ULS) =1.35*5.1 = 6.89 kNm/m

	Live Loads For simplicity will assume a 60 kN nominal wheel load at midspan and ignore the UDL load as defined in NZTA Bridge Manual. Span 2.5m between beams. Punching shear load: V*= 2.25*(60) = 135 kN Max ULS moment demand per m width: M*= 2.25(60x2.5/4) = 84.4 kNm Max SLS moment demand per m width: M*= 1.35(60x2.5/4) = 50.6 kNm
Choose bar type and size. Ensure reference to the particular specifications of the product manufacturer as no two GFRP bar designs are likely to be the same. Choosing a smaller bar size (while still being practical for the scale of the design) may be beneficial as design strengths increase as bar diameters decrease.	Using Mateen-bar. Choose size 25 mm diameter, second generation (GII). Area of single bar = 460 mm^2 Guaranteed Tensile Strength: 1025 MPa Tensile Modulus, E_f = 58 GPa
Determine effective depth, d, of the section. Choose an approximate position of GFRP to achieve necessary cover (~35mm).	Using 40 mm cover, d = 200 – 40 – 25/2 = 147.5 mm
Calculate punching shear capacity. Ensure by capacity design principles that the shear capacity of the reinforced concrete section is greater than all shear demands. $$\emptyset Vc \geq V^*$$ The author recommends the use of the model by El Gamal et al. (2005) to predict punching shear strength (as of the two most accurate models found in the experimental study this is the most simple to use). $$V_c = 0.33\sqrt{f_c'} b_{0;0.5d} d\alpha$$	V* = 135 kN Φ = 0.75 Calculate the value of α required to ensure the shear capacity exceeds the design value. Using a 200 x 500 load footprint: $b_{0:0.5d}$ = 2008 mm $$\alpha = \frac{V^*}{\emptyset 0.33\sqrt{f_c'} b_{0;0.5d} d}$$ $$\alpha = \frac{135000}{0.75 \times 0.33 \times \sqrt{40} \times 1990 \times 147.5}$$ $$\alpha = 0.3$$ Determine the minimum reinforcement ratio

$$\alpha = 0.5(\rho_f E_f)^{\frac{1}{3}}\left(1+\frac{8d}{b_{0;0.5d}}\right)$$ Increase the slab depth, concrete strength or reinforcement ratio as needed to achieve a satisfactory punching shear capacity.	required to achieve the necessary punching shear capacity: $$\rho_f = \frac{\sqrt[3]{\frac{\alpha}{0.5\left(1+\frac{8d}{b_{0;0.5d}}\right)}}}{E_f}$$ $$\rho_f = 1\times10^{-5}$$ This is such a small ratio that is likely that any reinforcement configuration required for bending strength will significantly exceed this.
Determine reinforcement ratio to satisfy ULS loading demands. Find balanced reinforcement ratio, ρ_{fb}. $$\rho_{fb} = 0.85\beta_1\frac{f_c'}{f_{fu}}\frac{E_f\varepsilon_{cu}}{E_f\varepsilon_{cu}+f_{fu}}$$ Ensure failure by concrete crushing by using $1.4\rho_{fb}$ to determine reinforcement quantity and spacing. Calculate the stress in the reinforcement at ultimate limit state to determine the moment capacity of the section. $$f_f = \left(\sqrt{\frac{(E_f\varepsilon_{cu})^2}{4}+\frac{0.85\beta_1 f_c'}{\rho_f}E_f\varepsilon_{cu}}-0.5E_f\varepsilon_{cu}\right)$$ $$\leq f_{fu}$$ $$M_n = A_f f_f\left(d-\frac{a}{2}\right)$$ $$a = \frac{A_f f_f}{0.85 f_c' b}$$ Φ is 0.65 for sections with $\rho_f \geq 1.4\rho_{fb}$	Environmental reduction factor for GFRP reinforced concrete exposed to weather, $C_E = 0.7$ $$f_{fu} = 0.7\times1045 = 717.5\ MPa$$ $$\rho_{fb} = 0.007$$ $$1.4\rho_{fb} = 0.0098$$ $$\rho_f = \frac{A}{bd}$$ $$Amin = \rho_f bd = 0.0098\times1000\times147.5$$ $$= 1451.5$$ # bars per m = 1451.5/460 = 4 bars $$A_f = 4\times460 = 1840\ mm^2$$ Spacing = 1000/4 = 250 mm $$f_f = 519.6\ MPa$$ $$a = 28\ mm$$ $$M_n = 127.6\ kNm$$ $$\emptyset M_n = 82.9\ kNm$$ This is currently less than M* = 6.89+84.4 = 91.3 kNm, so additional reinforcement is required. 25 mm nominal diameter bars at 225mm spacing gives φMn =110 kNm.
Check design against SLS loading demands. Determine cracking and deflection limits for the structure. As much of the reinforcement is inherently redundant for SLS calculations and GFRP not corrodible, both deflection and crack	**Check deflection:** c = 30.5 mm Icr = 64.1 x10^6 mm^4 Ie = 131.8 x10^6 mm^4

width limits may be relaxed slightly depending on the structure importance and client requirements.

Assuming cracked, elastic behaviour find neutral axis position, c, and use to calculate cracked moment of inertia.

$$\frac{bc^2}{2} - nA_f(d-c) = 0$$

$$n = \frac{E_f}{E_c}$$

$$I_{cr} = \frac{bc^3}{3} + nA_f(d-c)^2$$

$$I_e = \left[\frac{M_{cr}}{M_a}\right]^3 \beta_d I_g + \left[1 - \left(\frac{M_{cr}}{M_a}\right)^3\right] I_{cr} \leq I_g$$

Deflection at midspan due to a concentrated load is

$$\Delta = \frac{PL^3}{48E_cI_e}$$

Deflection at midspan due to a distributed load is

$$\Delta = \frac{5wL^3}{384E_cI_e}$$

Find stress in GFRP bars under max SLS moment and check that it doesn't exceed $0.2f_{fu}$ for dead load and $0.75f_{fu}$ for live load.

$$f_f = \frac{M^*}{A_f\left(d - \frac{c}{3}\right)}$$

Check crack widths are acceptable. As GFRP does not corrode, greater crack widths may be acceptable than for steel RC design.

$$w = 2\frac{f_f}{E_f}\beta k_b \sqrt{d_c^2 + \left(\frac{s}{2}\right)^2}$$

Δ= 6.7 mm

Deflection limit in NZTA bridge Manual for RC structures is span/1000 = 2.5 mm.

It is proposed that for the purpose of this example an increased deflection limit of span/500 = 5mm be used

Need additional reinforcement.

25 mm nominal diameter bars at 125mm spacing gives c = 39.4, and Δ= 5.0 mm.

Check SLS stress limits:

$f_{f\ DL}$ = 10.3 MPa (This is less than the 20% limit, $0.2f_{fu}$ = 143.5 MPa. Ok.)

$f_{f\ LL}$ = 102.3 MPa (This is less than the 75% limit, $0.75f_{fu}$ = 538 MPa. Ok.)

Check crack widths:

Assume GFRP bond strength as good as steel;

k_b = 1.

β = (h-c)/(d-c) = 1.49

w = 0.47 mm

Normal bridge crack width limits for reinforced concrete (NZTA Bridge Manual) are 0.35mm. For the purpose of this design example it can be assumed that this acceptable as corrosion is not a risk for GFRP.

Final summary of example design, with capacities calculated based on final reinforcement

design:

Main tension reinforcement:

25 mm nominal diameter bars at 125 mm spacing, $\rho_f = 0.025$

Punching shear capacity:

$\varphi Vc = 4139$ kN

Moment capacity ULS:

$\varphi Mn = 179.7$ kNm

Deflection SLS:

$\Delta = 5.0$ mm

Max crack width SLS:

$w = 0.27$ mm

Serviceability limit criteria were the limiting factors for this particular design rather than punching shear or ultimate limit state strength. The relatively deep pre-defined section depth ensured that punching shear was not a likely failure mechanism.

8 Conclusions

This thesis investigated the use of GFRP reinforcement in bridge decks for situations, such as coastal New Zealand, where the non-corrosive benefits of GFRP may offer an alternative to traditional mild steel reinforcement. GFRP use as structural reinforcement may offer life-cycle cost benefits for certain structures as maintenance to repair corroded reinforcement is not necessary. The use of GFRP reinforcement in a New Zealand design context was investigated to directly compare the structural performance of this alternative reinforcing product. Mateen-bar, manufactured by Pultron Composites Ltd, is the GFRP reinforcing bar used in the experimental tests.

Experimental investigation of tensile properties of GFRP bar samples was carried out to understand the mechanical behaviour of GFRP reinforcement and validate the manufacturer's specifications for Mateen-bar. This included 8-10 tensile tests each of 10, 12, 16 and 22 mm nominal diameter Mateen-bar samples to determine the Ultimate Tensile Strength, UTS, and Tensile Modulus of Elasticity, E, of the different bar diameters. Each bar failed in a brittle fracture resulting in splitting of the bar into many shards parallel to the longitudinal axis of the bar. This series of tests highlighted the complexities of carrying out tensile testing of FRP products due the inability to grip the GFRP directly in a testing machine without crushing the specimen. All tests gave a higher 'guaranteed tensile strength' value than that in the product specifications. Reproducibility of tests is important to achieve reliable design strength values, and it is clear from the comparison between the experimental and specified UTS values that the same strength values have not been achieved in other in-house and independent tests of the product resulting lower specified values given by the manufacturer for Mateen-bar. The experimental values of elastic modulus, E, were in good agreement with those specified by Pultron for Mateen-bar (51-53 MPa). Further improvements and regulations the for tensile testing method for GFRP bars focusing on achieving consistent results will help to improve reliability of data and likely increase the dependable strength of the bars for design purposes. This will also contribute to less variability between bar products and therefore increase industry confidence in the use of GFRP bar products for concrete reinforcement.

Two phases of full-scale tests were carried out to compare the performance of bridge deck slabs reinforced with typical mild steel and GFRP reinforcing bar. This experimental testing was different to most existing research on GFRP reinforced slab performance as it did not compare the performance of a GFRP reinforcing bar area equivalent to steel, but was designed in such a way as to dependably give the same moment capacity of the steel reinforced slab design. This incorporated the recommended limit of 20% of design stress given by the manufacturer which led to an apparent over-reinforced section for the GFRP slab design. As both tests only investigated the short term behaviour of the slabs, at a first glance this over-reinforcement may seem unnecessary, but the aim of the experiment was to investigate the comparative performance of a typical New Zealand bridge deck design and a GFRP reinforced equivalent designed in such a way as is currently recommended by the manufacturer. The over-reinforcement lead to differences in conclusions drawn by other authors who have studied GFRP reinforced slab behaviour.

In the first experimental slab testing phase the behaviour of the two slab designs was tested under a four-point (cross-sectional) bending load. This allowed direct comparison of the flexural behaviour of the GFRP and steel reinforced slabs in the zone of constant moment between load points. The typical steel reinforced slab design behaved with a ductile failure mode due to the yielding of the bars and crushing of the top fibre of the concrete. It was noted that the existing slab design was considerably stronger than the approximate ultimate limit state load calculate based on the NZTA Bridge Manual. This indicates that some investigation could be done into further improvement and optimisation of traditional steel reinforced concrete bridge deck design.

In the case of the GFRP reinforced slab, the post-cracking stiffness was linear due to the elastic properties of the GFRP bars. Due to the considerable over-reinforcement of the GFRP design the slab was unable to reach failure in the available testing rig, however extrapolation of data assuming failure due to concrete crushing rather than bar rupture indicated that the GFRP slab had approximately 3 times the capacity of the steel design. It was noted that due to the considerable over-reinforcement of the GFRP slab, serviceability requirements were not an issue, as the slab had a short-term capacity much greater than

required to achieve serviceable performance. Comparison of several deflection prediction models for GFRP reinforced slabs indicated that most lead to underestimation for over-reinforced sections. In the case of current GFRP slab design, it is understood that in most structural applications the concrete section will need to be over-reinforced with GFRP. The model which gave the closest approximation (though still underestimating deflection by ~3mm post-cracking) was the 2005 model by Benmokrane. Crack widths were noted and compared with the model found to be most common for predicting crack widths recommended by ACI Committee 440. Tests indicate that the bond coefficient used to calculate crack widths could be as low as ~0.65 for Mateen-bar, indicating that the bond strength is better than a typical steel reinforcing bar.

The second experimental phase investigated the behaviour of the two slab designs under a wheel load, as simulated by a concentrated load footprint of 500 x 200 mm. Both slabs exhibited a punching shear failure and, aside from the differences in reinforcement properties (yield behaviour of the steel, and fully elastic behaviour of the GFRP) which were evident in the global force – displacement plots, both had similar capacities. This shows that no matter how over-reinforced with GFRP a slab may be to accommodate flexural loads, the punching shear resistance is often a critical failure mechanism for GFRP reinforced slabs where concentrated loads are possible. The over-reinforcement of this particular GFRP slab design saw better crack control, higher post-cracking stiffness and a higher punching shear strength than the steel design. Other studies have found an inferior punching shear performance of GFRP reinforced slabs as they have compared equivalent GFRP and steel reinforcement areas, which in practise is an unsafe way to approach GFRP reinforced concrete design. Monitoring the strain of the tension reinforcement during testing showed that less than half of the ultimate capacity of the GFRP bars was reached at the point of global failure of the slab. This indicates that the structure will still exhibit some redundancy in the event of a localised failure. This is less likely in the case of a steel reinforced slab as the bars were found to have yielded not long after the serviceability limit state had been exceeded. Existing punching shear strength models used for GFRP reinforced slab design are generally empirically

derived and often modifications of steel reinforced slab design formula. Other studies have found large variation in punching shear predictions given by existing models from literature, and the values calculated using these models in this experimental phase also showed a large variation. The models that most closely predict the experimental values from this study were the model by JSCE (1997) and El-Gamal et al. (2005).

Based on the findings from the extensive experimental phases, a set of design recommendations were made to further improve the potential for GFRP to be used for bridge deck design in a New Zealand context.

8.1 Future Research

Further investigation into long term behavioural properties of this GFRP bar product (and GFRP bar products in general) may mean the design strength does not have to be reduced to such a low percentage (currently 20% for Mateen-bar) allowing a more efficient design with less rebar required for ULS design. This would contribute to GFRP bar products being seen as a more reliable and competitive alternative to steel reinforcing. Some redundancy will still be required however for robustness and to achieve appropriate system ductility.

Further investigation could be done considering short-term loading overloading scenarios such as High Productivity Motor Vehicle (HPMV) loading. Some short term overloading may be acceptable relying on a greater portion of the ultimate tensile bar strength (than is recommended for sustained loads) as this is unlikely to contribute to creep behaviour.

As existing approaches to estimate deflection of GFRP reinforced structures generally underestimated the global deflections of the experimental slab tests, further investigation to develop more accurate design equations focusing on over-reinforced slab sections is recommended to better represent a typical bridge deck.

Confirming the k_b value in smaller scale beam tests will improve the product specifications of Mateen-bar.

An opportunity for further investigation (which was not considered in this research) may be to examine the feasibility for the beams of the bridge to be pre-stressed with GFRP tendons.

Using a combination of different reinforcement types in the bridge deck design may be considered, such as using both steel and GFRP or a combining GFRP with other FRP bar products.

An important final point is to highlight the importance of consulting the manufacturer for the specified strengths and any particular design requirements when designing with GFRP. It is paramount that generalized GFRP properties are not used, as mechanical properties including tensile strength, stiffness and bond strength vary greatly between different bar product types and sizes.

References

Abdalla, H. (2002). Evaluation of deflection in concrete members reinforced with fibre reinforced polymer (FRP) bars. *Composite Structures*.

ACI Committee 440. (2006). *Guide for the Design and Construction of Structural Concrete Reinforced with FRP bars.* Farmington Hills, Mich: American Concrete Institute.

Al-Sunna, R., Pilakoutas, K., Hajirasouliha, I., & Guadagnini, M. (2012). Deflection behaviour of FRP reinforced concrete beams and slabs: An experimental investigation. *Composites Part B, 43*, 2125-2134.

ASTM Committee D30. (2006). Standard Test Method for Tensile Properties of Fiber Reinforced Polymer Matrix Composite Bars.

Benmokrane, B., & Wang, P. (2002). Durability of FRP composites for civil infrastructures applications, a state of art report. *Journal of Composites for Construction, 6(2)*, 143-153.

Benmokrane, B., Challal, O., & Masmoudi, R. (1996). Flexural response of concrete beams reinforced with FRP reinforcing bars. *ACI Structural Journal, 93*(1), 46-55.

Bentz, E. C., Massan, L., & Collins, M. P. (2010). Shear Strength of Large Concrete Members with FRP Reinforcement. *Journal for Composites in Construction*.

Berg, A., Bank, L., Oliva, M., & Russel, J. (2006). Construction and cost analysis of an FRP reinforced concrete bridge deck. *Construction and Building Materials 20*, 515-526.

Bouguerra, K., Ahmed, E., El-Gamal, S., & Benmokrane, B. (2011). Testing of full-scale concrete bridge deck slabs reinforced with fiber-reinforced polymer (FRP) bars. *Construction and Building Materials 25*, 3956-3965.

Deitz, D. H., Harik, I. E., & Gesund, H. (1999). *One-way slabs reinforced with glass fiber reinforced polymer reinforcing bars.* ACI Proc, 4th Int. Symp.

Dolan, C. W., Bakis, C. E., & Nanni, A. (2001). *Design recommendations for concrete structures prestressed with FRP tendons.*

Dulude, C., Hassan, M., Ahmed, E. A., & Benmokrane, B. (2013, September-October). Punching-Shear Strength of Normal and High-Strength Two-Way Concrete Slabs Reinforced with GFRP Bars. *ACI Structural Journal, 110*(5), 723-733.

Ehsani, M. R., Saadatmanesh, H., & Tao, S. (1996). Design Recommendations for Bond of GFRP Rebars to Concrete. *Journal of Structural Engineering, Vol 122, No. 3*, 247 - 254.

El-Gamal, S., El-Salakawy, E., & Benmokrane, B. (2007). Influence of Reinforcement on the Behaviour of Concrete Bridge Deck Slabs Reinforced with FRP Bars. *Journal of Composites for Construction, Vol. 11*(No. 5), 449-458.

El-Ghandour, A. W., Pilakoutas, K., & Waldron, P. (2003, August). Punching Shear Behavior of Fiber Reinforced Polymers Reinforced Concrete Flat Slabs: Experimental Study. *Journal of Composites for Construction, Vol. 7*(No. 3), 258-265.

El-Salakawy, E., Benmokrane, B., & Desgagne, G. (2003). Fibre-reinfroced polymer composite bars for the concrete deck slab of Wotton Bridge . *Canadian Journal of Civil Engineering*, 861 - 870.

Feldman, L., Boulfiza, M., Zacaruk, J., Christensen, P., & Sparks, G. (2008). Life cycle deterioration and cost comparison of bridge deck designs including rehabilitation strategies. *Life-Cycle Civil Engineering: Proceedings of the International Symposium on Life-Cycle Civil Engineering* (pp. 143 - 148). Varenna, Lake Como: CRC Press, Taylor & Francis Group.

fib. (2001). *Punching of structural concrete slabs.* Lausanne: fib - International Federation for Structural Concrete.

fib. (2007). *FRP reinforcement in RC structures, Bulletin 40.* Lausanne: fib - International Federation for Structural Concrete.

fib. (2010). *Model Code 2010, First complete draft - Volume 1* . International Federation for Structural Concrete .

Fico, R. (2008). *Limit states design of concrete structures reinforced with FRP bars.* Naples, Italy: Ph.D thesis, Univ. of Naples Federico II.

Grace, N. F., Soliman, A. K., Abdel-Sayed, G., & Saleh, K. R. (1998, November). Behavior and Ductility of Simple and Continuous FRP Reinforced Beams. *Journal of Composites for Construction, 2*(4), 186-194.

Guadagnini, M., Pilakoutas, K., & Waldron, P. (2003). Shear Peformance of FRP Reinforced Concrete Beams. *Journal of Reinforced Plastics and Composites*.

Hassan, M., Ahmed, E., & Benmokrane, B. (2013). Punching-Shear Strength of Normal and High-Strength Two-Way Concrete Slabs Reinforced with GFRP Bars. *Journal of Composites for Construction, 17*(6), 04013003.

Kara, I., & Ashour, A. (2012). Flexural performance of FRP reinforced concrete beams. *Composite Structures 94*, 1616-1625.

Kassem, C., Farghaly, A. S., & Benmokrane, B. (2011, October). Evaluation of Flexural Behavior and Serviceabiliyt Performance of Concrete Beams Reinforced with FRP Bars. *Journal of Composites for Construction, 15*(5), 682-695.

Katz, A. (1998). Effect of Helical Wrapping on Fatigue Resistance of GFRP. *Journal of Composites for Construction*, 121 - 125.

Kocaoz, S., Samaranayake, V., & Nanni, A. (2005). Tensile characterization of glass FRP bars. *Composites: Part B 36*, 127-134.

Lee, J., Kim, T., Kim, T., Yi, C., Park, J., You, Y., & Park, Y. (2008). Interfacial bond strength of glass fiber reinforced polymer bars in high-strength concrete. *Composites: Part B 39*, 258-270.

Lee, J.-H., Yoon, Y.-S., Cook, W. D., & Mitchell, D. (2009, July-August). Improving Punching Shear Behavior of Glass Fiber-Reinforced Polymer Reinforced Slabs. *ACI Structural Journal, 106*(4), 427-434.

Mufti, A., Bakht, B., Banthia, N., Benmokrane, B., Desgagne, G., Eden, R., . . . Taljsten, B. (2007). *New Canadian Highway Bridge Design Code design provisions for fibre-reinforced structures.* Canadian Journal of Civil Engineering.

Noel, M., & Soudki, K. (2014). Fatigue Behavior of GFR Reinforcing Bars in Air and in Concrete. *Journal of Composites for Construction*.

NZTA. (2008). *Research Report 364: Standard Precast Concrete Bridge Beams.* NZ Transport Agency.

NZTA. (2011). *State Highway Asset Management Plan 2012 - 2015.* NZ Transport Agency.

NZTA. (2012). *Research Report 475; Data collection and monitoring strategies for asset management of New Zealand road bridges.*

NZTA. (2013). *Bridge Manual 3rd Edition.* NZ Transport Agency.

Ospina, C. E., Alexander, S. D., & Cheng, J. J. (2003). Punching of Two-Way Concrete Slabs with Fiber-Reinforced Polymer Reinforcing Bars or Grids. *ACI Structural Journal*, 589-598.

Razaqpur, A., Svecova, D., & Cheung, M. (2000). Rational method for calculating deflection of fiber reinforced polymer reinforced beams. *ACI Structural Journal 97*, 175 - 184.

Robert, M., Cousin, P., & Benmokrane, B. (2009). Durability of GFRP Reinforcing Bars Embedded in Moist Concrete. *Journal of Composites for Construction, Vol 13, No. 2*, 66 - 73.

S. Kovaoz, V. S. (2005). Tensile characterization of glass FRP bars. *Composites: Part B (36)*, 127-134.

Saikia, B., Kumar, P., Thomas, J., Rao, K. N., & Ramaswamy, A. (2007). Strength and serviceability performance of beams reinfroced with GFRP bars in flexure. *Construction and Building Materials, 21*, 1709-1719.

Soong, W., Raghavan, J., & Rizkalla, S. (2011). Fundamental mechanisms of bonding of glass fiber reinforced polymer reinforcement to concrete. *Construction and Building Materials 25*, 2813-2821.

Theriault, M., & Benmokrane, B. (1998). Efects of FRP Reinforcement Ratio and Concrete Strength on Flexural Behavior of Concrete Beams. *Journal of Composites for Construction, 2*(1), 7-16.

Toutanji, H., & Deng, Y. (2003). Deflection and crack-width prediction of concrete beams reinforced with glass FRP rods. *Construction and Building Materials, 17*, 69-74.

Yost, J. R., Gross, S. P., & Dinehart, D. W. (2001). Shear Strength of Normal Strength Concrete Beams Reinforced with Deformed GFRP bars. *Journal of Composites for Construction*.

Appendix A: Tensile Testing Data

Processed data, Photos of failed specimens, Force vs displacement graphs for each test specimen

Test series:

10 mm tests: H1 – H10

12 mm tests: G1 – G10

16 mm tests: E1 – E8

22 mm tests: F1 – F10

Specimen code	Nominal diameter (mm)	Root diameter (mm)	Failure Load (kN)	UTS (MPa)	E modulus (GPa)
H1	10	9.2	60.8	915.2	57.6

Above and Below: Failed sample
Right: Load vs Displacement Graph for first part of tensile test

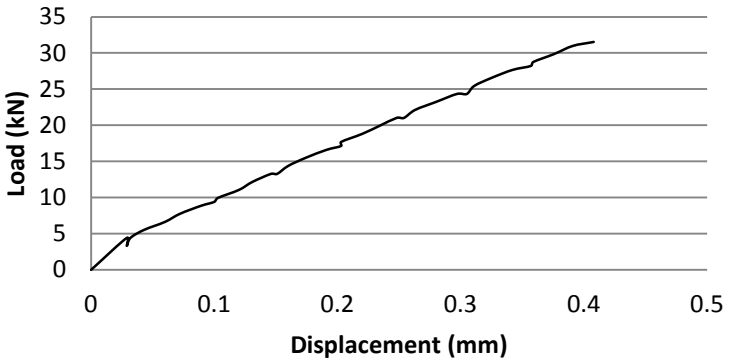

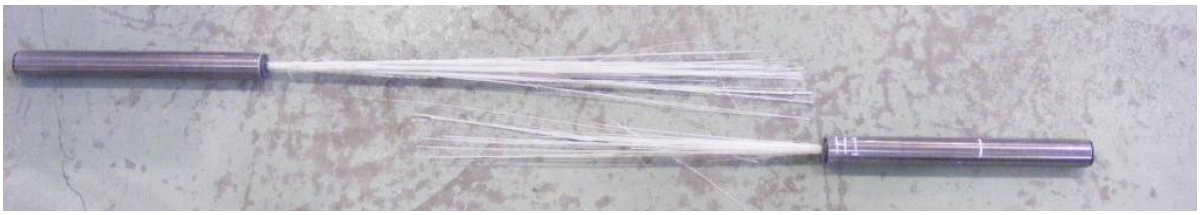

Specimen code	Nominal diameter (mm)	Root diameter (mm)	Failure Load (kN)	UTS (MPa)	E modulus (GPa)
H2	10	9.2	60.2	906.0	59.7

Above and Below: Failed sample
Right: Load vs Displacement Graph for first part of tensile test

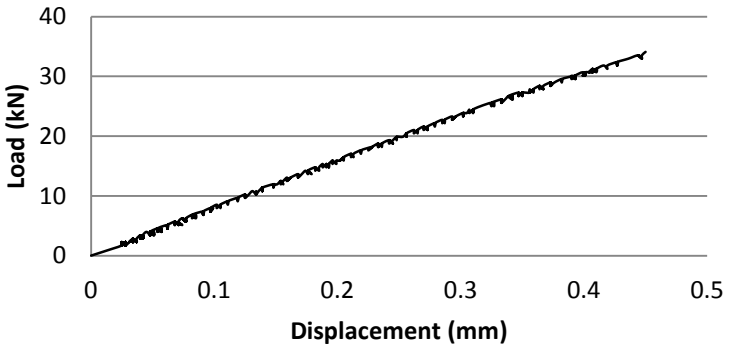

Specimen code	Nominal diameter (mm)	Root diameter (mm)	Failure Load (kN)	UTS (MPa)	E modulus (GPa)
H3	10	9.2	61.4	974.4	61.4

Above and Below: Failed sample
Right: Load vs Displacement Graph for first part of tensile test

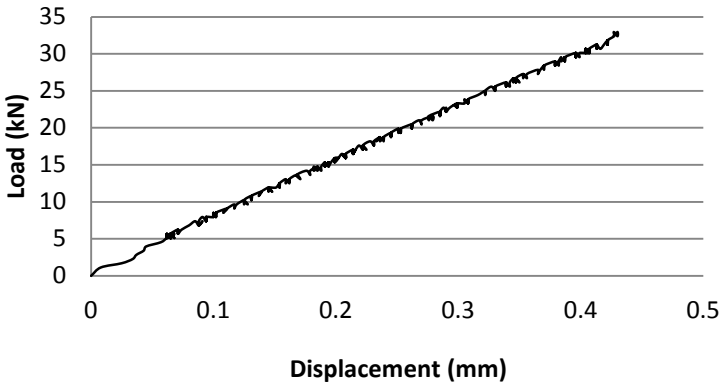

Specimen code	Nominal diameter (mm)	Root diameter (mm)	Failure Load (kN)	UTS (MPa)	E modulus (GPa)
H4	10	9.2	61.4	965.8	61.4

Above and Below: Failed sample
Right: Load vs Displacement Graph for first part of tensile test

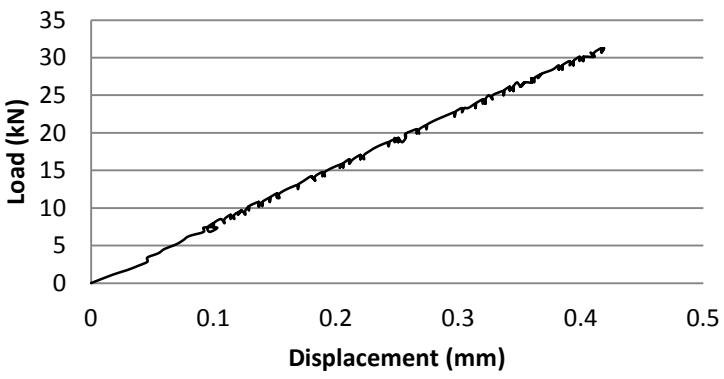

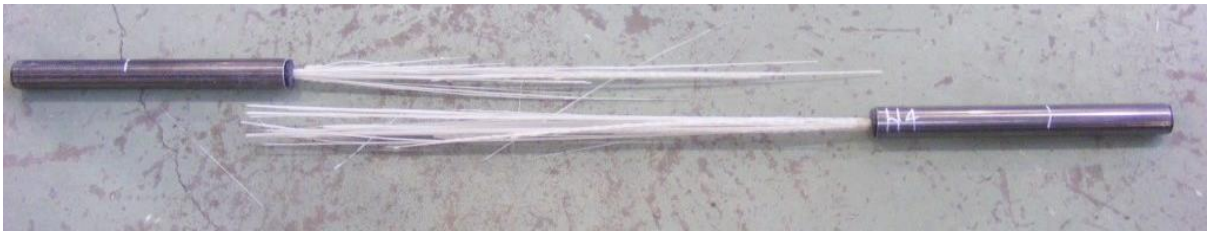

Specimen code	Nominal diameter (mm)	Root diameter (mm)	Failure Load (kN)	UTS (MPa)	E modulus (GPa)
H5	10	9.2	61.4	923.1	65.3

Above and Below: Failed sample
Right: Load vs Displacement Graph for first part of tensile test

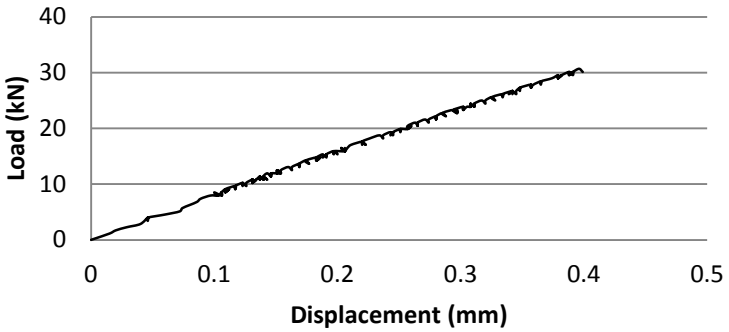

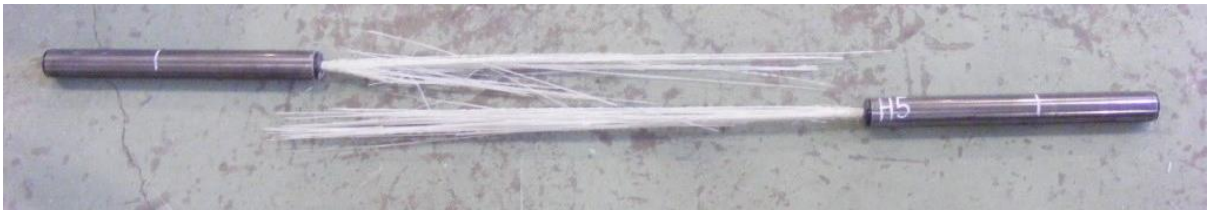

Specimen code	Nominal diameter (mm)	Root diameter (mm)	Failure Load (kN)	UTS (MPa)	E modulus (GPa)
H6	10	9.2	63.1	948.7	62.2

Above and Below: Failed sample
Right: Load vs Displacement Graph for first part of tensile test

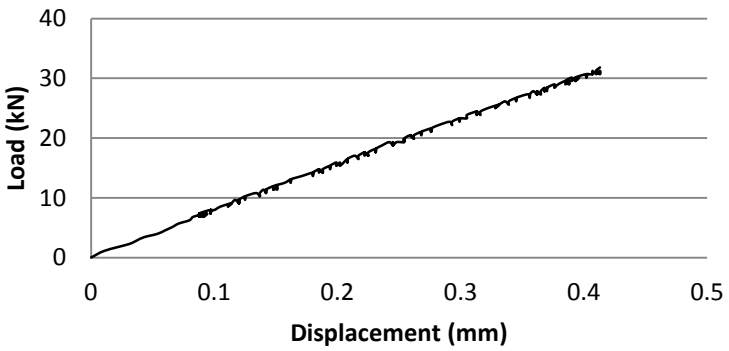

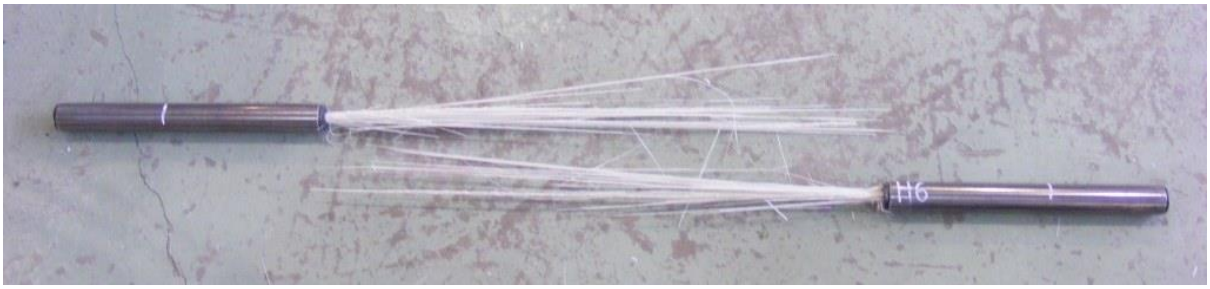

Specimen code	Nominal diameter (mm)	Root diameter (mm)	Failure Load (kN)	UTS (MPa)	E modulus (GPa)
H7	10	9.2	58.0	871.8	57.2

Above and Below: Failed sample
Right: Load vs Displacement Graph for first part of tensile test

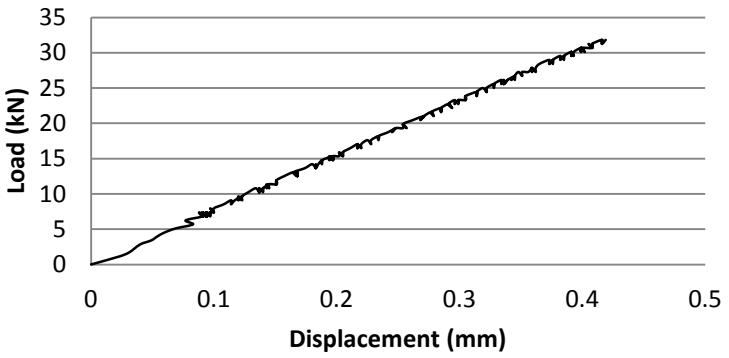

Specimen code	Nominal diameter (mm)	Root diameter (mm)	Failure Load (kN)	UTS (MPa)	E modulus (GPa)
H8	10	9.2	65.3	982.9	57.6

Above and Below: Failed sample
Right: Load vs Displacement Graph for first part of tensile test

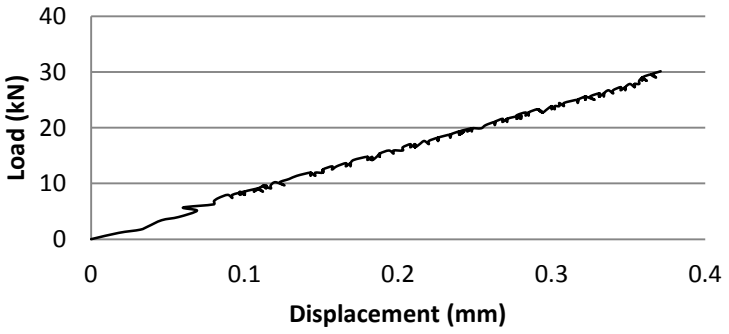

Specimen code	Nominal diameter (mm)	Root diameter (mm)	Failure Load (kN)	UTS (MPa)	E modulus (GPa)
H9	10	9.2	65.3	982.9	56.4

Above and Below: Failed sample
Right: Load vs Displacement Graph for first part of tensile test

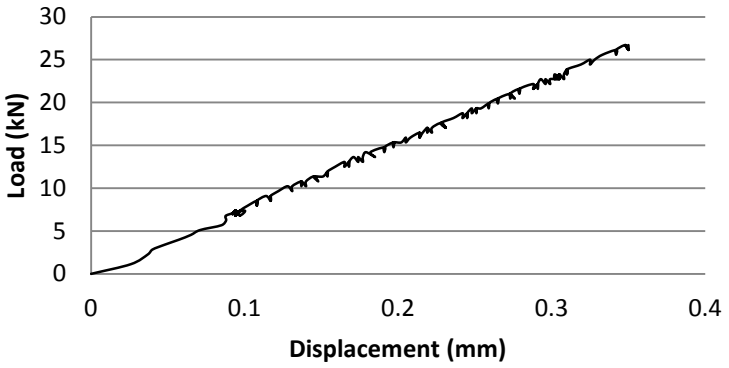

Specimen code	Nominal diameter (mm)	Root diameter (mm)	Failure Load (kN)	UTS (MPa)	E modulus (GPa)
H10	10	9.2	61.4	923.1	57.9

Above and Below: Failed sample
Right: Load vs Displacement Graph for first part of tensile test

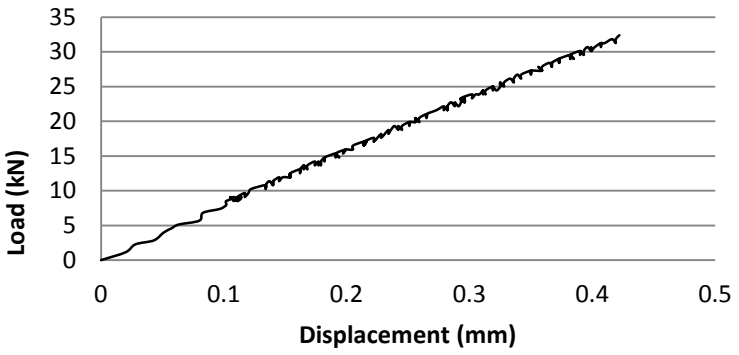

Specimen code	Nominal diameter (mm)	Root diameter (mm)	Failure Load (kN)	UTS (MPa)	E modulus (GPa)
G1	12	11.2	86.9	882.4	50.2

Above and Below: Failed sample
Right: Load vs Displacement Graph for first part of tensile test

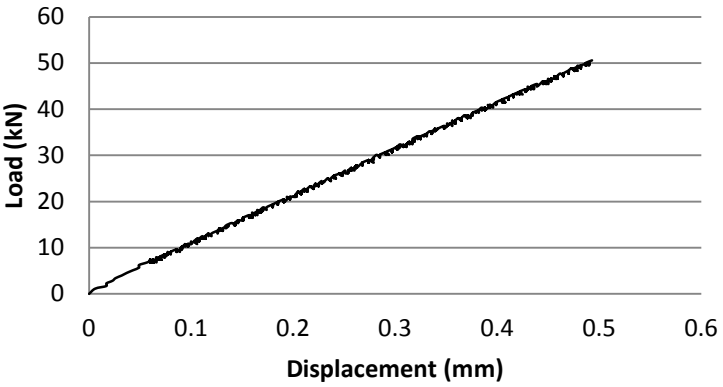

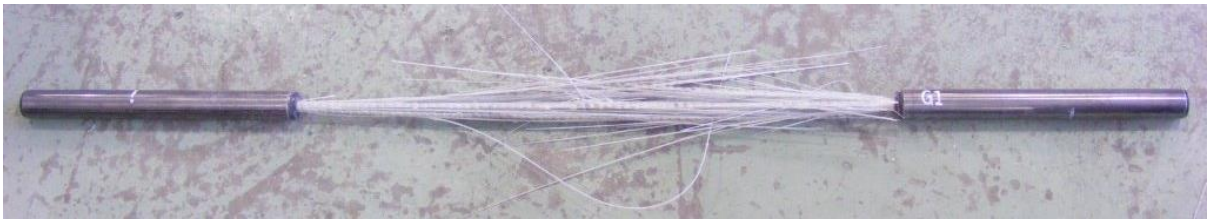

Specimen code	Nominal diameter (mm)	Root diameter (mm)	Failure Load (kN)	UTS (MPa)	E modulus (GPa)
G2	12	11.2	87.5	888.1	54.4

Above and Below: Failed sample
Right: Load vs Displacement Graph for first part of tensile test

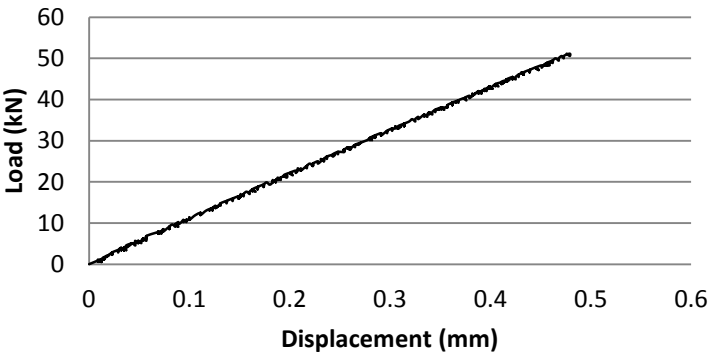

Specimen code	Nominal diameter (mm)	Root diameter (mm)	Failure Load (kN)	UTS (MPa)	E modulus (GPa)
G3	12	11.2	85.2	865.1	52.4

Above and Below: Failed sample
Right: Load vs Displacement Graph for first part of tensile test

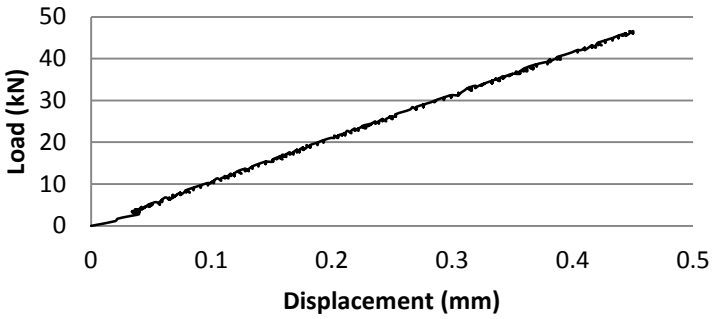

Specimen code	Nominal diameter (mm)	Root diameter (mm)	Failure Load (kN)	UTS (MPa)	E modulus (GPa)
G4	12	11.2	85.2	865.1	52.3

Above and Below: Failed sample
Right: Load vs Displacement Graph for first part of tensile test

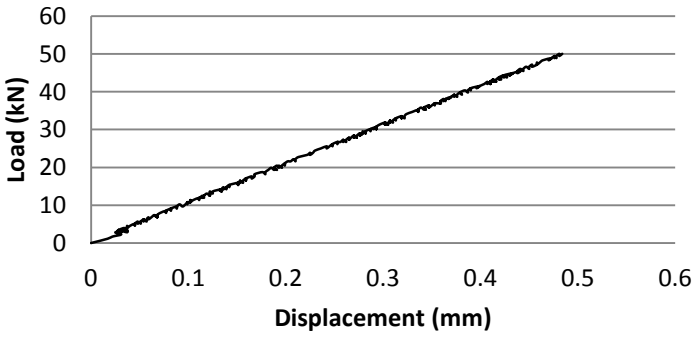

Specimen code	Nominal diameter (mm)	Root diameter (mm)	Failure Load (kN)	UTS (MPa)	E modulus (GPa)
G5	12	11.2	84.1	853.5	53.1

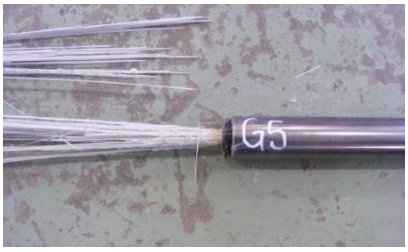

Above and Below: Failed sample
Right: Load vs Displacement Graph for first part of tensile test

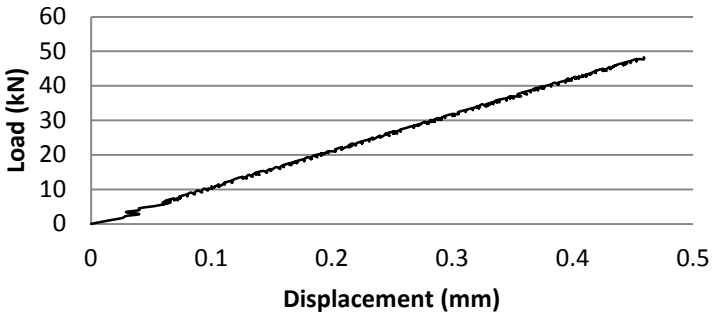

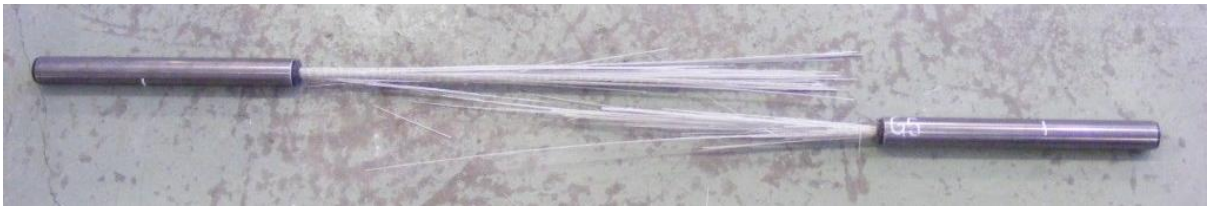

Specimen code	Nominal diameter (mm)	Root diameter (mm)	Failure Load (kN)	UTS (MPa)	E modulus (GPa)
G6	12	11.2	85.8	870.8	53.8

Above and Below: Failed sample
Right: Load vs Displacement Graph for first part of tensile test

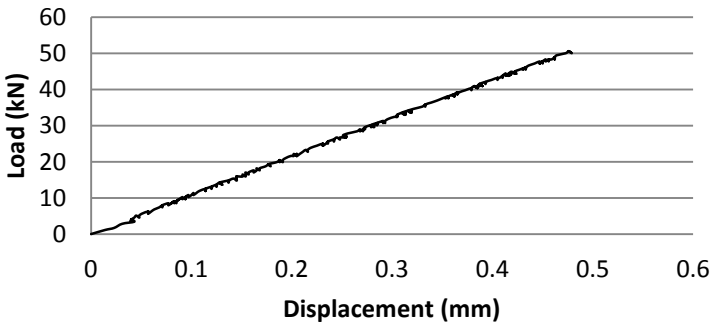

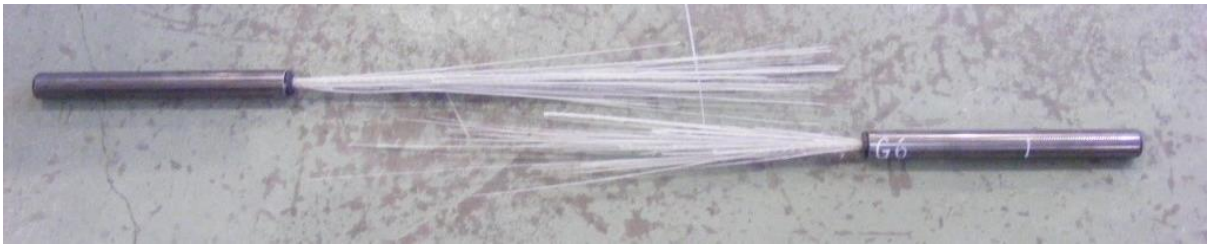

Specimen code	Nominal diameter (mm)	Root diameter (mm)	Failure Load (kN)	UTS (MPa)	E modulus (GPa)
G7	12	11.2	85.2	865.1	52.8

Above and Below: Failed sample
Right: Load vs Displacement Graph for first part of tensile test

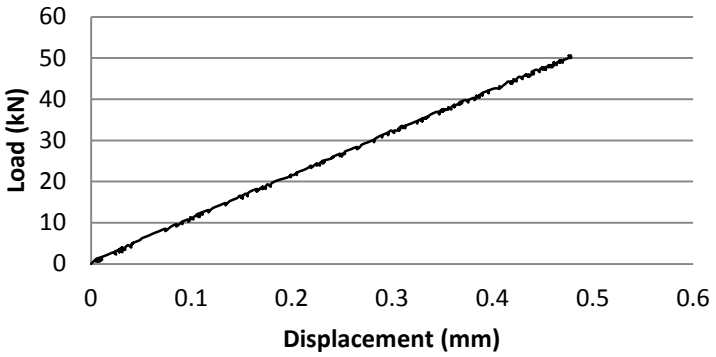

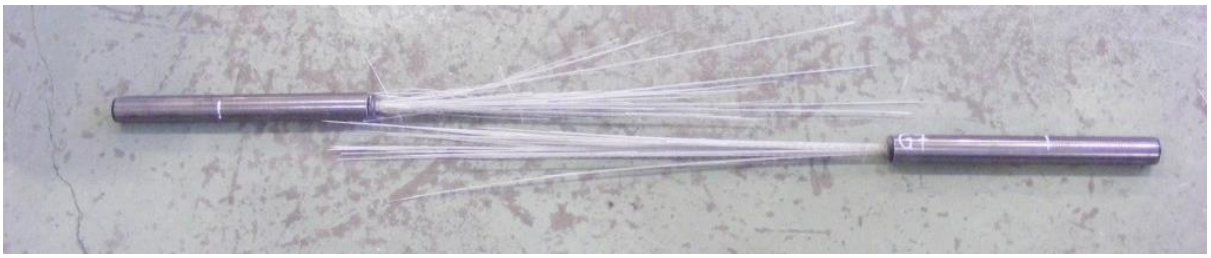

Specimen code	Nominal diameter (mm)	Root diameter (mm)	Failure Load (kN)	UTS (MPa)	E modulus (GPa)
G8	12	11.2	87.5	888.1	53.2

Above and Below: Failed sample
Right: Load vs Displacement Graph for first part of tensile test

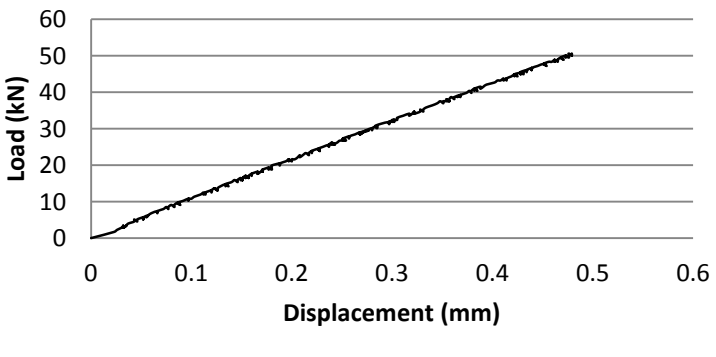

Specimen code	Nominal diameter (mm)	Root diameter (mm)	Failure Load (kN)	UTS (MPa)	E modulus (GPa)
G9	12	11.2	86.9	882.4	52.6

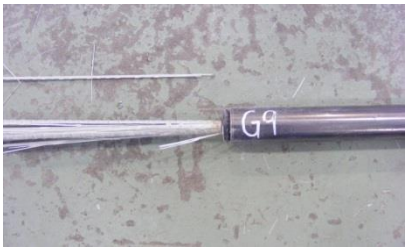

Above and Below: Failed sample
Right: Load vs Displacement Graph for first part of tensile test

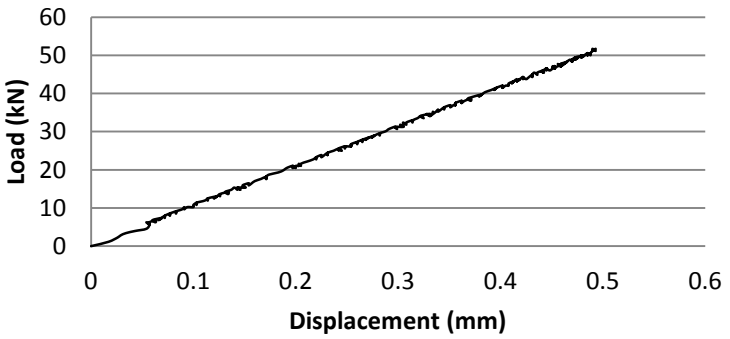

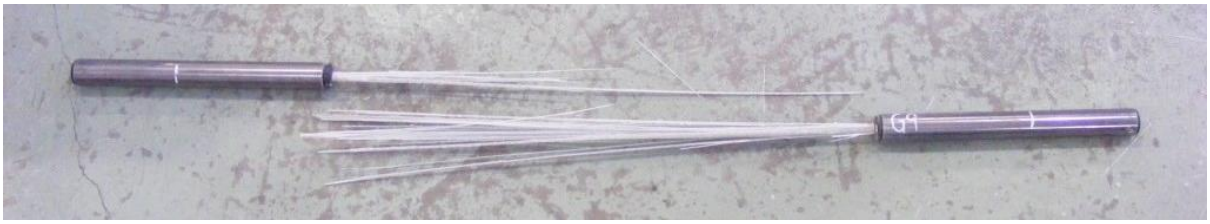

Specimen code	Nominal diameter (mm)	Root diameter (mm)	Failure Load (kN)	UTS (MPa)	E modulus (GPa)
G10	12	11.2	88.1	893.9	54.3

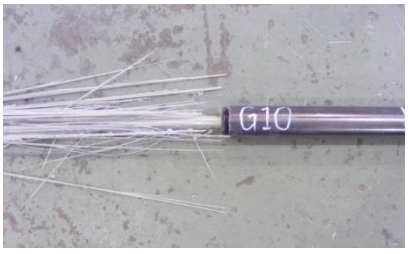

Above and Below: Failed sample
Right: Load vs Displacement Graph for first part of tensile test

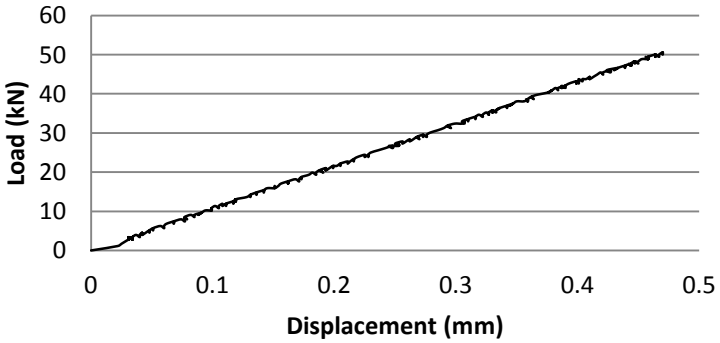

Specimen code	Nominal diameter (mm)	Root diameter (mm)	Failure Load (kN)	UTS (MPa)	E modulus (GPa)
E1	16	15.2	154.5	851.7	-

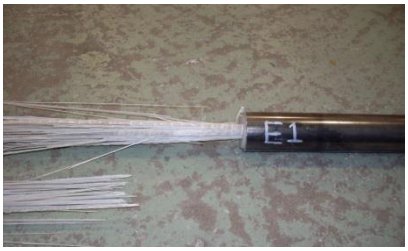

Above and Below: Failed sample
Right: Load vs Displacement Graph for first part of tensile test

Note: Error with extensometer.
No E modulus calculation or load vs displacement graph.

Specimen code	Nominal diameter (mm)	Root diameter (mm)	Failure Load (kN)	UTS (MPa)	E modulus (GPa)
E2	16	15.2	157.4	867.3	-

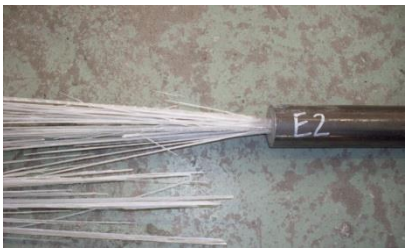

Above and Below: Failed sample
Right: Load vs Displacement Graph for first part of tensile test

Note: Error with extensometer.
No E modulus calculation or load vs displacement graph.

Specimen code	Nominal diameter (mm)	Root diameter (mm)	Failure Load (kN)	UTS (MPa)	E modulus (GPa)
E3	16	15.2	156.8	864.2	47.5

Above and Below: Failed sample
Right: Load vs Displacement Graph for first part of tensile test

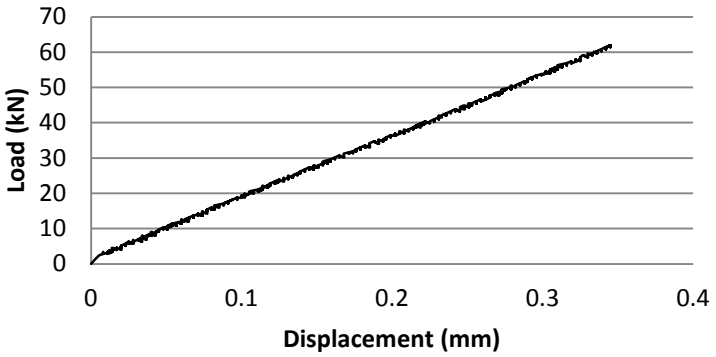

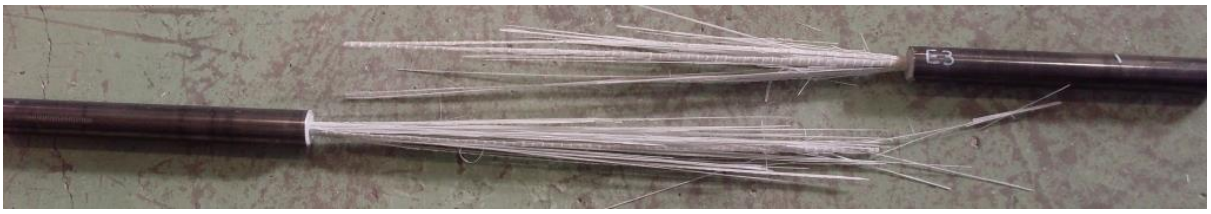

Specimen code	Nominal diameter (mm)	Root diameter (mm)	Failure Load (kN)	UTS (MPa)	E modulus (GPa)
E4	16	15.2	164.2	904.9	51.0

Above and Below: Failed sample
Right: Load vs Displacement Graph for first part of tensile test

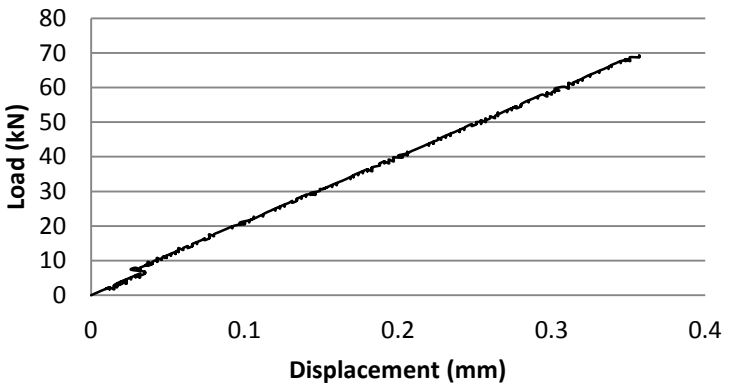

Specimen code	Nominal diameter (mm)	Root diameter (mm)	Failure Load (kN)	UTS (MPa)	E modulus (GPa)
E5	16	15.2	158.5	873.6	51.8

Above and Below: Failed sample
Right: Load vs Displacement Graph for first part of tensile test

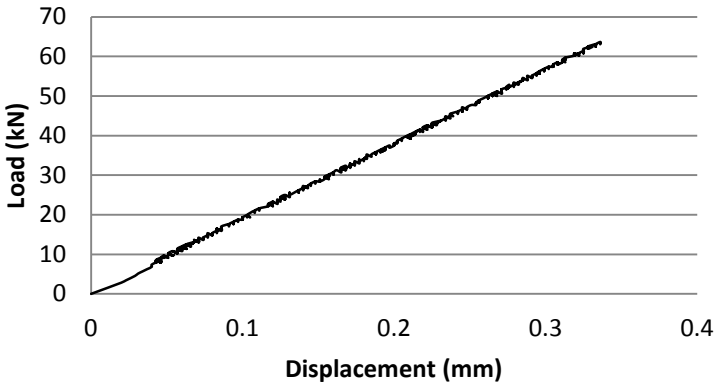

Specimen code	Nominal diameter (mm)	Root diameter (mm)	Failure Load (kN)	UTS (MPa)	E modulus (GPa)
E6	16	15.2	163.6	901.8	50.0

Above and Below: Failed sample
Right: Load vs Displacement Graph for first part of tensile test

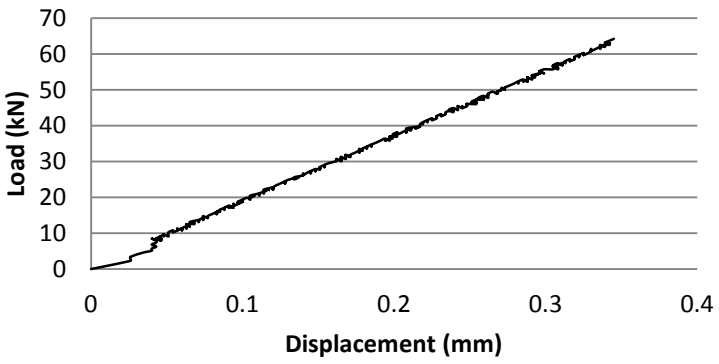

Specimen code	Nominal diameter (mm)	Root diameter (mm)	Failure Load (kN)	UTS (MPa)	E modulus (GPa)
E7	16	15.2	158.5	873.6	51.8

Above and Below: Failed sample
Right: Load vs Displacement Graph for first part of tensile test

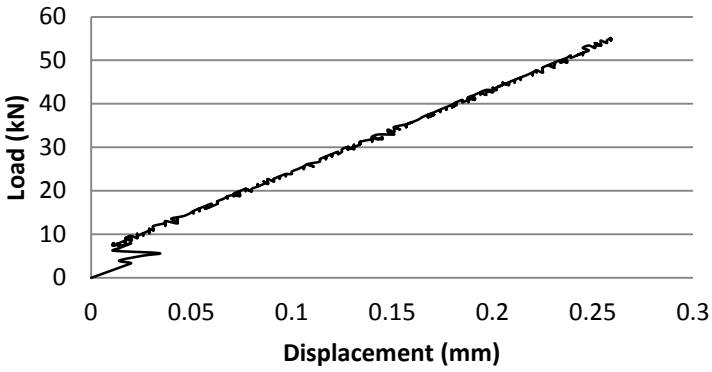

Specimen code	Nominal diameter (mm)	Root diameter (mm)	Failure Load (kN)	UTS (MPa)	E modulus (GPa)
E8	16	15.2	163.6	901.8	51.6

Above and Below: Failed sample
Right: Load vs Displacement Graph for first part of tensile test

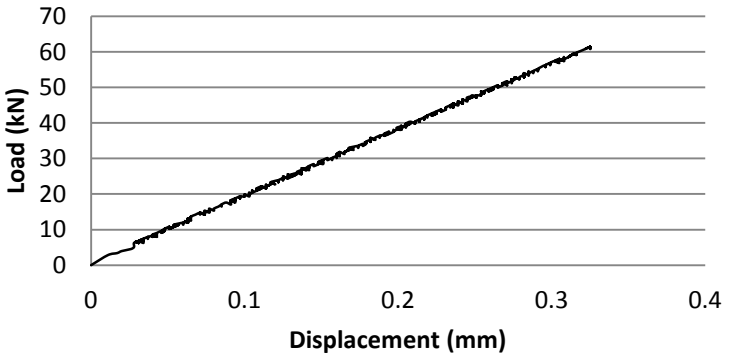

Specimen code	Nominal diameter (mm)	Root diameter (mm)	Failure Load (kN)	UTS (MPa)	E modulus (GPa)
F1	22	21.2	314.2	890.0	50.6

Above and Below: Failed sample
Right: Load vs Displacement Graph for first part of tensile test

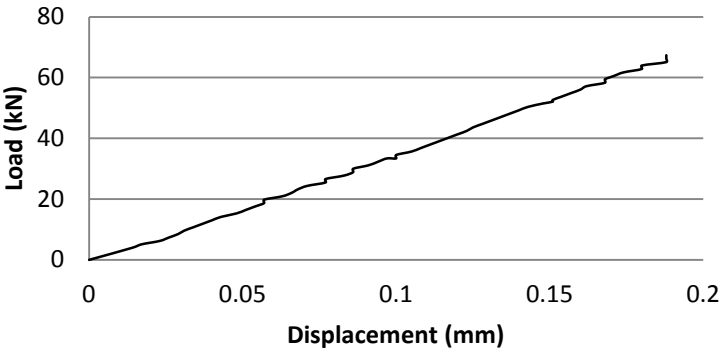

Specimen code	Nominal diameter (mm)	Root diameter (mm)	Failure Load (kN)	UTS (MPa)	E modulus (GPa)
F2	22	21.2	318.1	901.2	51.5

Above and Below: Failed sample
Right: Load vs Displacement Graph for first part of tensile test

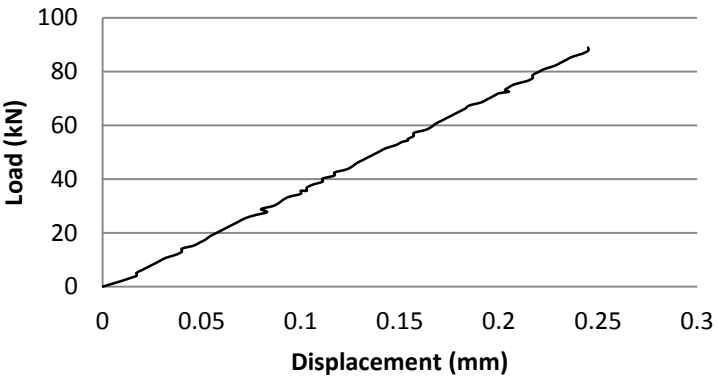

Specimen code	Nominal diameter (mm)	Root diameter (mm)	Failure Load (kN)	UTS (MPa)	E modulus (GPa)
F3	22	21.2	315.8	894.8	50.1

Above and Below: Failed sample
Right: Load vs Displacement Graph for first part of tensile test

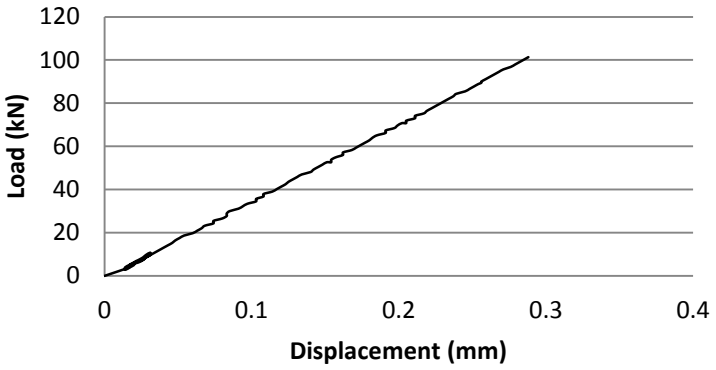

Specimen code	Nominal diameter (mm)	Root diameter (mm)	Failure Load (kN)	UTS (MPa)	E modulus (GPa)
F4	22	21.2	312.5	885.2	48.4

Above and Below: Failed sample
Right: Load vs Displacement Graph for first part of tensile test

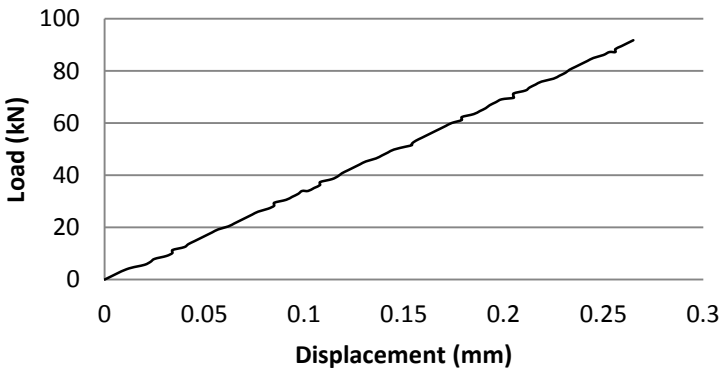

Specimen code	Nominal diameter (mm)	Root diameter (mm)	Failure Load (kN)	UTS (MPa)	E modulus (GPa)
F5	22	21.2	314.2	890.0	49.6

Above and Below: Failed sample
Right: Load vs Displacement Graph for first part of tensile test

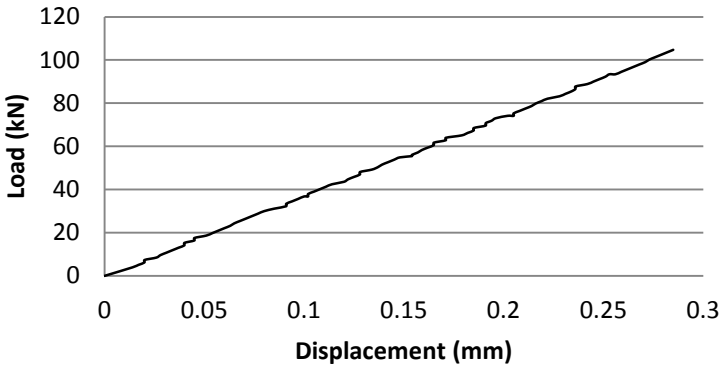

Specimen code	Nominal diameter (mm)	Root diameter (mm)	Failure Load (kN)	UTS (MPa)	E modulus (GPa)
F6	22	21.2	310.2	878.7	50.0

Above and Below: Failed sample
Right: Load vs Displacement Graph for first part of tensile test

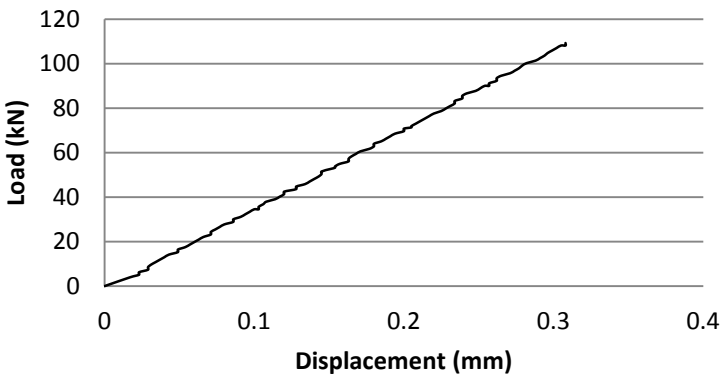

Specimen code	Nominal diameter (mm)	Root diameter (mm)	Failure Load (kN)	UTS (MPa)	E modulus (GPa)
F7	22	21.2	318.7	902.8	52.9

Above and Below: Failed sample
Right: Load vs Displacement Graph for first part of tensile test

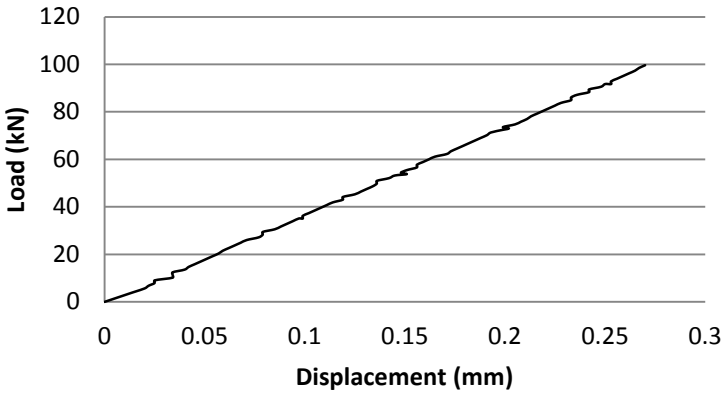

Specimen code	Nominal diameter (mm)	Root diameter (mm)	Failure Load (kN)	UTS (MPa)	E modulus (GPa)
F8	22	21.2	310.8	880.4	51.7

Above and Below: Failed sample
Right: Load vs Displacement Graph for first part of tensile test

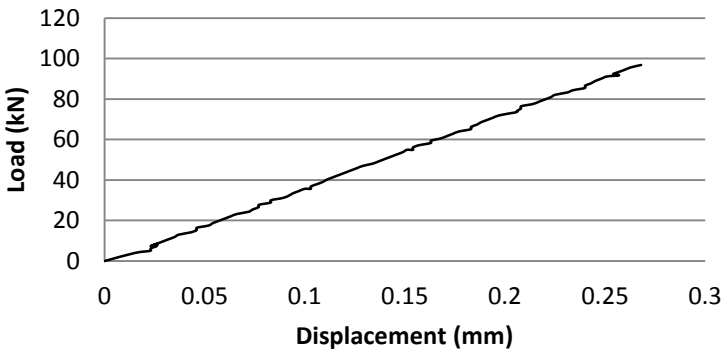

Specimen code	Nominal diameter (mm)	Root diameter (mm)	Failure Load (kN)	UTS (MPa)	E modulus (GPa)
F9	22	21.2	326.6	925.3	-

Note: Error with extensometer.
No E modulus calculation or load vs displacement graph.

Above and Below: Failed sample
Right: Load vs Displacement Graph for first part of tensile test

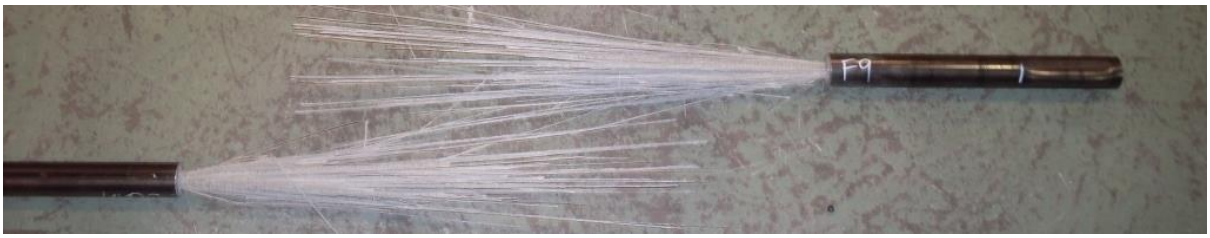

Specimen code	Nominal diameter (mm)	Root diameter (mm)	Failure Load (kN)	UTS (MPa)	E modulus (GPa)
F10	22	21.2	312.5	885.2	49.6

Above and Below: Failed sample
Right: Load vs Displacement Graph for first part of tensile test

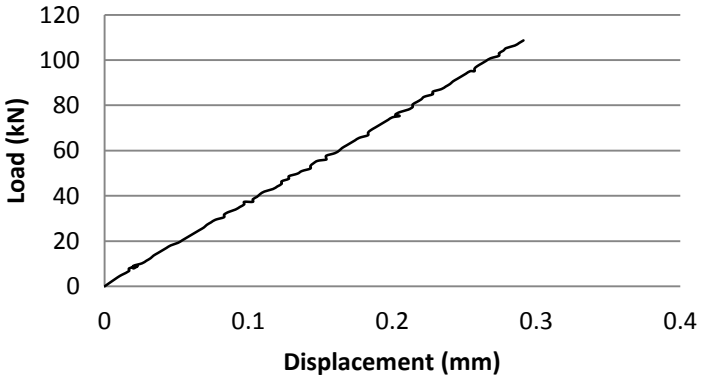

Appendix B: SLS and ULS loading calculations

SLS and ULS loading calculations for Flexural Testing

Due to the set-up of the test, the load measured by the load cell could not be directly related to the moment experienced by the slab and to the expected design live loading. To calculate the applied load corresponding to the Serviceability behavior (P_{SLS}) it was assumed that this load would be uniformly distributed along the spreading beams to allow a 'per metre' moment to be easily calculated. The load was based on the HN-HO-72 loading with additional load as recommended for self-weight and services. The live load is based on a single element of HN loading consisting of 60 kN loading over a contact area of 500 x 200 mm to represent a wheel load and 3.5 kN/m^2 uniformly distributed load.

The SLS loading combination used is:

$$SLS = DL + 1.35\ LL \times I$$

where DL is dead load, LL is live load and I is the dynamic load factor, 1.3.

Dead Load:

5.0 kN/m2 self weight

1.5 kN/m2 surfacing

0.25 kN/m2 future servicing

(Handrails ignored as they create a negative moment in this case)

Sum = 6.75 kN/m2

Live load:

3.5 kN/m2

(60 kN concentrated load)

Considering uniformly distributed loads first:

$$UDL = 6.75\frac{kN}{m^2} + 1.35 \times 3.5\frac{kN}{m^2} \times 1.3$$

$$UDL = 12.89\frac{kN}{m^2}$$

Max moment caused by UDL:

$$M_{\max(UDL)} = \frac{12.89 \times 2.5^2}{8} = 10.07\frac{kNm}{m}$$

Considering concentrated load:

$$Point\ Load = 1.35\ \times 60\ kN \times 1.3$$

$$Point\ Load = 105.3\ kN$$

Moment in slab (per metre width) caused by applied load P:

Load split between two load spreader beams: P/2

Assume uniform distribution of load along: $w = \frac{P/2}{2.6m} = \frac{P}{5.2m}$

Max moment: $M_{max} = \frac{P}{5.2m} \times \left(\frac{L-a}{2}\right) = \frac{P}{5.2m} \times \left(\frac{2.5m-0.8m}{2}\right) = 0.1635\ P\ (\frac{kNm}{m})$

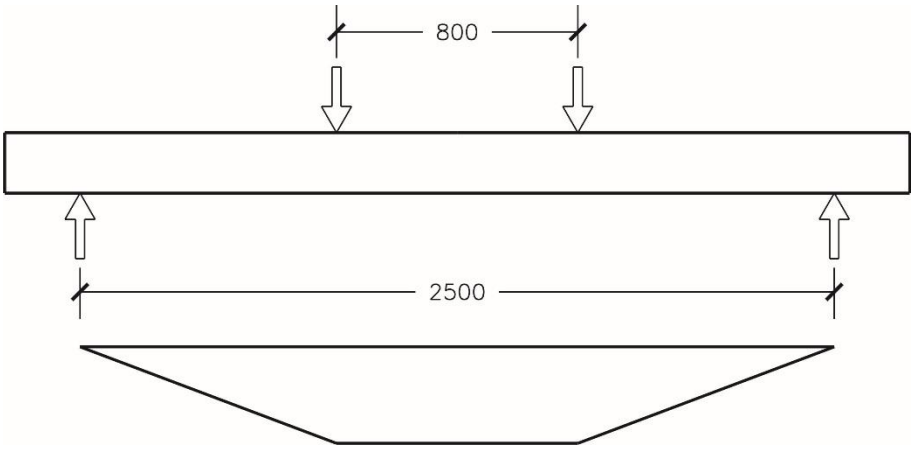

Schematic of the test set-up and bending moment diagram showing the maximum moment in the central region between the loading points.

Calculate the applied load at SLS:

$$P_{SLS} = \frac{10.07}{0.1635} + 105.3 = 167\ kN \approx 170\ kN$$

ULS calculation:

The ULS loading combination used is:

$$ULS = 1.35DL + 1.10\ OL \times I$$

where DL is dead load, OL is live load and I is the dynamic load factor, 1.3. The dead load is the same as for SLS. The over load consists of a 120 kN concentrated load and 3.5 kN/m^2 uniformly distributed load.

Over load:

3.5 kN/m2 (same as live load)

(120 kN concentrated load)

Considering uniformly distributed loads first:

$$UDL = 1.35 \times 6.75\frac{kN}{m^2} + 1.67 \times 3.5\frac{kN}{m^2} \times 1.3$$

$$UDL = 16.71 \frac{kN}{m^2}$$

Max moment caused by UDL:

$$M_{\max(UDL)} = \frac{16.71 \times 2.5^2}{8} = 13.05 \frac{kNm}{m}$$

Considering concentrated load:

$$Point\ Load = 1.10\ \times 120\ kN \times 1.3$$

$$Point\ Load = 171.6\ kN$$

Calculate the applied load at ULS:

$$P_{ULS} = \frac{13.05}{0.1635} + 171.6 = 251.4\ kN\ \approx 250$$

SLS and ULS loading calculations for Punching Shear Testing:

The applied load corresponding to the Serviceability behavior (P_{SLS}) was calculated based on the NZTA Bridge Manual HN loading with additional load as recommended for self-weight and services. It was assumed that the uniformly distributed load prescribed by the NZTA Bridge manual was applied to the whole of the area 'enclosed' by the supports, but was considered by determining the equivalent load applied through the concentrated load footprint in the centre of the span.

The SLS loading combination used is:

$$SLS = DL + 1.35\ LL \times I$$

where DL is dead load, LL is live load and I is the dynamic load factor, 1.3.

Dead Load:

5.0 kN/m2 self weight

1.5 kN/m2 surfacing

0.25 kN/m2 future servicing

(Handrails ignored as they create a negative moment in this case)

Sum = 6.75 kN/m2

Live load:

3.5 kN/m2

60 kN concentrated load

Considering uniformly distributed loads first, and assuming they act in the centre of the slab:

$$UDL = 6.75\frac{kN}{m^2} + 1.35 \times 3.5\frac{kN}{m^2} \times 1.3$$

$$UDL = 12.89\frac{kN}{m^2}$$

Considering the approximate area of the slab affected (based on experimental test set-up):

$$Area\ affected = 2.240\ \times 2.568 = 5.75\ m^2$$

$$Point\ Load\ (from\ UDL) = 5.75m^2 \times 12.89\frac{kN}{m^2} = 74\ kN$$

Considering concentrated load:

$$Point\ Load\ (from\ wheel\ load) = 1.35\ \times 60\ kN \times 1.3$$

$$Point\ Load = 105.3\ kN$$

Calculate the applied load at SLS:

$$P_{SLS} = \ 74 + 105.3 = 179.3\ kN \approx 180\ kN$$

ULS calculation:

The ULS loading combination used is:

$$ULS = 1.35DL + 1.10\ OL \times I$$

where DL is dead load, OL is live load and I is the dynamic load factor, 1.3. The dead load is the same as for SLS. The over load consists of a 120 kN concentrated load and 3.5 kN/m^2 uniformly distributed load.

Over load:

3.5 kN/m2 (same as live load)

120 kN concentrated load

Considering uniformly distributed loads first, and assuming they act in the centre of the slab:

$$UDL = 1.35 \times 6.75\frac{kN}{m^2} + 1.67 \times 3.5\frac{kN}{m^2} \times 1.3$$

$$UDL = 16.71\frac{kN}{m^2}$$

Area affected is the same as for SLS.

$$Point\ Load\ (from\ UDL) = 5.75m^2 \times 16.71\frac{kN}{m^2} = 96.1\ kN$$

Considering concentrated load:

$$Point\ Load\ (from\ wheel\ load) = 1.35\ \times 120\ kN \times 1.3$$

$$Point\ Load = 210.6\ kN$$

Calculate the applied load at ULS:

$$P_{ULS} =\ 96.1 + 210.6 = 306.7\ kN\ \approx 300\ KN$$

Appendix C: Mateen-bar Technical Specifications (2013)

Used for analysis of test specimens.

Appendix D: Mateen-bar Technical Specifications (Nov 2014)

Including some Generation II (GII) reinforcing bars.

Used for design example.